

Understanding Proton Transfer: Towards Mapping
Proton Motion in Molecular Crystals Using
Ultrafast Spectroscopy and Electron Diffraction

DISSERTATION

zur Erlangung des Doktorgrades
an der Fakultät für Mathematik, Informatik und Naturwissenschaften
Fachbereich Chemie der Universität Hamburg

Angefertigt am Max-Planck-Institut für
Struktur und Dynamik der Materie

vorgelegt von

Hyein Hwang

Hamburg, Deutschland

Januar 2023

Dissertation submitted to the University of Hamburg

Dissertation Assessors:

Prof. Dr. R. J. Dwayne Miller

Prof. Dr. Gabriel Bester

Disputation Committee:

Prof. Dr. Alf Mews (Chair)

Prof. Dr. Christian Bressler

Prof. Dr. R. J. Dwayne Miller

Date of Disputation:

17. 3. 2023

List of publications

Hwang, H., et al., *Two-dimensional confinement for generating thin single crystals for applications in time-resolved electron diffraction and spectroscopy: an intramolecular proton transfer study*. *Chem. Commun*, 2022. 58(70): p. 9774-9777.

Table of content

List of publications	iii
Table of content	iv
List of abbreviations	vi
ZUSAMMENFAS SUNG	viii
ABSTRACT.....	x
Chapter 1. Introduction	1
Chapter 2. Review of Literature.....	5
2.1 Photo-induced transitions in molecular system.....	5
2.2 Photo-induced chemical reactions in molecular systems.....	7
2.2.1 Excited State Intramolecular Proton Transfer (ESIPT) Reaction	8
2.2.2 Hydroxyanthraquinone derivatives	10
Chapter 3. Theoretical Framework	13
3.1 Thin crystal growth for transmission-based measurements	13
3.2 Characterisation methods.....	18
3.2.1 Microscopic methods	18
3.2.2 Diffraction methods	18
3.2.3 Steady state absorption.....	20
3.3 Quantum chemical calculations	21
3.4 Femtosecond transient absorption.....	22
Chapter 4. Thin Crystal Growth and Characterization.....	28
4.1 Morphology.....	28
4.1.1 Control over nucleation and growth.....	29
4.1.2 Thickness measurement	34
4.1.3 Effect of spatial confinement	36
4.2 Crystallographic Characterization.....	37

4.2.1	Single crystal X-ray diffraction.....	37
4.2.2	Transmission Electron Microscopy.....	39
Chapter 5. Steady-State Absorption Measurements and Quantum Chemical Calculations.....		41
5.1	Steady-state absorption spectra.....	41
5.2	Quantum chemical calculations.....	43
Chapter 6. Excited State Dynamics: Femtosecond Transient Absorption.....		51
6.1	Excited state dynamics in solution phase.....	51
6.1.1	1,5-Dihydroxyanthraquinone.....	52
6.1.2	1,8-Dihydroxyanthraquinone.....	54
6.1.3	1,4-Dihydroxyanthraquinone.....	57
6.2	Crystalline Phase.....	59
6.2.1	1,5-Dihydroxyanthraquinone.....	59
6.2.2	1,8-Dihydroxyanthraquinone.....	61
6.2.3	1,4-Dihydroxyanthraquinone.....	63
6.2.4	Discussion.....	65
Chapter 7. Summary and Outlook.....		66
Bibliography.....		69
Appendix A.....		74
Appendix B.....		103
Acknowledgements.....		105
Declaration on Oath.....		106

List of abbreviations

Abbreviation	Definition
2D	2-dimension(al)
2D IR spectroscopy	2-dimensional infrared spectroscopy
2HC	2'-hydroxychalcone
3-HF	3-hydroxyflavone
ADP	Adenosine diphosphate
AFM	Atomic force microscope
AIE	Aggregation-induced emission
AIM	Atoms in molecules
ATP	Adenosine triphosphate
BBO	Beta barium borate
BO	Born-Oppenheimer
BS	Beam splitter
CIF	Crystallographic Information File
CSD	Cambridge Structural Database
CVD	Chemical vapor deposition
DHAQ	dihydroxyanthraquinone
DHBIA	N,N'-di[3-Hydroxy-4-(2'-benzothiazole)phenyl]5-tert-butyl-isophthalic amide
DHIA	N,N'-di[3-Hydroxy-4-(2'-benzothiazole)phenyl]isophthalic amide
DM	Dielectric mirror
DMHC	(E)-3-(4-(dimethylamino)phenyl)-1-(1-hydroxynaphthalen-2-yl)prop-2-en-1-one
DNA	Deoxyribonucleic acid
ESA	Excited state absorption
ESIPT	Excited state intramolecular proton transfer
ESPT	Excited state proton transfer
FED	Femtosecond electron diffraction
FWHM	Full width half maxima
GSB	Ground state bleach
HAQ	hydroxyanthraquinone
HOMO	Highest occupied molecular orbital
HWP	Half-waveplate
ISC	Intersystem crossing
L	Convex lens
LUMO	Lowest unoccupied molecular orbital
MO	Molecular orbital
ND	Neutral density filter
NMR	Nuclear magnetic resonance
OAP	Off-axis parabolic mirror
OD	Optical density
PES	Potential energy surface
RNA	Ribonucleic acid
RT	Room temperature
SAED	Selected area electron diffraction

SCXRD	Single crystal X-ray diffraction
SE	Stimulated emission
SN ratio	Signal to noise ratio
TA	Transient absorption
TDDFT	Time dependent density functional theory
TEM	Transmission electron microscope

ZUSAMMENFASSUNG

Der photoinduzierte Protonentransfer ist eine elementare Reaktion in der Photo-(Bio)Chemie. Auch für die organische Optoelektronik ist der Mechanismus dieser Reaktion von großem Interesse. In der Chemie finden die meisten Reaktionen, an denen organische Moleküle beteiligt sind, in kondensierter Phase statt, d. h. flüssig und fest, und nicht in einem isolierten Molekülsystem. Hierbei ermöglicht das Basismedium hohe Kollisionsfrequenzen und schnellere Reaktionsgeschwindigkeiten als in der Gasphase. Auch die Natur des Bades beeinflusst den Reaktionsweg durch Wechselwirkungen mit dem System, da die Freiheitsgrade in der festen Phase geringer als in der flüssigen Phase sind. Darüber hinaus können die elektronischen Zustände, an denen aggregierte Moleküle oder Moleküle in unmittelbarer Nähe beteiligt sind, delokalisiert werden. Dies führt zu veränderten Dissipationswegen für optisch angeregte Zustände bzw. zu einer kompetitiven nicht-radiativen Relaxation. Da der Protonentransfer mit der Bewegung eines Kerns einhergeht, ist dieser Prozess per Definition mit einer atomaren Strukturveränderung verbunden. Der Prozess beinhaltet auch eine Ladungsverschiebung mit Veränderungen der räumlichen Position der Protonen. Hierbei entstehen elektrische Felder, die an das Gitter koppeln und eine Reorganisation desselben bewirken, um die mit dem Protonentransfer verbundene Ladungstrennung zu stabilisieren. Studien zur strukturellen Dynamik in Verbindung mit supramolekularen Wechselwirkungen in der festen Phase sind selten, da der optische Zugang zu solchen Reaktionsprozessen begrenzt ist. Bei den für spektroskopische Untersuchungen geeigneten Systemen bietet die ultraschnelle Spektroskopie eine Möglichkeit, die relevanten elektronischen sowie Schwingungsmoden zu beobachten, die zur Verfolgung der Dynamik des Protonentransfers optisch aktiv sind. Allerdings müssen die spezifischen atomaren Bewegungen abgeleitet werden, die zu den beobachteten Veränderungen der angeregten elektronischen und vibronischen Zustände sowie der Schwingungsrelaxation entlang der Reaktionen führen. Diese Informationen sind jedoch aktuell unvollständig. Mit den ultrahellen Elektronenquellen ist es nun möglich, Pump-Probe-Methoden in Form von ultraschneller Beugung zu erweitern, um die atomaren Bewegungen direkt zu verfolgen. Bei Protonentransferreaktionen ergibt sich dadurch die Möglichkeit, die Protonenbewegung direkt zu beobachten, die an einer der klassischen chemischen Reaktionen von Säure-Base-Reaktionen bis hin zur Protonenverschiebung bei der Energietransduktion in biologischen Systemen beteiligt ist.

Eine der Schwierigkeiten bei der Beobachtung der photoinduzierten Reaktion in Molekülkristallen ist die Probenvorbereitung. Hierbei muss die Kristallprobe dünn genug sein, damit die Strahlen zur Eindringung im Bereich Einkristalls generiert und untersucht werden können. Als ersten Schritt für mein Promotionsvorhaben wurde eine einfache Kristallzüchtungsmethode entwickelt, um große und dünne Kristalle von Dihydroxyanthrachinon (DHAQ)-Derivaten zu erhalten: 1,5-, 1,8-, und 1,4-DHAQs. Hierbei hat sich ergeben, dass 1,5- und 1,8-DHAQ in Lösung einen intramolekularen

Protonentransfer im angeregten Zustand (ESIPT) durchlaufen, während 1,4-DHAQ überschüssige Energie überwiegend auf andere Weise als durch ESIPT abbaut. Ziel ist die maximal sensitive Beobachtung der photochemischen Reaktionsdynamik in den Systemen, die durch das umgebende kristalline Bad beeinflusst werden, mit Hilfe von transmissionsbasierten ultraschnellen optischen und Elektronenbeugungsexperimenten. Als Strategie für dünne und große Kristalle wurden überlappende Schichten eines transparenten dielektrischen Substrats auf die Kristallisation aus übersättigten Lösungen angewandt, um den Kristallisationsraum zweidimensional zu begrenzen. Die Verdampfung des Lösungsmittels in dem eingeschränkten Raum führte dazu, dass die Kristalle zu dünnen (1 - 1,75 μm) und großflächigen (> 100 μm) Formen heranwuchsen. Diese Methode kann auch auf andere π -verzweigte planare organische Moleküle angewendet werden.

Die mittels XRD bestimmten Kristallstrukturen zeigten das Vorhandensein von intermolekularen Wasserstoffbrückenbindungen in 1,5- und 1,4-DHAQ-Kristallen. Außerdem weist die Berechnung der Coulomb'schen Kopplung zwischen den Übergangsdipolmomenten benachbarter Moleküle starke Kopplungen in 1,5- und 1,4-DHAQ-Kristallen und schwächere Wechselwirkungen in 1,8-DHAQ-Kristallen auf. In der Arbeit wurden darüber hinaus die Abhängigkeit der verschiedenen intermolekularen Wechselwirkungen von den Derivaten sowie die Auswirkung der Kristallstruktur auf die photochemischen Reaktionen mithilfe von transienten Femtosekunden-Absorptionsmessungen untersucht. Die Dynamik der angeregten Kristalle zeigt gegenüber den vergleichbaren Lösungen deutliche Veränderungen der angeregten Zustände in 1,5- und 1,4-DHAQ-Kristallen, während die Dynamik zwischen 1,8-DHAQ-Kristall und den entsprechenden Lösungen sehr ähnlich ist. Hierbei wird vermutet, dass die intermolekularen Wasserstoffbrückenbindungen und die starken exzitonischen Kopplungen in den Kristallen neue nicht-radiative Relaxationspfade in 1,5-DHAQ schaffen und möglicherweise einen Protonentransferkanal in 1,4-DHAQ öffnen. Diese Ergebnisse deuten darauf hin, dass eine neue chemische Eigenschaft in ein molekulares System eingeführt werden kann, indem die Moleküle auf eine bestimmte Weise gestapelt werden. Dadurch wird die Möglichkeit nahegelegt, die photochemische Aktivität von Molekülen in der kristallinen Phase zu steuern. Außerdem ebnet diese Arbeit den Weg zur atomaren Auflösung der Protonenbewegungen in Verbindung mit Skelett- und Gittermoden durch ultraschnelle Elektronenbeugungsexperimente.

ABSTRACT

Photoinduced proton transfer is one of the most basic reactions in photo-(bio)chemistry. The mechanism of this reaction is also of great interest for organic optoelectronics. For most chemistry, reactions involving organic molecules occur in condensed phase, i.e., liquid and solid, not in isolated molecular systems. The host medium for condensed phase processes enables high collision frequencies and faster reaction rates than possible in gas phase. The nature of the bath also influences the reaction pathway by interacting with the system. The uncorrelated degrees of freedom in the solid phase is by definition less than that in the liquid phase. This difference reduces confusion in the modes coupled to the reaction coordinate and offers more control of the bath in terms of tuning the chemistry. In addition, the electronic states involving aggregated molecules or molecules in close proximity, defined by the lattice structure, can be delocalized, leading to modified dissipation routes for photoexcited states and competitive nonradiative relaxation. Since proton transfer involves motion of a nuclei, this process fundamentally involves structural changes at the atomic level. The process also involves displacement of charge with changes in the proton spatial position, which creates electric fields that further couple to the lattice to cause lattice reorganization to stabilize the charge separation involved with proton transfer. Studies of the structural dynamics coupled with supramolecular interactions in solid phase are rare due to limitations in optically accessing such reaction processes.

For the systems amenable to spectroscopic studies, ultrafast spectroscopy provides a means to track the relevant electronic and vibration modes that are optically active to track the proton transfer dynamics. However, one must infer the specific atomic motions giving rise to the observed changes in excited electronic and vibronic states, and vibrational relaxation along reaction coordinates. This information is incomplete. With the advent of ultrabright electron sources, it is now possible to extend ultrafast pump-probe methods in the form of ultrafast diffraction to directly observe the atomic motions involved. For proton transfer reactions, we have the opportunity to directly observe proton motion involved in one of the most classic chemical reactions that is central to acid base reactions to proton translocation in energy transduction for biological systems.

One of the huddles to observe photoinduced reaction in molecular crystals is sample preparation. The crystal sample is required to be thin enough for pump and probe beams to penetrate within the area of the single crystal. As the first step for my doctoral project, I have designed a simple crystal growth method to obtain large and thin crystals of dihydroxyanthraquinone (DHAQ) derivatives: 1,5-, 1,8-, and 1,4-DHAQs. In solution, 1,5- and 1,8- DHAQs are known to undergo excited state intramolecular proton transfer (ESIPT), but 1,4-DHAQ tends to dissipate excess energy through other ways than ESIPT. The aim is to observe the photochemical reaction dynamics in the systems influenced by the surrounding

crystalline bath using transmission-based ultrafast optical and electron diffraction experiments for maximum sensitivity. The strategy for thin and large crystal growth used overlapping sheets of transparent dielectric substrates which acted to confine crystallisation from supersaturated solutions to selectively direct two-dimensional growth. The constrained evaporation of the solvent in the confined space guided the crystals to grow into thin (1 – 1.75 μm) and large area (> 100 μm) shapes. This method holds great promise to be applicable to other π -stacking planar organic molecules for developing samples specifically for ultrafast electron diffraction – to directly map the atomic motions involved in proton transfer.

The crystal structures as determined by XRD revealed the existence of intermolecular hydrogen bonds in 1,5- and 1,4-DHAQ crystals. Furthermore, the calculation of the Coulombic coupling between transition dipole moments of adjacent molecules in the lattice, using the crystallographic data, predicts strong couplings in 1,5- and 1,4-DHAQ crystals and weaker interactions in 1,8-DHAQ crystal. I investigated how the different intermolecular interactions depend on the derivatives and how crystal structure impacted on the photochemical reactions using femtosecond transient absorption measurements. The excited state dynamics of the crystals compared to their respective solutions reveal distinctively modified excited state dynamics in 1,5- and 1,4-DHAQ crystals, whereas the dynamics in 1,8-DHAQ crystal and solution are very similar. The intermolecular hydrogen bonds and strong excitonic couplings in crystals are suggested to create new non-radiative relaxation pathways in 1,5-DHAQ and possibly open a different proton transfer channel in 1,4-DHAQ. These results imply that new chemistry can be introduced into a molecular system via stacking of the molecules in a specific way and suggests the ability to tune photochemical activity of molecules in the crystalline phase. The ultimate goal of this research has been achieved. This work paves the way to atomically resolve the motion of protons coupled with skeletal and lattice modes by ultrafast electron diffraction experiments.

Chapter 1. Introduction

Elementary chemical reactions involve charge and energy redistribution within the various electronic and nuclear degrees of freedom of the reactants, which may subsequently lead to bond breakage, charge transfer or other chemical processes forming product states with different nuclear and electronic configurations. The transfer of a negatively charged particle, the electron, is a common elementary reaction. An electron bound to a nucleus (or nuclei) can be transferred to other nuclei through barrier crossing processes related to the potential energy barrier separating reactant and product surfaces. The electronic charge redistribution induces the nuclei of both the intramolecular and intermolecular coordinates to new nuclear configurations in a process called nuclear reorganization. In an analogous way, positive electronic charge transfer is carried out by protons. Proton transfer reactions often occur in inter- or intramolecular hydrogen bonded systems. It is a similar process to electron transfer in the sense that both these charged particles involve sampling different nuclear fluctuations and rearrangements that stabilize the charge separation or formation of a charge transfer state. However, the much heavier mass of the proton relative to the electron reduces the spatial extent of the wavefunction describing the proton probability distributions. The spread of the wavefunction is influenced by interaction with the surroundings, such as solvents or lattice structure, which in principle is more amenable to control.

Proton transfer has been a great interest for chemists and biologists because it is a key elemental process in many chemical and biological reactions, such as acid-base reactions, photosynthesis and phosphorylation of ADP to ATP [1]. After the structure of DNA was revealed, which showed that the double helix is constructed with hydrogen bonds [2], implication of proton transfer at the hydrogen bonds between nucleic acid as a basis for mutation, aging, and tumorigenesis has been actively discussed [3-5]. The role of prototropic tautomerism, isomerism caused by proton transfer, in RNA has been studied using quantum mechanical calculations, spectroscopic approaches such as NMR or 2D IR, and X-ray crystallography [6].

Intramolecular hydrogen bonding systems can go through excited state proton transfer reactions. In the field of photochemistry, excited state intramolecular proton transfer (ESIPT) is known to provide photostable decay pathways for hydroxyanthraquinone based organic pigments by dissipating the absorbed photon energy through a reversible process faster than irreversible degradation [7, 8]. This pathway involving proton transfer relaxation of excited states is responsible, fortunately, for the long-lived pigments used in some of the great art works. Thanks to the improvement of ultrafast laser spectroscopic techniques followed by the development of self-mode-locked femtosecond laser pulse

technology [9], the reaction time scale of ESIPT has been fully resolved temporally to be in the range from sub-picosecond to several ps [10-15] or in a few cases in nanoseconds [16].

Since the proton transfer dynamics involve displacement of a nucleus (i.e., a proton), it is strongly coupled to the vibrational modes of the molecular system as well as interaction between the system and its surrounding bath. For instance, skeletal motions in green fluorescent protein are intimately involved in the ESPT process, which produces bioluminescence [17]. The effect of solvent on ESIPT dynamics has been studied to determine the role of system-bath interactions in solution and to rationalise the reaction dynamics [18-23]. Single crystals or solid state host media, where the molecules are arranged by Van der Waals forces, provides a very different environment for the molecular reaction dynamics [24]. The interaction between transition dipole moments of the close packed molecules possibly modifies the intrinsic reaction pathway(s).

In this thesis, hydroxyanthraquinone (HAQ) derivatives were chosen as a model system to study the ESIPT structural dynamics in single crystals. They have been candidates for ESIPT studies for decades. The previous research work on ESIPT in HAQs will be briefly reviewed in chapter 2. The ESIPT active molecules including HAQ hold great promise for photonic device applications due to their unique energy states, which will also be described in chapter 2. Tunability of the ESIPT reaction by crystal engineering has been investigated: modulation of the emission wavelength by switching the intramolecular hydrogen bond to the intermolecular hydrogen bond driven by molecular packing was observed [25], enhancement of the fluorescence quantum efficiency in ESIPT molecules by proper design of crystal structures was proposed with first principle calculations [26], and crystallization-enhanced emission in complex ESIPT molecular system was demonstrated using steady state and time-resolved fluorescence measurements [27]. However, fundamental insight to the structural dynamics involving ESIPT in the crystalline phase is still missing, especially with respect to direct observation of the structural changes coupled to the proton motion.

Ultrafast spectroscopic techniques enable resolving electronic structural dynamics of excited states. Probe pulses after variable time delays between the excitation and pump pulses on a target molecular system provide a set of spectra, from which transient electronic features are extracted. Those features include both photophysical and photochemical information. To connect the resulting spectroscopic determined evolution in the chemical reaction to specific structural changes requires direct observation of the atomic motions to ensure all motions, including those not involving optically active states, are resolved. Due to the charged nature of electrons as a structural probe, electron pulses are sensitive to the motion of hydrogen atoms, including protons, by probing nuclei directly via the Coulomb interaction [28]. Thus, time-resolved electron diffraction is truly a unique probe of proton transfer reactions. Crystals thin enough for transmission studies is the best option for the highest sensitivity, compared to

low energy diffraction from surface layers. The signal grows quadratically with thickness until a limit where inelastic scattering reduces the transmitted electron intensity as well as obscures the diffraction process. The temporal resolution in ultrafast electron diffraction (UED) is another consideration because of the velocity mismatch between the excitation (photon) pulse and probing electron pulse [29]. For typically thickness of less than 100 nm, this broadening of the temporal resolution is negligible (less than 10 fs broadening). Therefore, to measure the electronic and nuclear structural dynamics of excited states using ultrafast spectroscopic and diffraction methods, single crystal samples larger than the pump and probe beam sizes and thin enough to transmit the electron beam are required. Furthermore, the thickness restriction depends on the probing methods. For transmission-based optical spectroscopy, the crystal needs to be thinner than its optical penetration depth. For electron diffraction, the elastic mean free path of electron pulses, which depends on the electrons' energy and Z value of the constituent atoms in the sample, determines rather demanding micron to submicron thickness [30]. For instance, for 100 keV electron beam, roughly less than 100 nm is allowed for inorganic compounds and a few 100 nm is still acceptable for pure organic materials, and relativistic electrons accelerated by MeV accepts even thicker samples, up to 1 μm [31].

Various methods for thin single crystal preparation have been developed especially after transmission electron microscopy became one of the main tools for microstructure observation [32]. The methods can be categorized into two ways: top-down and bottom-up approaches. Top-down methods such as mechanical, electrochemical, or ion-beam milling, erode bulk crystals. Those milling techniques demand precise effort to evenly prepare surfaces in large area (>100-micron diameters) and the milling process can cause degradation of compounds in soft materials. Microtomy is a sectioning method using a glass or diamond knife. This method limits samples to water-insoluble classes of crystals and the shear stress while cutting can cause deterioration in crystal uniformity [33]. Bottom-up process use chemical or physical forces to assemble building blocks, i.e., atoms or molecules. For example, vapour deposition methods such as atomic layer deposition and physical or chemical vapour deposition are well developed typically for thin crystal growth [34]. The key to obtain thin crystals with the bottom-up process is to control the growth kinetics in an anisotropic way. In this PhD thesis work, evaporation of supersaturated solution is adopted as the crystallisation framework. For kinetic control, a two-dimensional (2D) spatial confinement method is applied. The as-grown thin HAQ crystals on optically transparent substrate (in the visible region of the spectrum) can be used for the transmission-based ultrafast spectroscopy measurements without any additional treatment, as done in this thesis work.

The aim of this work is to unravel ESIPT dynamics in prototypical molecular systems coupled with intermolecular interactions in crystalline phases using femtosecond transient absorption (fs TA) and state-of-the-art electron diffraction techniques. The HAQ crystals obtained using spatial confinement methods are characterized using microscopic and diffraction methods followed by steady state optical

measurements. A few preliminary electron diffraction studies for UED, using transmission electron microscope to characterize the diffraction quality, were also performed. In addition, the excitonic couplings in crystal are calculated to decipher the role of intermolecular interactions in modifying the nature of electronic transitions. This point is important to establish as the nature of the initial state is required to define the reaction pathway. Lastly the excited state dynamics of HAQs in solution and crystalline phase are observed by fs TA measurements. Systematically integrated studies of several derivatives of HAQ in solution and crystals provides unprecedented insight to the effect of intermolecular interactions on ESIP dynamics in crystals.

Chapter 2. Review of Literature

When a molecular system is irradiated with light, the system goes through photophysical processes such as primary absorption, emission, intersystem crossing, internal conversion, and so on. Chemical reactions can also be triggered by the absorption of photons by providing competing pathways with the deactivating photophysical processes. The examples of photochemical reactions are ionization, electron transfer, proton transfer, dissociation, and structural transformation such as photoisomerization, which create other energy relaxation pathways than physical deactivation of excited states. In this chapter, the photophysics of isolated molecular systems and molecular crystals and photo-induced intramolecular proton transfer reactions are introduced. The central role of the system-bath interactions on ESIPT is reviewed. Finally, ESIPT-related photophysical and photochemical dynamics of hydroxyanthraquinones, the model system to study ESIPT dynamics in a crystalline bath, are reviewed.

2.1 Photo-induced transitions in molecular system

Electronic structure of molecular systems can be accurately constructed by molecular orbital (MO) theory for small to moderately large systems such as hydroxyanthraquinones, where electrons are depicted throughout the molecule in terms of probability distribution for particular electronic states. MO theory mathematically describes the wavefunctions for electrons in a molecule. The quantized energies of an electron of hydrogen can be determined exactly and full eigen spectrum of the time-dependent Schrödinger equation calculated. However, solving the equation for molecules is not possible due to the mathematically intractable problem in separating spatial variables for more than 1 electron – the well-known two body problem. Various perturbation methods are used to address electron-electron correlations in their respective motions. The nuclear positions also strongly influence the electron distribution. To separate nuclear and electronic degrees of freedom, the Born-Oppenheimer (BO) approximation is adopted to simplify the calculation, i.e., the nuclei are treated as stationary while electrons are moving in the potential defined by the frozen positions of the nuclei. This approach is well justified as the mass of the nuclei is much heavier than that of electron; the nuclei move orders of magnitude slower than electrons. This insight enables the electronic energy diagram to be drawn as a function of the internuclear distance.

The highest energy level filled with electrons is called the HOMO (highest occupied molecular orbital) and the next level above the HOMO is called the LUMO (lowest unoccupied molecular orbital). By absorbing photon energy, an electron in the HOMO can be excited to higher energy levels. The excitation of an electron to higher energy levels is referred to as an electronic transition, and the transition from the ground state to the first excited state by absorbing a photon at the corresponding

energy difference is called the primary absorption. In conjugated molecules the HOMO is typically a π orbital constructed by overlapping p orbitals of carbons. The LUMO is typically a π^* state, and the resulting lowest energy electronic transition will be π - π^* transition. The electronic structure of molecules is reflected in the absorption spectrum leading to the creation of excited states.

Since atoms in a molecule vibrate about their bonds, electronic and vibrational states are strongly coupled in molecular spectra. Therefore, vibrational levels are associated with each electronic state and are referred to vibronic states. The associated energy diagram is expressed with configuration coordinates to represent energy levels regarding the normal vibrational modes with anharmonic couplings to take into account nonradiative relaxation of the strongly coupled electronic and vibrational degrees of freedom in molecules. The equilibrium modes at each electronic level are not identical. In the Frank-Condon principle, a similar postulate as the BO approximation, the motions of the nuclei are relatively slow compared to that of the electron and associated optical transition to an upper excited state. The absorption of a photon is illustrated as a vertical transition (frozen nuclear coordinates) to illustrate the transition process. When an electron is promoted to the excited state by absorption, the nuclei of the molecule are left in the equilibrium configuration at the ground state and the overall transition probability is weighted by the joint probability for the same nuclear configuration in the excited state. This principle explains the vibronic progression or different intensities in the absorption or emission of photons related to transitions involving vibronic levels. The molecule or system relaxes from the excited vibronic levels by non-radiative relaxation process involving anharmonic coupling between vibrational modes to lead statistically to the lowest vibrational mode before transitioning back to the ground state through a nonradiative process referred to as internal conversion. The electronic transition to the ground state can also occur by radiating a photon, which for spin conserved or spin allowed processes, is called fluorescence. This process typically occurs on 10 ps to ns timescales and ultimately limits the excited state lifetime. The excited electronic state can also intersect with other electronic surfaces involving different nuclear configurations that lead to chemical transformation. The photochemistry of interest in this thesis work occurs in competition with these other radiative and nonradiative channels within the electronic manifold of the initially created excited state.

With respect to spin state considerations, the HOMO with full complement of electrons has a spin quantum number $S = 0$, which results the number of spin states $2S + 1 = 1$. The state is referred to as a singlet. Singlet states are denoted as S_0, S_1, S_2, \dots , from the ground state. Photons can excite electrons only to the same spin states because they do not have magnetic field frequencies resonant with electron spin transitions as like, i.e., transitions from S_0 to S_n are referred to as “allowed transitions. The excited states can have $S = 1$ as well, for processes leading to unpaired electrons at excited and ground electronic states (weak optical transitions or nonradiative relaxation). This overall spin angular momentum gives the multiplicity of the spin states to be 3, in other words, triplet states. In presence of spin-orbit coupling,

transitions from singlet to triplet state can happen. In the case of nonradiative relaxation, the transition is called intersystem crossing (ISC). The excess energy will then dissipate into heat along vibrational states associated with T_1 . Returning radiatively to S_0 from T_1 is also induced by spin-orbit coupling, requiring a change in spin breaking the selection rule for spin conservation during optical transitions. Therefore, the photon emission by the decay via T_1 states is generally much slower (microsecond to millisecond) than radiative relaxation involving fluorescence. Given the different nature of this radiative transition it is distinguished from the spin allowed fluorescence and denoted as phosphorescence.

So far, the different photophysical pathways of isolated molecules have been discussed. In condensed state, i.e., in liquids or solids, molecules interact with their bath, which results in distinguishable features in their optical spectra. In molecular crystals, the excitation of a molecule generates an unpaired electron at a higher energy level and the vacancy in the lower electronic level can be treated as a hole with positive charge. This concept is similar to electron-hole carriers in semiconductors. The resulting electron and hole are tightly bound by their mutual Coulomb interaction, which is regarded as one excited quasi particle called a Frenkel exciton. Frenkel excitons are localized at a molecule, so the binding energy is stronger than free excitons in semiconductors [35]. The electron and hole wavefunctions in molecular systems are strongly correlated in space. Their respective spatial envelope wavefunctions overlap. Frenkel excitons can propagate through a crystal through transitions involving dipole-dipole coupling between molecules in either coherent or incoherent hopping processes between molecules for the spatial transport of the excited state energy. Specifically, the excitation energy migrates spatially by the dipole-dipole coupling between two molecules (M_1 and M_2):



where * means excited species, or “excitation waves” [36]. Since the Coulombic dipole-dipole coupling depends on the distance and angle between constituting molecules in a crystal, Frenkel excitons are coupled with low-frequency lattice vibrations (phonon modes) or high-frequency intramolecular vibrations that modulate the distance and associated coupling between molecules.

2.2 Photo-induced chemical reactions in molecular systems

Photo-excited molecules go through not only the photophysical pathways described above but also can experience chemical reactions, for example, ionization, electron transfer, dissociation, abstraction, isomerization, or rearrangement. Those reactions can compete with radiative and nonradiative decay pathways, and even dominate, if the photochemical reaction rate is faster than the fluorescence or nonradiative lifetime of the excited state. In other words, photochemical reactions are another non-radiative deactivation process distinct from internal conversion within the same electronic manifold. Among the photochemical reactions, I focused on intramolecular proton transfer in this thesis.

2.2.1 Excited State Intramolecular Proton Transfer (ESIPT) Reaction

The first experimental finding of ESIPT was the large Stokes shift in salicylic acid by Weller in 1955 [37]. He explained the large shift with the potential energy picture with the proton transfer coordinate based on Lippincott-Schröder model [38]. For instance, the ground state potential energy of a molecule having an intramolecular hydrogen bond between the ketone and enol groups can be drawn as an asymmetric double well along the hydrogen bond length coordinate (Figure 2.1). N indicates normal form of a molecule and T indicates intramolecular-proton-transferred form of the molecule. The potential energy N is lower than T, but at the first excited state (N^* and T^* , respectively), some molecules have inverted energy levels. Due to this four-level system, molecules promoted to N^* by absorbing a photon nonradiatively relax through a chemical reaction to T^* in competition with the radiative relaxation. In [38], Weller suggested that the ESIPT in salicylic acid is faster than nanoseconds, the timescale of fluorescence ($N^* \rightarrow N$), because the intensity of red-shifted emission associated with the ESIPT dominated.

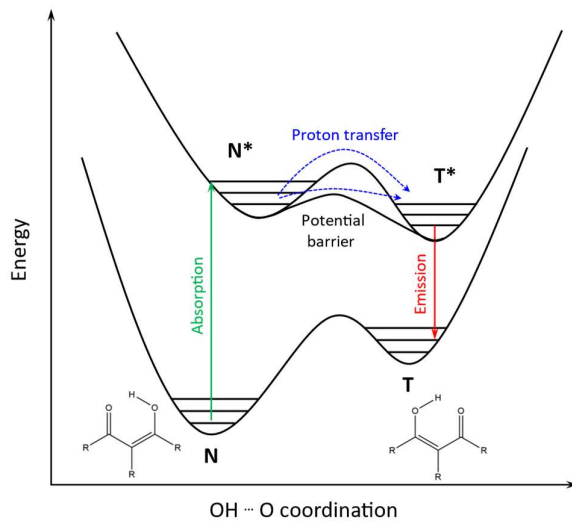


Figure 2.1. Energy diagram of ESIPT with chemical coordinate of the distance of $\text{OH}\cdots\text{O}$. The probability of photo-excited tautomerization depends on the potential barrier.

The rate of ESIPT reactions depends on the barrier along the potential energy surface (PES), which is influenced by low-frequency vibrational modes of the surrounding atoms coupled with their bath [39]. The dynamics of ESIPT has been studied by ultrafast spectroscopic methods on various molecular systems. Herek et al. observed ESIPT in gas-phase methyl salicylate taking place in faster than 60 fs [10], and Laermer et al. found the ESIPT lifetime of 2-(2'-hydroxyphenyl)benzothiazole occurring in 170 fs in nonpolar solvent [40]. Itoh et al. observed a slower proton transfer rate (~300 fs) for 3-hydroxyflavone (3-HF) in polar solvent, 2-methyltetrahydrofuran, possibly due to torsional motion of phenyl group and longer distance in the intra- and intermolecular hydrogen bond coordinate [41]. Those observations suggest femtosecond timescales for the ESIPT reactions, however, even slower ESIPT reactions have been observed in some systems. The proton transfer in 6-amino-2-(2'-hydroxyphenyl)benzoxazole and 2-(2'-methoxyphenyl)benzoxazole solution occurs from 1.2 ps to 35 ps depending on solvents, where the ESIPT dynamics is governed by intramolecular charge transfer reaction [42]. Joshi et al. reported nanosecond timescale of ESIPT in 3-hydroxyisoquinoline solutions [23].

From the above discussion, it can be appreciated that the system-bath interaction plays very important role in chemical reactions [43], therefore, solvent effects have been investigated extensively in ESIPT dynamics. Smith and Kaufmann investigated the solvent dependence on the rate of nonradiative decay due intramolecular proton transfer in methyl salicylate using picosecond laser spectroscopy [44]. They reported that the dielectric strength of the solvent is correlated to the lifetime. McMorrow and Kasha proposed the effect of hydrogen bonding impurities in hydrocarbon solvents on the ESIPT path in 3-HF [45], and Strandjord and Barbara found the slow proton-transfer component of 3-HF is dependent on the hydrogen-bond-donating ability of the solvent [46].

When the bath is crystalline, the interactions between molecules in the ordered lattice perturb the electronic structure and vibrational and rotational modes, and the various photophysical processes can be influenced when chromophores are in close contacted [47]. In case of ESIPT reaction, since the motion of proton is strongly coupled with the surroundings, delocalized excitations within the crystal lattice, the bath, possibly influence the photochemical pathway. Khatib et al. reported that photoactivity of proton transfer reaction in crystals of 2-(2,4-dinitrobenzyl)pyridine derivatives, which were found to be dependent on molecular packing. They suggested that π - π interactions in π -stacked crystals open other deactivation routes faster than ESIPT [48]. The effect of crystal packing on ESIPT process has been utilized in optoelectronics engineering field: Qian et al. showed enhanced emission of N,N'-di[3-Hydroxy-4-(2'-benzothiazole)phenyl]5-tert-butyl-isophthalic amide (DHBIA) and N,N'-di[3-Hydroxy-4-(2'-benzothiazole)phenyl]isophthalic amide (DHIA) nanoparticles compared to solution

[49]. The enhancement of DHBIA was higher than DHIA, which was attributed to J-aggregation inducing a higher ESIPT quantum efficiency (Φ_{ESIPT}) than H-aggregation, based on their molecular modeling. Cheng et al. showed some 2'-hydroxychalcone (2HC) derivatives exhibited fluorescence from ESIPT in crystals which were not emissive in solution [50]. Dommett et al. theoretically investigated electronic structure of two 2HC derivatives in gas and crystal phase, and suggested substituents and the degree of distortion allowed in the crystal determine the pathways of ESIPT coupled to aggregation induced emission (AIE) [51].

As introduced above, the properties of the ESIPT active molecules in crystal phase have been studied and applied to organic optoelectronics [52-54]. However, the ESIPT process is a chemical reaction, which is dynamic. The fundamental studies on the dynamics of ESIPT reactions with consideration of crystalline bath effects is rather limited. To name a few, Wu et al. measured (E)-3-(4-(dimethylamino)phenyl)-1-(1-hydroxynaphthalen-2-yl)prop-2-en-1-one (DMHC) nanowire arrays using fs fluorescence and TA methods to demonstrate near-infrared lasing with ESIPT-active organic solids [55]. Their analysis on excited state dynamics of DMHC crystals revealed the timescale of ESIPT in a few ps and faster emission process in crystal than in solution indicating the crystal bath boosted stimulated emission from the tautomer form rather than nonradiative decay. Towrie et al. studied transient vibrational changes of the C=O and C=C modes in 1,5-dihydroxyanthraquinone solution and solid particle in nujol (a kind of mineral oil) mull, to suggest quenching of the ESIPT channel in the presence of additional energy dissipation pathways, or stronger lattice coupling, in the solid state [56]. In this thesis, I investigate the influence of the lattice bath on photo-induced proton transfer reaction dynamics compared to the reaction dynamics in solution as the bath with hydroxyanthraquinone derivatives as model systems.

2.2.2 Hydroxyanthraquinone derivatives

Hydroxyanthraquinones are derivatives of 9,10-anthraquinone where hydrogen atoms are substituted for hydroxyl groups. Hydroxy groups at 1-, 4-, 5- or 8-positions form hydrogen bonds with the 9- or 10- keto group. The hydrogen bonds are the key infrastructure for ESIPT process, but they do not always allow the process. The variation of the position of the hydroxy groups diversifies the potential energy surface of molecular systems, which either open the paths for proton transfer reactions or not. The differences with structure are significant in this regard. In other words, the dynamics of this intramolecular chemical reaction is highly coupled with motions in the skeletal geometry [57].

Based on the existing knowledge of the ESIPT activity of hydroxyanthraquinones, 1,5-, 1,8-, and 1,4-DHAQs, these systems are chosen as the model systems to study ESIPT dynamics in crystals. The molecular structures of these systems are depicted in Figure 2.2. The system, 1,5-DHAQ, is known to

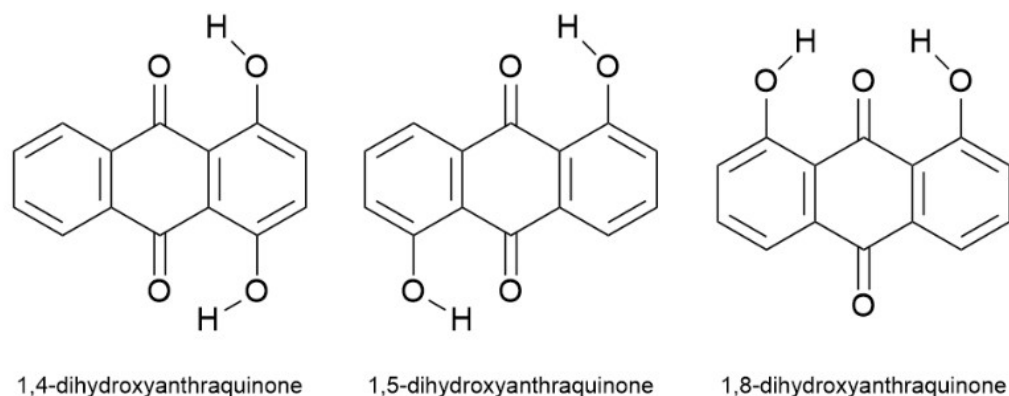


Figure 2.2. Molecular structure of 1,4-, 1,5-, and 1,8-dihydroxyanthraquinone.

exhibit ESIPT reactions both in solution and crystalline phase by photoexcitation in the visible range, with evidence of dual fluorescence [58, 59]. Steady state absorption, fluorescence, and Raman excitation spectra on 1,8-DHAQ solution and powder by Smulevich et al. suggested solid state 1,8-DHAQ as well as solution phase undergoes ESIPT processes [60-62]. Carter et al. and Benthem et al. compared fluorescent features of 1,4- dihydroxyanthraquinones (1,4-DHAQ) and 1,5-DHAQ and investigated the change in intramolecular hydrogen bonding by comparing with deuterated isotopes [58, 63]. They found no evidence of ESIPT in 1,4-DHAQ, whereas difference in the electronic spectra of 1,5-DHAQ by deuteration was observed. They also proved two proton transfer is unlikely in 1,5-DHAQ by comparing spectra for 1-HAQ. Theoretically, Zheng et al. studied photoinduced ESIPT dynamics of anthraquinone derivatives in solution combining time dependent density functional theory (TDDFT) and atoms in molecules (AIM): the ESIPT process is barrierless in 1,5-DHAQ, the reaction of 1,8-DHAQ is sensitive to the solvent, and for ESIPT the energy barrier was high for 1,4-DHAQ [64].

To review the excited state dynamics in the three systems, first with 1,5-DHAQ, Towrie et al. compared time-resolved IR spectra of 1,5-DHAQ solution in chloroform and solid powder [56]. They observed a fluorescence lifetime of 402 ps in solution phase and quenching of the transient C=O band in solid phase which was assigned to an ESIPT state in the solution spectra. They suggested internal conversion dominates rather than proton transfer for relaxation in solid state. On the other hand, Wei et al. observed dual fluorescence with dispersed 1,5-DHAQ micro crystals and measured time-resolved fluorescence up-conversion, reporting that lifetime of emission band is in sub-nanoseconds time scales, while an emission peak at 575 nm has an additional fast decaying component with a lifetime of 1.4 ps [59]. They inferred this picosecond decay to be evidence of the proton transfer pathway, as the sub-nanosecond decay is from fluorescence.

The time-resolved fluorescence of 1,8-DHAQ solution in hexane showed instantaneous dual fluorescence indicating ESIPT occurred in 50 fs and spectral change in some ps time domain, which

was assumed to be an additional proton translocation followed by the barrierless proton transfer reaction [65]. The timescale of ESIPT in 1,8-DHAQ solution in benzyl alcohol was observed to be 300 fs by the rise time of stimulated emission in fs-transient spectroscopy [66]. Mohammed et al. suggested equilibration processes between normal and tautomerized form while vibrational relaxation in 0.1 – 50 ps time scale by time-resolved electronic and vibrational spectroscopy and computational modelling of 1,8-DHAQ in several solvents. They conjectured that the solvent's role in the intramolecular hydrogen bond during the excited state decay was to promote either relaxation to the ground state or triplet state from the deviated spectral feature and much longer decay time with protic solvent [67].

Berenbeim et al. investigated excited state lifetimes of 7 derivatives of hydroxyanthraquinones in gas phase generated by jet-cooled molecular beam methods, which are classified into “with” and “without” the 1,4-hydroxyl structural motif [8]. The comparably longer excited state lifetime in 1,4-motif molecules was theoretically explained by calculating the potential energy surface of gas phase 1-hydroxyanthraquinone (1-HAQ) and 1,4-DHAQ. In the excited state potentials of in 1-HAQ, the intersection of $\pi\pi^*$ and $n\pi^*$ surface let the excited molecule dissipate the energy along the proton transfer coordinate. However, the OH group at the position 4 in 1,4-DHAQ stabilises the $\pi\pi^*$ state below $n\pi^*$ state, resulting in relaxation only from $\pi\pi^*$ state to the ground state.

Despite the numerous studies of ESIPT processes in HAQs, experiments with HAQ crystals larger than typical probe spot sizes have not been reported. Powdered solid molecules or dispersed microcrystals have scattering issues in optical measurements and are insufficient to draw precise information of structural change from diffraction studies. One of the major limiting steps in single crystal sample preparation is to obtain large area crystals, which are thin enough to perform transmission-based measurements. Therefore, I started with developing the strategy to grow thin and large HAQ crystals to study their ESIPT dynamics in crystalline phase using femtosecond spectroscopy and electron diffraction.

Chapter 3. Theoretical Framework

This chapter describes the experimental and theoretical methods. First, the strategy to prepare thin molecular crystal samples suitable for transmission-based measurements is introduced starting from classical nucleation theory to the 2D spatial confinement technique, followed by the description of methods for crystal characterization. Next, quantum chemical calculation methods for predicting the resonant excitations and the excitonic couplings is introduced. Lastly, the fs transient absorption method for measuring the excited state dynamics is explained.

3.1 Thin crystal growth for transmission-based measurements

Time-resolved experiments are preferred with transmission-based measurements than reflection methods to pursue high time resolution. The main difference is the sensitivity. Reflection studies limit the interaction zone of the probe to the surface region and the resulting signal involves fewer molecules and correspondingly less signal than in transmission sampling of orders of magnitude more optically modulated molecular spectra. In terms of sample delivery for solution phase studies, the excitation fraction and S/N ratio of solution sample can be easily controlled by optimizing the concentration and path length. However, solid state samples have their characteristic optical penetration depth defined by the crystal density. There is no possibility to control the optical density other than crystal thickness. In addition, there are limits to the area of the sample for diffraction methods as mentioned in the introduction. This challenge was solved by exploiting the slow evaporation of supersaturated solution method aided with a new approach to 2D spatial confinement using overlapping mica sheets to obtain large and flat crystals.

Solvent evaporation is a simple and common method to grow molecular crystals. The main process of crystallization is nucleation and crystal growth. Nucleation occurs under metastable conditions for a system and can be described with classical nucleation theory. The driving thermodynamic force for the phase transformation from solution (state 1) to solid or single crystal form (state 2) is the chemical potential difference, $\Delta\mu$:

$$\begin{aligned}\Delta\mu &= \mu_1 - \mu_2 \\ &= (\mu_0 + RT \ln a) - (\mu_0 + RT \ln a^*) \\ &= RT \ln \frac{a}{a^*} \\ &= RT \ln S.\end{aligned}\tag{3.1}$$

μ_0 is the standard potential, a is the activity, a^* is the activity for a saturated solution, and S is the supersaturation ratio. For a non-electrolyte solute S is given by [68]:

$$\ln S = \frac{2\gamma v}{kTr^2} \quad (3.2)$$

where γ is the specific interfacial free energy between solid and liquid phase, v is molar volume of the solute, k is the Boltzmann constant, and T is the temperature in absolute units and r is the radius of a critical nucleation domains (Figure 3.1). The specific interfacial free energy, i.e., the surface energy, represents the change in internal energy of a two-phase system with change in internal area [69]. It has units of energy per unit area. The surface energies of crystals depend on the nature of the orientation of the crystal planes and the interfacing medium. The surface energies of crystalline faces can be estimated by DFT calculations using the slab model [70].

In the scenario of homogeneous nucleation, the total excess free energy between a nuclei and solute in solution, ΔG , is equal to the sum of the surface excess free energy, ΔG_s , and volume excess free energy, ΔG_v :

$$\Delta G = \Delta G_s + \Delta G_v = 4\pi r^2 \gamma + \frac{4}{3}\pi r^3 \Delta G_v, \quad (3.3)$$

where ΔG_v is free energy change of the transformation per unit volume. The radius at which ΔG has a maximum ($\Delta G/dr = 0$) is called the critical radius, r_c :

$$r_c = -\frac{2\gamma}{\Delta G_v}, \quad (3.4)$$

and this gives the critical excess free energy:

$$\Delta G_c = \frac{16\pi\gamma^3}{3(\Delta G_v)^2}. \quad (3.5)$$

ΔG_c can be written for supersaturation conditions by applying (3.2) and (3.4):

$$\Delta G_c = -\frac{16\pi\gamma^3 v^2}{3(kT \ln S)^2}. \quad (3.6)$$

The rate of nucleation J is expressed with Arrhenius reaction velocity equation:

$$J = A \exp(-\Delta G/kT), \quad (3.7)$$

where A is constant. By putting (3.6) into (3.7),

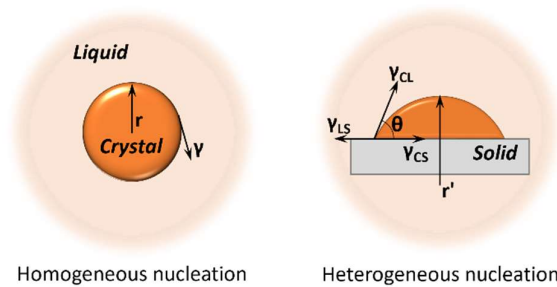


Figure 3.1. Radius of crystal and interfacial tensions in homogeneous and heterogeneous nucleation.

$$J = A \exp\left(-\frac{16\pi\gamma^3 v^2}{3k^3 T^3 (\ln S)^2}\right). \quad (3.8)$$

This implies that nucleation velocity is governed by surface energy, temperature, and supersaturation.

In realistic environments, the solution is contained in some vessel, and the solution contains impurities. The wall of the vessel and impurities disturb homogeneous nucleation, which in turn leads to heterogeneous nucleation with the factor ϕ :

$$\Delta G'_c = \phi \Delta G_c. \quad (3.9)$$

The factor ϕ is expressed with contact angle of crystal on a solid surface which is drawn in Figure 3.1 by Volmer's theory:

$$\phi = \frac{(2 + \cos \theta)(1 - \cos \theta)^2}{4}. \quad (3.10)$$

After nuclei are created and survive dissolution, they can grow to form crystals by solute molecules adsorbing on the surface of the nuclei. There are many theoretical crystal growth models to predict crystal growth rate and shape. Adsorption-layer theories first proposed by Volmer and modified by many others postulate solute particles form as an adsorbed layer on a crystal surface and describe the growth rate with supersaturation and temperature-dependent constants. Diffusion-reaction theories originated by Noyes and Whitney focus on diffusion and reaction near/on the surface of crystal during its growth. The details of all the growth modes are beyond this thesis. In brief, the growth process is governed by parameters such as concentration, solvent, temperature, cooling rate, temperature holding time, etc., so that the size and shape of crystals can be engineered by optimizing these parameters for a desired outcome within the limits of this relationship.

In this work, the 2D spatial confined growth method is applied to solvent evaporation crystallization to attain suitable dimensions of the target molecular crystals for optical measurements. The 2D spatial confined growth methods are well developed in the field of vapor phase growth of inorganic layer-structured materials, such as graphene or transition metal chalcogenides, to maximize their 2D properties by engineering growth morphology [71]. Basic knowledge of the method is to introduce spatial constraints to vapor or solution crystallisation, to modulate adsorption kinetics and growth direction. Diffusion and convection of vapor containing precursor, or those using evaporation of solution is restricted in the volume of a confined space. 2D spatial confinement is adopted to grow non-layered crystals as well, e.g., perovskite crystal growth in between glass and polymer-covered substrate [72] and further with seed-printing strategy [73], and organic semiconductor in between overlapped SiO₂/Si substrates [74]. Namsrai et al. attempted to grow thin 1,5-DHAQ crystals in similar manners by recrystallizing from melt in space gap between two quartz plates [75], but the thickness and single-crystal diffraction data of the thin crystals was not presented.

Materials

Muscovite mica ($\text{KAl}_2[\text{AlSi}_3\text{O}_{10}](\text{OH})_2$) was used in this work for confining substrate. Mica is a layer-structured mineral group widely used for dielectrics. Muscovite mica is consisted of layers of negatively charged aluminosilicate, which are neutralized and weakly bound by potassium ions (Figure 3.3) [76]. Due to its chemically smooth surface, mica is a popular substrate for van der Waals epitaxial growth. Mica is directly applicable as a substrate for optoelectronics because it provides a transparent substrate in the visible and infrared range (Figure 3.2). Thus, direct optical measurements in transmission geometry of sufficiently thin crystals were possible through the *as grown* crystals on mica. Supersaturated solution was made by dissolving commercial powder form of 1,5-DHAQ (> 85% purity), 1,8-DHAQ (96%), and 1,4-DHAQ ($\geq 98.0\%$) from Sigma-Aldrich in organic solvents.

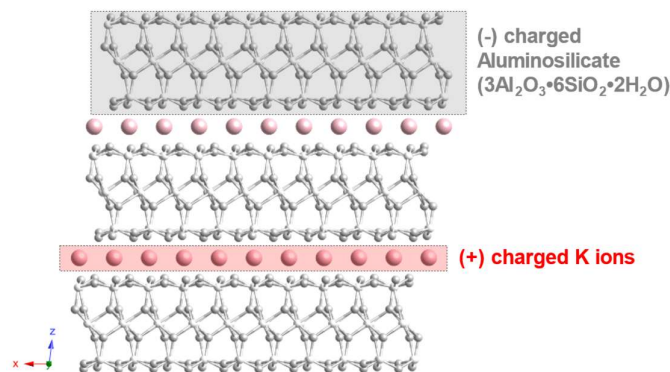


Figure 3.3. Crystal structure of muscovite mica. Projection along [010] direction.

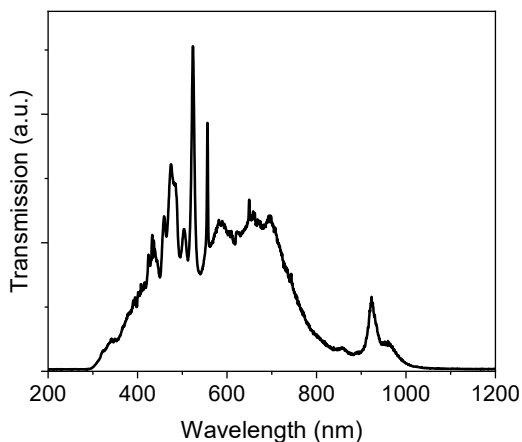


Figure 3.2. Transmission spectrum of a muscovite mica sheet measured at a home-built absorption setup. The white light source is generated by deuterium and halogen lamps. The detail of the setup is described in section 3.2.3.

Crystallization methods

To achieve the intended goals of the 2D confinement strategy, proper solvents, which gives flat shapes for the desired crystals should be chosen. This relationship depends on the interaction between solvent and solute; crystals grow in various shapes, i.e., needle, cube or plate in a solvent dependent manner [77]. By scanning several solvents, plate-shape preferred growth was found with 1,5-DHAQ in chloroform, 1,4-DHAQ in ethyl acetate and butyl acetate, and 1,8-DHAQ in acetone and acetonitrile. After finding appropriate solvents to grow flat shape crystals, V-1 grade 0.26 mm Muscovite mica was used in the crystallisation process to introduce the confined space. The scheme of the growth strategy is depicted in Figure 3.4. Mica is cut and cleaved into proper dimensions (edge length 10 to 15 mm and thickness around 0.2 mm) to be soaked in 20 ml vials. Mica sheets were heated at 105°C for 10 minutes on hot plate and rinsed with acetone to remove surface impurities. Two pieces of cleaned mica sheets were soaked in a 20 mL vial containing the saturated solution for crystallization. Details in growth conditions such as temperature, concentration, volume of solution, and annealing and cooling time is described in chapter 4. Briefly, the vials containing solute and solvent with lids closed were heated up to optimise the initial temperature to reach supersaturation. The annealing process, as well as initial concentration and initial volume of the solution, was optimized depending on the solutions to attain thin and large area crystals. After the annealing steps, the lids were replaced with aluminium foil with a pin hole made using a 0.8 mm needle. The vials were left in a stable place for a few days for the solvent to fully evaporate. DHAQ molecules were crystallised on the surface of mica sheets which was directly available for optical measurements. TEM specimens were prepared at the same time, by putting carbon film coated 200 mesh Cu grids on mica sheets in the supersaturated solutions. Small crystals having the same shape as those grown on mica sheet grew on the carbon film. This step is a simple expedient to get TEM specimens. However, for large area crystals a further strategy is needed. For instance, polymer-assisted dry transfer methods should be developed for UED experiments because the surface of carbon film on the mesh grid is not adequate for uniform, thin and large crystal growth.

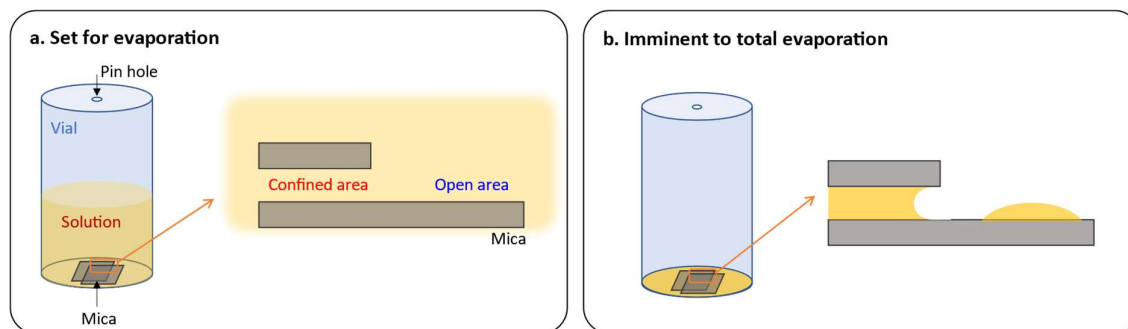


Figure 3.4. Scheme of the spatial confinement in supersaturated solution evaporation method. The contact angle between solution and mica differed by solvent, temperature, concentration, and impurities on the surface.

3.2 Characterisation methods

The crystals should be characterised before investigating their excited state behaviour using pump-probe experiments in terms of the dimension, crystal structure, and electronic structure. The dimensions of crystals are measured by optical microscope and atomic force microscope (AFM), and the crystal structures are determined by single crystal X-ray diffraction (SCXRD). Electron diffractograms were collected with a transmission electron microscope (TEM) to test the electron diffraction quality through the molecular crystals and analyse the crystallographic face of the surface. Steady state absorption spectra of the crystal and solution samples were recorded using a home-built spectrometer, to give information on excitation energies and calculation of the excitation fractions at the excitation.

3.2.1 Microscopic methods

The morphology of crystal growth was observed using an optical microscope (Olympus SZX10 with DP27 camera) and the images analysed by Stream Basic software. The thickness measurement and topography were achieved using an AFM, which is a probing method to collect information of surface structure and properties by scanning the target surface with a stylus probe. It measures the surface force normal to the surface as a function of the distance between the sharp probe tip on a flexible cantilever and the sample surface by monitoring the displacement of the cantilever. Vertical movement of the cantilever is controlled by a piezoelectric system. For thickness measurements of DHAQ crystals, a line crossing the edge of the crystals is traced with Bruker Stylus Profilometer Dektak XT in "Standard Scan" mode. For topographic images of the 1,5-DHAQ crystals on mica, a specific area on the surface of the crystals was scanned in intermittent contact mode with NanoWizard® 4 XP BioScience [78].

3.2.2 Diffraction methods

Diffraction patterns or spectra were used as a fingerprint of crystal structure to identify crystalline phase and the orientation of crystal faces. Here, single crystal X-ray diffraction is performed to determine the structures of the 1,5-, 1,8-, and 1,4-DHAQ crystals obtained by the different growth experiments. The electron diffraction patterns were recorded using a transmission electron microscope (TEM) and analysed to characterize the index of the surface of the thin crystals.

Single crystal X-ray diffraction

Cell dimensions of crystals are obtained by single crystal X-ray diffraction (SCXRD) at 100 K using Cu x-ray source. The obtained data are compared with existing data posted in Cambridge Structural Database (CSD). The measurement was carried out by Ms. Isabelle Nevoigt, and the result was discussed with Dr. Frank Hoffman.

Electron diffraction with TEM

The 1,5-, 1,8-, and 1,4-DHAQ crystals were tested using a TEM as preliminary experiments for UED. The zone axis was deduced from the selected area electron diffraction (SAED) pattern by comparing the d-spacing of Bragg spots and the degree between the spots with existing data. Also, the SAED pattern will be used as a reference for the UED experiments owing to the higher resolution of TEM relative to the electron sources used for ultrashort electron pulses.

Electron micrographs and diffraction patterns were taken with CryoTEM JEOL JEM-2100F operated by Dr. Robert Schubert and JEOL JEM 2100 TEM operated by Dr. Günther Kassier. The data were analysed using the software ImageJ and Gatan DigitalMicrograph. The crystal structure analysis was performed with the software VESTA.

3.2.3 Steady state absorption

Absorption measurements of solution and crystals have been performed on a home-built setup based on Kirchner's design [79] with four off-axis parabolic mirrors (OAP, Al, 90°, focal length = 10 cm). Light sources employed in the set-up are deuterium and halogen lamps (Ocean Optics, DH-2000-BAL), which provide white light in the range of 215 – 2500 nm (Figure 3.5). The white light is collimated when reflected at the first OAP, and the beam is focused on sample by the second OAP. The transmitted light is collected by a spectrometer (Avantes, AvaSpec-ULS2048-USB2-UA-50). To measure absorption spectra, crystal samples were fixed placed in a lens mount. The solution samples were contained in a 1 mm quartz cuvette. Absorption spectra are plotted as the logarithm of the transmitted light spectrum through the bare substrate or pure solvent as the reference relative to that transmitted through a crystal on substrate or solution sample.

The transition energies of the solution samples were analysed by finding peaks from the absorption spectra using first derivative methods for the main peaks and second derivative methods for the shoulder peaks. The optical bandgap of crystal samples were determined by fitting with Tauc plot [80]:

$$(\alpha h\nu)^{1/\gamma} = A(h\nu - E_g), \quad (3.11)$$

where h is Planck's constant, ν is frequency of photon, A is a constant, $\gamma = 2$ for indirect transition and α is absorption coefficient calculated from measured optical density by the formular [35]:

$$OD = \frac{\alpha l}{\log_e(10)} = 0.434\alpha l,$$

where l is length of a medium, or thickness of a sample.

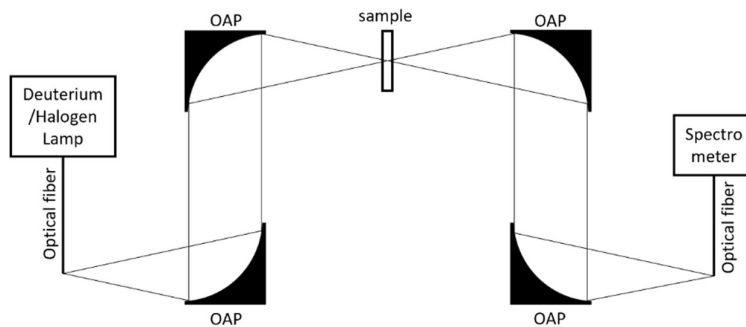


Figure 3.5. Schematic diagram of steady state absorption setup. OAP: Off-axis parabolic mirror.

3.3 Quantum chemical calculations

The excitation energies for solution and crystal samples were calculated with time-dependent density functional theory (TD-DFT) using the Gaussian 09 package [81] to support the steady-state absorption spectra. The coordinates of 8 molecules in a unit cell for the respective crystals are adopted from the CIF files, as the model for computing. The coordinates for the crystal models are listed in the Appendix, Table A 1 – 3. The geometries of crystal and solution models were optimized at B3LYP/6-31G level B3LYP/6-31G(d) level, respectively. The molecular orbital images were obtained by using the software Avogadro [82, 83].

In addition to obtaining insights on how the excited molecules are affected by the lattice, the strengths of excitonic couplings in the respective crystalline systems were estimated. First, the coordinates of three or four molecules which are neighbouring in a unit cell (In Appendix, Table A 4 – 6) are taken from CIF files posted in CSD that match the SCXRD measurements [84-86]. The vertical excitations of the respective molecules were calculated. The transition dipole moments of the first excitation (HOMO-LUMO) were extracted from the two output files of adjacent molecules and the excitonic coupling between the two dipole moments are calculated using the Fortran code created by Prof. Dr. Hong-Guang Duan.

3.4 Femtosecond transient absorption

One can observe the spectral change of an excited system in time with two ultrafast pulses: pump and probe beams. Pump beam at specific wavelengths excites the target system. After varied time delays, probe beams having a supercontinuum profile are spatially overlapped to determine the excited state spectra. When the excited system is irradiated by the probe beam, it absorbs photons to be promoted to the next energy levels (excited state absorption, ESA) or is stimulated to emit photons by transitioning to ground state (stimulated emission, SE). The change in absorption will also have contributions from photochemical processes and changes in absorption with the formation of different photoproducts. The differential absorption spectra, $\Delta A = A_{\text{Pump_on}} - A_{\text{Pump_off}}$, also called TA spectra, are collected at each time delay. The signals of ESA and SE appear in the spectra as positive and negative features, respectively. In addition, the reduced population of the ground state after pumping can be determined in the spectrum as negative ΔA signal in the wavelength region of ground state absorption, which is called ground state bleach (GSB). The differential absorption spectrum at a given time delay is the superposition of ESA, SE and GSB (Figure 3.6), and the integration of the spectra provides the time evolution of the excited system.

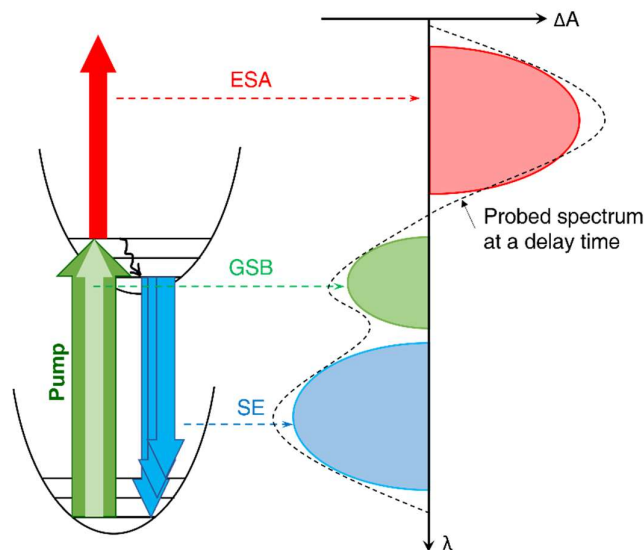


Figure 3.6. Diagram of transient absorption signals.

Experimental setup

Two different home-built TA setup were employed according to the respective systems' excitation energies. Figure 3.7 shows schematic diagram of the TA setup.

One setup used a Nd based commercial laser, PHAROS by Light conversion to generate pump beams with wavelengths 515 nm and 343 nm. The setup was constructed by Dr. Vandana Tiwari. The fundamental beam wavelength is 1030 nm with an output power of 1 W, temporal resolution of 190 fs, and repetition rate of 1 kHz. The fundamental beam (total input energy = 1 mJ) is divided to pump (80 %) and probe (20 %) beams at beam splitter (BS). The 20% fraction of the fundamental beam is guided to focus on 3 mm YAG crystal (SC in figure) by a convex lens (L1) to generate white light ranging from 500 to 850 nm to serve as the probe beam (Figure 3.7). The energy of the probe beam is controlled by neutral density filters (ND). A pin hole is placed to optimize spot size and power. The diameter of the probe beam is set to be 100 μm . The excitation fraction, 80% of the fundamental beam, is directed to a half-waveplate (HWP) to control the polarization. This beam passes through beta barium borate (BBO) crystal for Type I second-harmonic generation (SHG) to generate second harmonic pulses at 515 nm. To generate the 343 nm pump pulses, the 515 nm beam and residual 1030 nm beam are mixed with a BBO crystal type II SHG to go through third harmonic generation after passing through calcite crystal to match the two beams in a collinear geometry. Dielectric mirrors (DM) are placed in the beam paths to remove remaining fundamental and/or second harmonic beam. The pump beam is chopped using a Thorlabs chopper operating at 500 Hz, and the excitation photon fluence is controlled using a set of ND filters. The beam is focused on the sample by a convex lens with a diameter of 250 μm and 190 μm for 515 nm and 343 nm, respectively. Time delays between the pump and probe is controlled by a 150 mm linear motorized delay stage utilizing a retroreflector assembly from Newport. Crystal samples were fixed on a lens mount, and solution samples were contained in 1-mm quartz cuvette mounted on motorized shaker to keep sample fresh. Probe spectra for each time delay are detected with the combination of a spectrograph (9055, Scintec) and a charge-coupled device linear image sensor (CCD; S11156-2048-02, Hamamatsu Photonics).

Another setup uses a Ti:Sapphire laser (Coherent Legend Elite USP), of which the fundamental wavelength is 800 nm with a pulse duration of 40 fs, and a repetition rate of 1 kHz. The setup had been constructed by Drs. Gastón Corthey, Khalid Siddiqui and Simon Bittmann. The fundamental beam (total input energy = 500 μJ) is split into pump (80 %) and probe (20 %) beams. The probe beam (410 – 760 nm, Figure 3.7) in this setup is produced by passing through a 2 mm quartz cuvette filled with deionised water. The delay line in this setup has as scan range of 300 mm. The pump beam with a wavelength of 400 nm is generated by passing through a BBO crystal for Type I SHG. The pump energy is controlled using a variable neutral density filter. Residual 800 nm light in pump and probe beams is removed with

a short pass filter ($\lambda_{\text{cut-off}} = 700 \text{ nm}$). Solution samples were circulated through an in-line 0.5-mm quartz cuvette assisted by a miniature flow pump. The transmitted probe spectra are collected with a home-built spectrograph and a low-noise CCD (Hamamatsu, S11155-2048-01) equipped with fast electronics (Hamamatsu, C11165-01). The acquired data from both setups were analysed with a Python GUI script developed by Simon Bittmann [87].

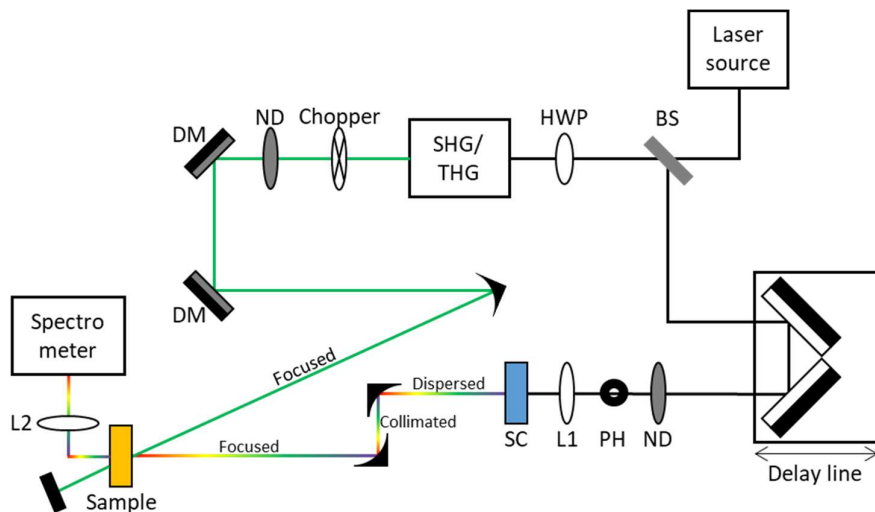


Figure 3.7. Schematic diagram of transient absorption setup.

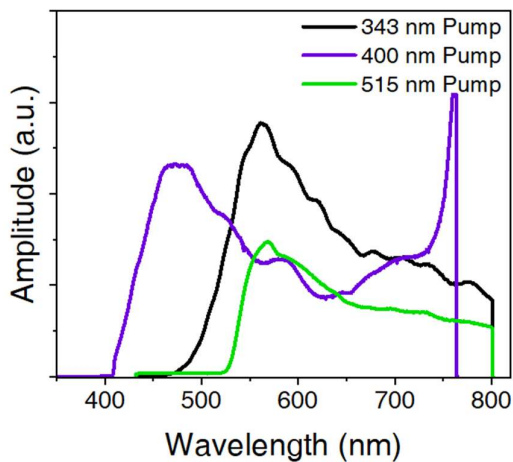


Figure 3.8. Spectra of the white light continuum used for probe in each measurement with different pump energies.

Sample preparation

Solution samples are prepared by dissolving solids in powder form into acetonitrile and filling the solution in a 1 mm quartz cuvette. For the measurement of crystals, as-grown crystals were used without any further treatment. Since the TA setup is not equipped with a sample monitoring system to focus the laser beams on smaller size than eye resolution, guiding lines with opaque tape were attached near the visibly large crystals (Figure 3.9). It should be noted that as-grown thin 1,8-DHAQ crystals did not give signal in a TA measurement as they were too thick to have sufficient light transmission. So, 1,8-DHAQ crystals were cut into 400 nm thin slices using ultramicrotomy. The penetration depth of 1,8-DHAQ crystal at the excitation wavelength (400 nm) is sub-micron in length. The penetration depths of crystal samples were calculated with measured absorbance and thickness.

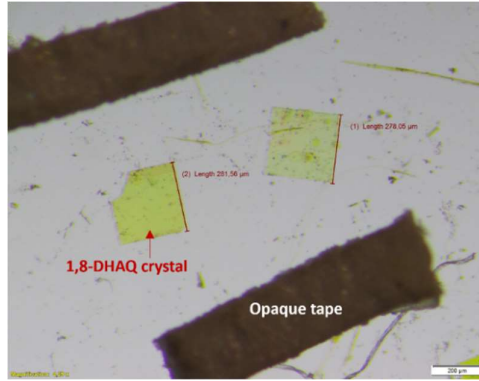


Figure 3.9. Guiding line for the sample position with opaque tape attached near the crystals to help located the crystal positions.

Penetration depth

Penetration depth (δ) means the distance where the flux density drops by a factor of e^{-1} after the propagation of a light through a medium. The attenuation of the light is expressed as [88]:

$$I(l) = I_0 e^{-\alpha l}, \quad (3.12)$$

where I_0 is the initial intensity of light, $I(l)$ is the intensity after transmission in distance of l , and α is attenuation coefficient. Then the penetration depth is given as $\delta = 1/\alpha$. The absorption spectra are recorded in terms of the absorbance or optical density (OD), which is dependent on the length of the absorbing medium and defined as:

$$OD = -\log_{10} \frac{I(l)}{I_0}. \quad (3.13)$$

The attenuation coefficient α can be calculated when the thickness of the crystal and absorbance is given by substituting the equation (3.2):

$$OD = \frac{\alpha l}{\log_e 10} = 0.434 \alpha l. \quad (3.14)$$

Excitation fractions

To estimate the fraction of molecules excited with a given photon pump flux, the absorption cross-section σ was calculated by the relation:

$$\sigma = \frac{\alpha}{N}, \quad (3.15)$$

where N is the number of molecules in unit volume given by

$$N = \frac{\rho N_A}{M}. \quad (3.16)$$

ρ is density of the crystal, N_A is Avogadro's number, and M is molar mass of the molecule. The absorption cross section, σ , of the solution sample can be calculated in a similar way by the relation:

$$\sigma = \frac{\epsilon}{N_A}, \quad (3.17)$$

where ϵ is molar absorption coefficient from Beer-Lambert's Law [89]:

$$I(l) = I_0 10^{-\epsilon c l}. \quad (3.18)$$

c is the concentration of the solution sample. This gives the relation:

$$OD = \epsilon c l. \quad (3.19)$$

The excitation fraction is given by multiplying the absorption cross-section and photon flux of the pump beam. Photon flux is calculated by dividing the number of photons:

$$\text{Photon flux} = \frac{\text{number of photons}}{\text{spot area}} = \frac{\text{energy per pulse}/(hc/\lambda)}{\text{spot area}}. \quad (3.20)$$

The energy per pulse was obtained by measuring the power of the pump beam using a calibrated power meter and the diameter of the beam spot (full width half maxima, FWHM) was calculated by reading the intensity of the pump beam passed through an aperture with known size. For Gaussian beam, the intensity profile of the beam along the radius r is written as:

$$I = I_0 e^{-2r^2/w^2}, \quad (3.21)$$

where I_0 is the intensity at the centre and w is $1/e^2$ width. Then the power of the transmitted beam through an aperture with radius a is:

$$T = 1 - e^{-2a^2/w^2}. \quad (3.22)$$

w is obtained by measuring the power with a power meter, and FWHM can be calculated by the relationship:

$$FWHM = \sqrt{2 \ln 2} w. \quad (3.23)$$

According to the measured data and calculations, the specifications of the samples are listed in Table 3.1 and Table 3.2 and excitation fractions of each samples at each photon fluences are listed in Table 3.3. The thicknesses of crystals on mica were measured using AFM.

Table 3.1. Specifications of 1,5-, 1,8-, and 1,4-DHAQ crystal samples for the TA measurements.

	Absorbance (OD)	Thickness (μm)	Penetration depth (μm)	Density ($\text{g}\cdot\text{cm}^{-3}$)	Absorption cross-section (cm^2)
1,5-DHAQ	0.84 at 343 nm	3.88 – 8.00	2.00 – 4.13	1.59	$6.07\cdot 10^{-19}$ – $1.25\cdot 10^{-18}$
1,8-DHAQ	0.38 at 400 nm	0.4	0.46	1.54	$5.66\cdot 10^{-18}$
1,4-DHAQ	0.50 at 515 nm	1.5	1.30	1.58	$1.94\cdot 10^{-18}$

Table 3.2. Specifications of 1,5-, 1,8-, and 1,4-DHAQ solution samples measured TA.

	Absorbance (OD)	Concentration ($\text{mol}\cdot\text{cm}^{-3}$)	Absorption cross-section (cm^2)
1,5-DHAQ	0.078 at 343 nm	$7.96\cdot 10^{-8}$	$1.63\cdot 10^{-16}$
1,8-DHAQ	0.97 at 400 nm	$1.98\cdot 10^{-7}$	$8.12\cdot 10^{-17}$
1,4-DHAQ	0.43 at 515 nm	$1.22\cdot 10^{-7}$	$5.88\cdot 10^{-17}$

Table 3.3. Calculated excitation fractions of 1,5-, 1,8-, 1,4-DHAQ crystal and solution sample at each photon fluences.

	1,5-DHAQ		1,8-DHAQ		1,4-DHAQ	
	Fluence ($\text{mJ}\cdot\text{cm}^{-2}$)	Excitation fraction (%)	Fluence ($\text{mJ}\cdot\text{cm}^{-2}$)	Excitation fraction (%)	Fluence ($\text{mJ}\cdot\text{cm}^{-2}$)	Excitation fraction (%)
Crystal	1.13	0.05 – 0.11	0.75	0.47	0.24	0.05
	2.71	0.12 – 0.25	1	0.62	0.44	0.10
	3.14	0.14 – 0.29	2	1.24	1.60	0.35
Solution	2.08	5.88	1	16.35	0.035	0.53
	2.71	7.68	2	32.70	0.29	4.35
	3.14	8.88	3	49.05	0.44	6.64

Chapter 4. Thin Crystal Growth and Characterization

As described in the section 3.1 in Chapter 3, transient absorption measurement requires a solid sample to be thin enough to pass the pump and probe beams and larger than the beam sizes. To study the photo-induced reaction influenced by the lattice, the solid sample must be crystalline. Many crystals are typically needed and the density of crystals on a substrate should be low to avoid overlapping of crystals. One independent single crystal in a beam spot is desired. Also, if the crystals grow on a substrate which is transparent to the pump and probe beams, the sample preparation task will be reduced due to the omitted crystal transfer step. To meet these requirements for transmission-based experiments, I have designed a method to grow thin and large crystal on visible-transparent substrates, so that the as-grown crystals on the substrate can be directly measured. In this chapter the strategy is introduced, and the dimension of the crystals and their crystallographic characters are measured.

4.1 Morphology

As reviewed in the section 3.1 in Chapter 3, the nucleation density is influenced by thermodynamic factors. The shape of crystals for example, needle, cube, or plate, is determined by the kinetics of crystal growth, i.e., the growth rates of the different crystallographic faces [68]. The impacting factors on the growth kinetics are solvent-solute interactions, supersaturation, temperature, evaporation rate in the case of solvent drying method, quenching rate, and so on. The crystal morphology differed by those factors, which can be predicted by theoretical modelling [77], but the calculation methods needed to provide this optimisation are beyond this project, so the optimised parameters were experimentally determined. In this work, the nucleation density and the crystal shape are optimised to have isolated thin and large crystals by adjusting the crystallisation conditions and applying 2D spatial confinement to the crystallisation environment to maximise the 2D anisotropic growth.

4.1.1 Control over nucleation and growth

Solvents

First, to find suitable solvents in which 1,4- and 1,5-DHAQ crystals grow to flat shapes, several solvents which are known to dissolve them were tested: toluene, ethyl acetate, isopropyl alcohol, butyl acetate, acetone, acetonitrile, ethanol, and chloroform. For the 1,8-DHAQ sample, it was not necessary to test many solvents since it has been reported to grow in flat square shape from slow evaporation of solution in toluene, n-butanol, acetone, and acetonitrile [86]. Initial temperatures for each solvent were set slightly above the boiling point of the solvent to develop supersaturation. As a result, 1,4-DHAQ is found to preferably grow in plate shape in ethyl acetate and flat-shaped crystals of 1,5-DHAQ grew in chloroform. Figure 4.1 shows the crystal shapes of the two molecules to compare the morphology dependence on the solvents.

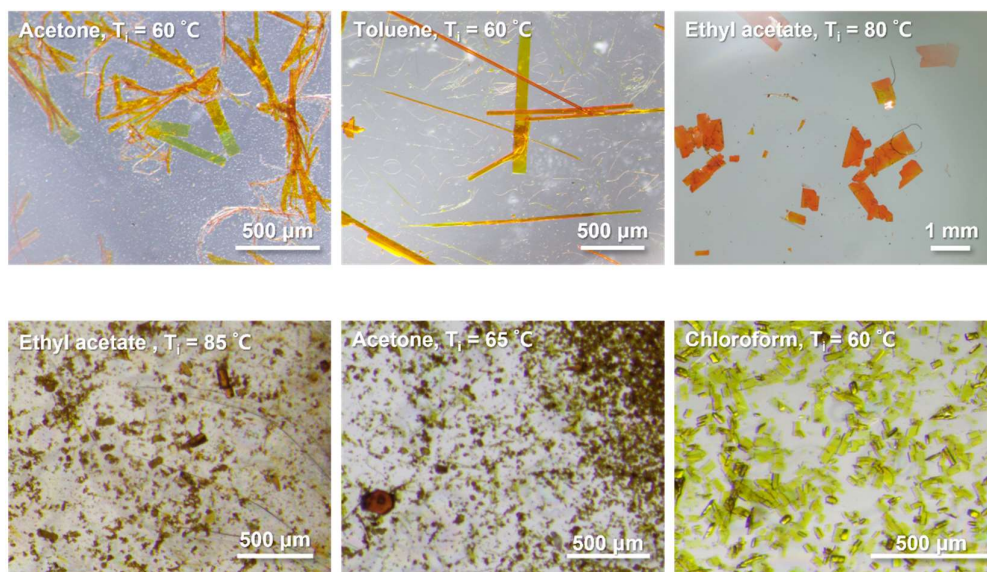


Figure 4.1. Optical images of 1,4-DHAQ (upper row) and 1,5-DHAQ (lower row) crystallization with different solvents.

Spatial confinement

After finding adequate solvents, overlapped mica sheets were applied to introduce 2D spatial confinement. Figure 4.2 shows how overlapping mica substrates give differences in crystallisation after evaporating DHAQ solutions. The crystal densities are markedly different in open and confined area. The confined area refers to the part of the mica sheet covered by another mica sheet. For a quantitative comparison, the number of crystals in open and confined areas marked with blue and red rectangles in Figure 4.2(a) are counted: 34 crystals in confined region whereas 296 crystals in open region. In addition, the probability to find thin and isolated crystals, i.e., not aggregated with adjacent crystals, is higher in confined area. The chunky crystals found in exposed areas represent the known crystal habit of the molecules. For instance, 1,5-DHAQ is known to grow in prism shape with (100) and (102) faces [75]. Among polymorphs of 1,8-DHAQ crystal, polymorph 1 which has (001) plate habit [85] is obtained in this experiment. F1 polymorph of 1,4-DHAQ crystal is thermodynamically predicted to favour plate formation having (002) and (101) faces, but the shape is highly affected by kinetic factors [86]. Detailed crystallographic characterization is discussed in section 4.2.

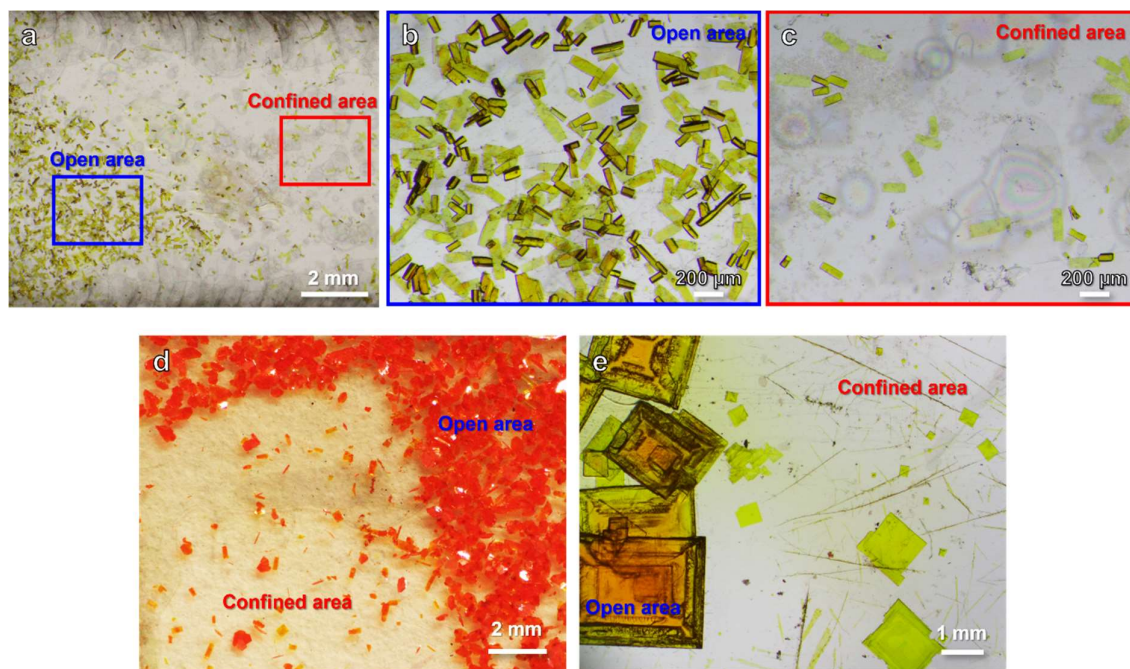


Figure 4.2. Morphology of DHAQ crystals grew on muscovite mica substrate. (a) Optical image of 1,5-DHAQ crystallised on mica. (b) Enlarged images in open area and (c) in confined area in (a). (d) 1,4-DHAQ and (e) 1,8-DHAQ crystals on mica.

Additional optimisations

To avoid interference between crystals, nucleation density should not be too high. The driving force of the nucleation step is supersaturation which depends on concentration and temperature as described in chapter 3, equation 3.1 and 3.2. Therefore, the initial concentration and temperature are optimized for moderate nucleation density. Initial concentration indicates the total amount of solute per unit volume of solvent, regardless of the solute fully dissolved or not. Figure 4.3 and Figure 4.4 shows the morphology of 1,5-DHAQ crystal growth from the solution in chloroform depending on the initial concentration (C_i) and initial temperature (T_i) in open and confined area, respectively. The 8 mM solution was heated to 60 °C, which produced isolated planar crystals in the confined area. When the solution is heated to 65 and 70 °C, needle-shaped crystals are more produced.

Since the solvent's evaporation dynamics and cooling rate also impact on crystal growth kinetics, the initial volume (V_i) and annealing process was additionally optimized for more frequency in finding flat and large crystals. Figure 4.5 shows variation of the initial volume from 1 mL to 4 mL. Evaporation of a 2 mL solution resulted large (lateral length 100 – 300 μm) planar crystals. The variation of annealing process was tested with 2 mL of 8 mM 1,5-DHAQ solutions in chloroform (Figure 4.6). The cooling rate is controlled by sequences of putting the vials containing the solution, which are closed with its plastic lids, on a temperature-set hot plate and off the hot plate at room temperature (RT). Four sequences are applied: (a) 60 °C (10 min.) – RT (10 min.), (b) 60 °C (10 min.) – 40 °C (10 min.) – RT (10 min.), (c) 60 °C (20 min.) – 40 °C (20 min.) – RT (10 min.), and (d) 60 °C (10 min.) – 50 °C (10 min.) – 40 °C (10 min.) – 30 °C (10 min.) – RT (10 min.). After the annealing courses, the plastic lid of the vial is replaced with aluminium foil with one pin hole made by 0.8 mm needle to diffuse evaporated solvent out of the vial. The vial was left in a stable place for a few days for the solvent to be fully evaporated. Figure 4.6 shows that the sequence (b) produces the greatest number of thin and large crystals.

The conditions for 1,4-DHAQ and 1,8-DHAQ are optimized in a similar way as done for 1,5-DHAQ crystallization. The initial conditions for 1,4-DHAQ are adjusted as: $C_i = 1.4$ mM, $V_i = 4.5$ ml, and $T_i = 80$ °C and annealing process is optimized as: 80 °C (10 min.) – RT (5 min.) – 60 °C (10 min.) – RT (10 min.). The initial conditions for 1,8-DHAQ are adjusted as: $C_i = 16.7$ mM, $V_i = 2$ ml, and $T_i = 60$ °C and 1,8-DHAQ crystals are large enough without the annealing treatment.

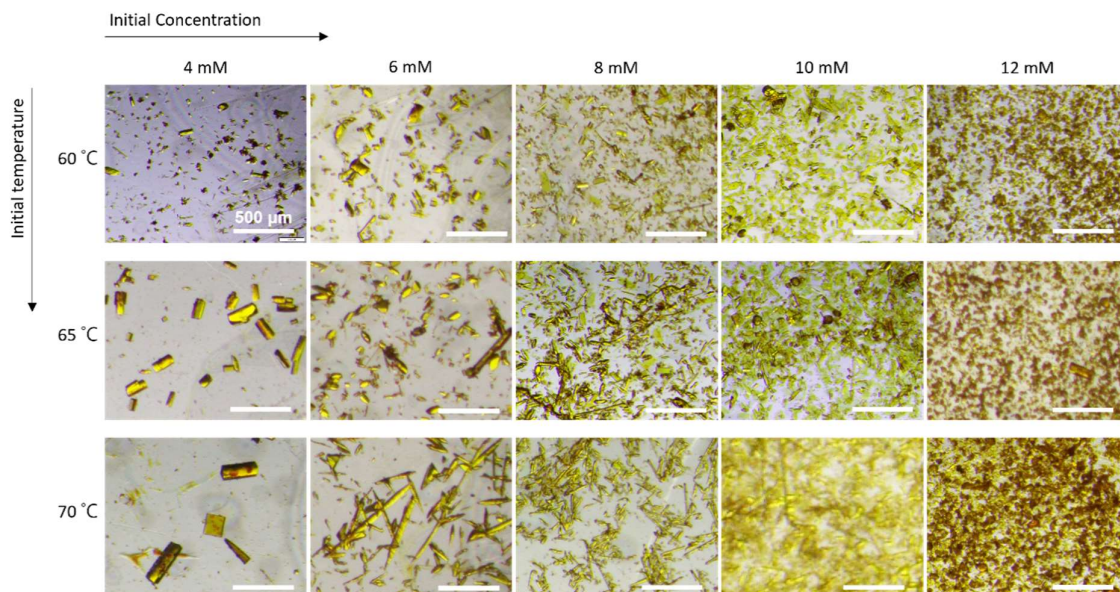


Figure 4.3. Crystal morphology of 1,5-DHAQ in open area by variation of initial concentration and initial temperature. Initial volumes were all set to be 2 ml. Scale bar is 500 μm for all panels.

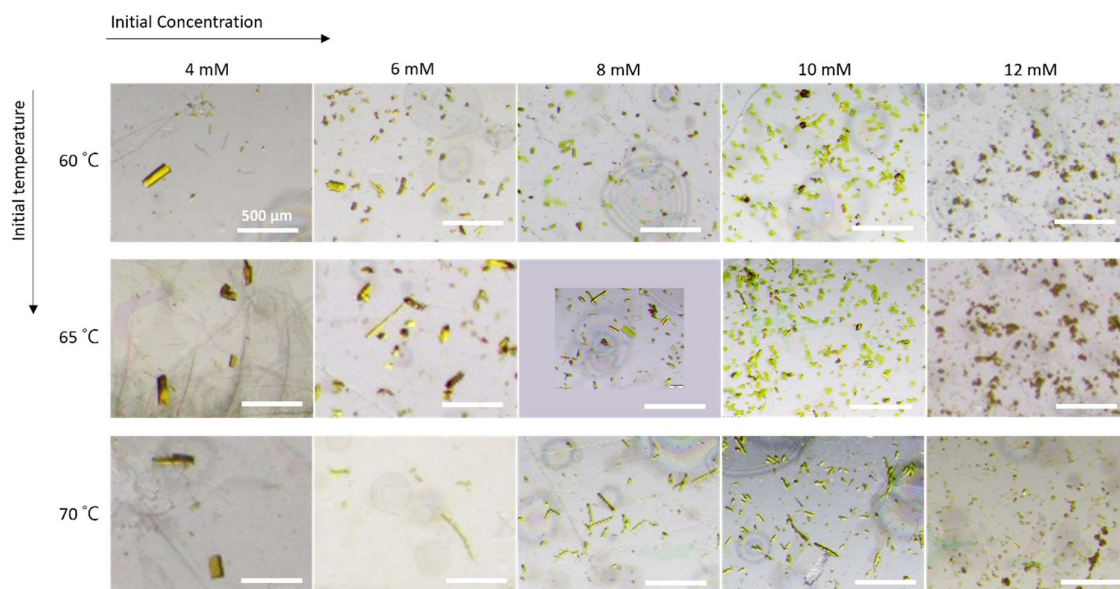


Figure 4.4. Crystal morphology of 1,5-DHAQ in confined area by variation of initial concentration and initial temperature. Scale bar is 500 μm for all panels.

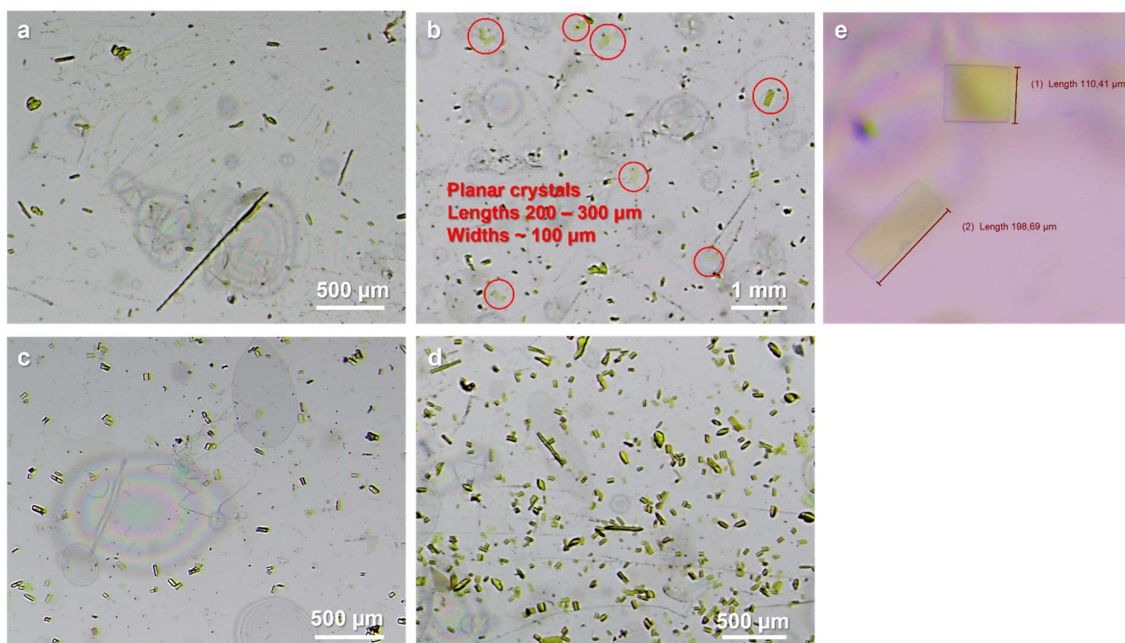


Figure 4.5. Morphology of 1,5-DHAQ crystals in confined area depending on initial volume (V_i). The initial concentration is set to 8 mM. (a) $V_i = 1$ mL. (b) $V_i = 2$ mL. (c) $V_i = 3$ mL. (d) $V_i = 4$ mL. (e) Enlarged optical image of two crystals on the substrate of (b).

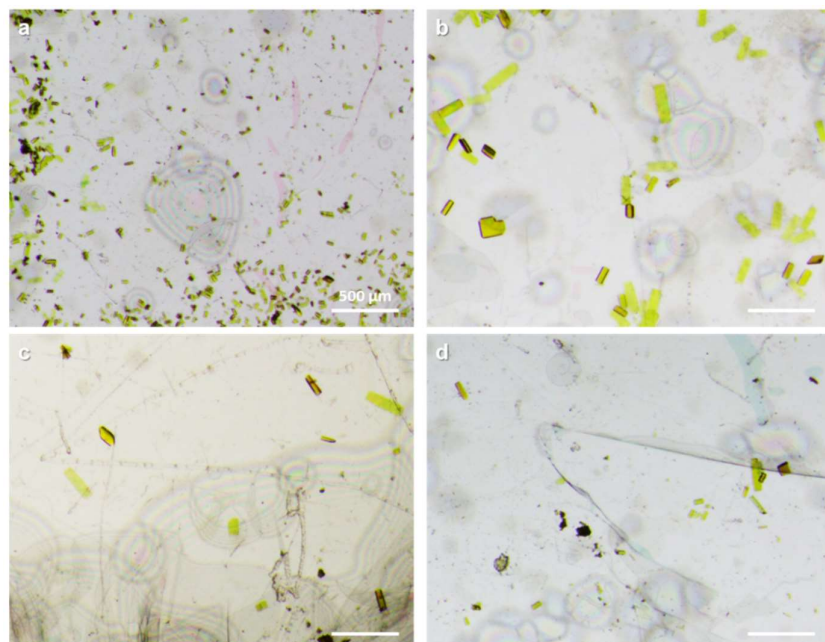


Figure 4.6. Crystal growth morphology of 1,5-DHAQ after different temperature treatments. (a) 60 °C | 10 min - RT | 10 min - Evaporation. (b) 60 °C | 10 min - 40 °C | 10 min - RT | 10 min - Evaporation. (c) 60 °C | 20 min - 40 °C | 20 min - RT | 10 min - Evaporation. (d) 60 °C | 10 min - 50 °C | 10 min - 40 °C | 10 min - 30 °C | 10 min - RT | 10 min - Evaporation.

4.1.2 Thickness measurement

Several 1,5-DHAQ thin crystals grown on confined area of mica sheet are investigated with AFM. Figure 4.7 shows eight crystals observed on a sheet. The thicknesses of thin crystals are in the range of 1.0 – 1.75 μm . By scanning a corner of a crystal, the stacked layers on the crystal surface are visualized by the error signal (deviation) image (Figure 4.8). Note that despite many thin crystals, which are larger than the beam size, were found much larger crystals on the substrate, which are resolvable by eyes. These were chosen for the TA measurement to focus laser beams on target crystal with simple alignment by eye. The thicknesses of TA-measured crystals are described in

Table 3.1 in chapter 3.

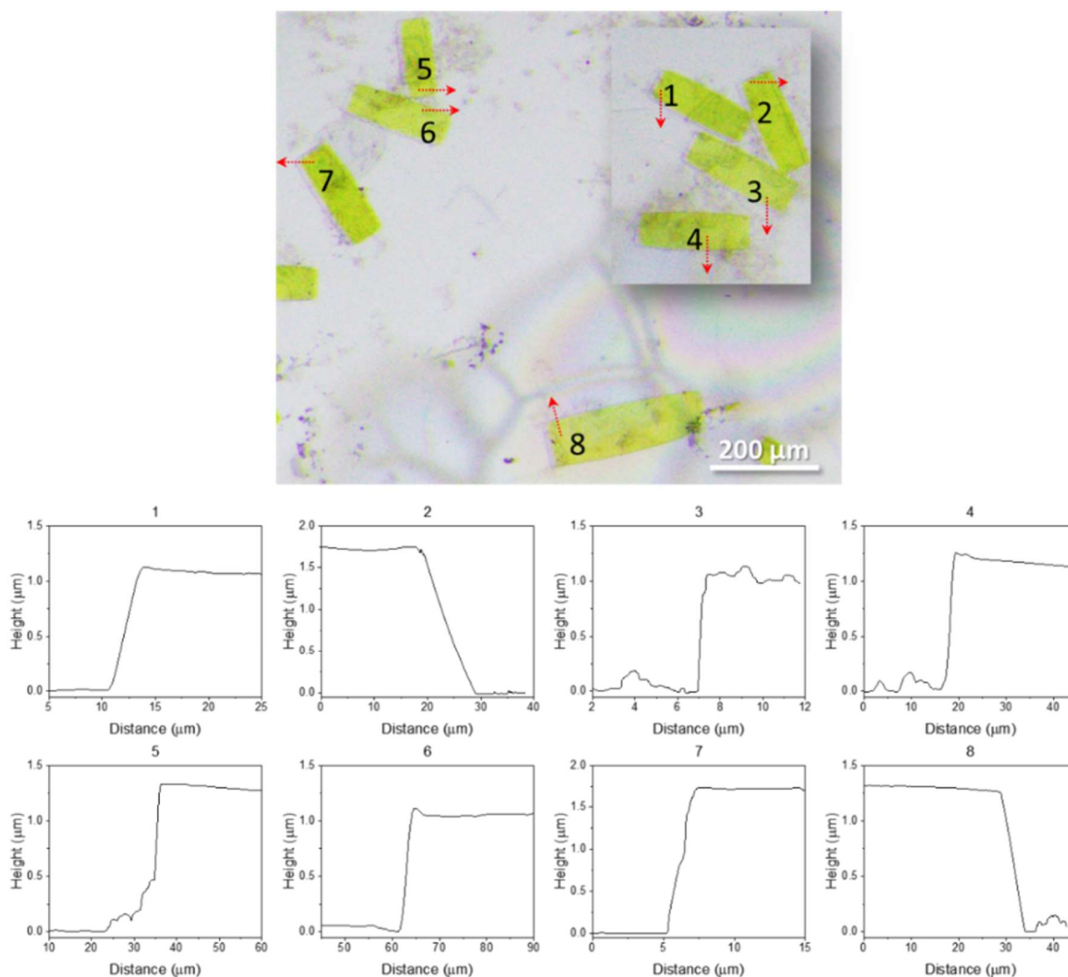


Figure 4.7. Height profiles at the edges of each crystal by AFM. Red arrows represent scanning direction.

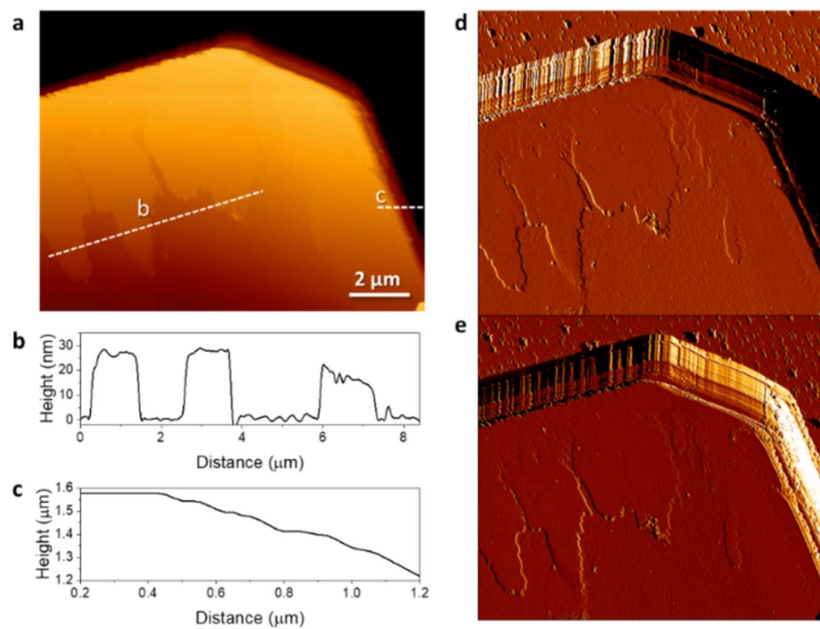


Figure 4.8. Topography of 1,5-DHAQ thin crystal. (a) AFM height image. (b, c) Height profile. Each profile is traced along the dashed lines shown in (a), respectively. The background height of the surface is subtracted in profile (b). (d, e) Error signal image of trace and retrace, respectively.

4.1.3 Effect of spatial confinement

The main difference of growth morphology in the confined and open areas of mica was the crystal density and shape. Recall the rate of nucleation J discussed in section 3.1 with equation 3.8:

$$J = A \exp \left[-\frac{16\pi\gamma^3 v^2}{3k^3 T^3 (\ln S)^2} \right].$$

Evaporation of solvent in the confined area is slower than in the open areas, as Berli et al. showed with sessile and confined water droplets [90], which induces slower increase of S . At a certain time during evaporation leading to the nucleation step, the supersaturation is lower in the confined space than in the open space; it means that the nucleation barrier is higher in the confined area than in open areas at the same time. Consequently, the crystal growth step proceeds with a smaller number of nuclei. After nucleation, the nuclei go through a growth step, which is a kinetic process governed by transport of solute particles, surface diffusion, and equilibrium between adsorption and desorption. The motion of solute particles in a 2D-confined volume of solution during evaporation is supposed to be modified from those in free volume. The modified growth kinetics in the confined area was discussed for graphene growth by chemical vapor deposition (CVD) [91]. The growth kinetics for gas phase processes, involve deposition rates mainly governed by mass transport (diffusion) or surface reaction (edge-attachment). Since the mass transport coefficient increase with the increase of the reactant's flow velocity [92], suppressing the flow by confining the reaction space leads the growth kinetics to be dominated by the edge-attachment process and this mechanism results in large area crystal growth. In analogy of diffusion, reduced evaporation rate in the confined space is designed to give a similar effect of suppression of reactant's flow rate in confined spaces used for CVD system.

4.2 Crystallographic Characterization

The crystal structures were determined by XRD for understanding supramolecular interactions in the lattice structure. The visualised crystal structures from the Crystallographic Information File (CIF) files show how the molecules are linked and stacked in the lattice. The coordinates of atoms in the lattice are used for the time-dependent density functional theory (TD-DFT) calculations of electronic structure and excitonic couplings in the next chapter. In addition, steady state electron diffraction patterns were recorded by TEM to provide preliminary information for UED experiments planned in the future.

4.2.1 Single crystal X-ray diffraction

For determination of the crystals' structures among their polymorphs, single crystal X-ray diffraction (SCXRD) was performed. The cell dimension of 1,4-DHAQ matched with the identifier DHXANT12 [86] in the Cambridge Structural Database (CSD). The cell dimension of 1,5-DHAQ and 1,8-DHAQ crystals matches with DHANTQ02 [84] and DHANQU08 [85], respectively. The crystallographic data is sorted in Table 4.1. With those data, the crystal structures can be drawn as shown in Figure 4.9. The upper row of Figure 4.8 represents how those molecular layers are stacked by π - π interaction, of which distance is about 3 Å in all three structures. And the π -stacked layers are arranged along the c axis in alternative orientation. The last row of Figure 4.9 shows two laterally neighbouring molecules forming a layer in the lattice structure. Those molecules of 1,4- and 1,5-DHAQ are linked by intermolecular hydrogen bonds, whereas those of 1,8-DHAQ are not. The hydrogen bond lengths are listed in Table 4.2. The intermolecular hydrogen bonds in 1,5-DHAQ crystal are coupled with the intramolecular hydrogen bonds which is involved in ESIPT process. As reviewed in section 2.2.2, OH groups at the 1 and 4 positions in anthraquinone stabilise the $\pi\pi^*$ state, so that the excited state relaxation is not dominated by the ESIPT reaction. The distortion in intramolecular hydrogen bonds and the addition of intermolecular hydrogen bonds are presumed to perturb the atomic motions at excited states.

Table 4.1. Crystallographic data in CSD of 1,4-, 1,5-, and 1,8-DHAQ which matched with the crystals obtained from this work.

	1,4-DHAQ	1,5-DHAQ	1,8-DHAQ
Crystal system	Monoclinic	Monoclinic	Tetragonal
Space group (point group)	P2 ₁ /c (2m)	P2 ₁ /c (2m)	P4 ₁ (4)
a (Å)	10.2390(8)	6.0092(5)	5.7165(9)
b (Å)	6.0429(4)	5.3074(2)	5.7195(9)
c (Å)	16.454(2)	15.7538(6)	30.801(5)
α (deg)	90	90	90
β (deg)	95.999(8)	93.672(5)	90
γ (deg)	90	90	90

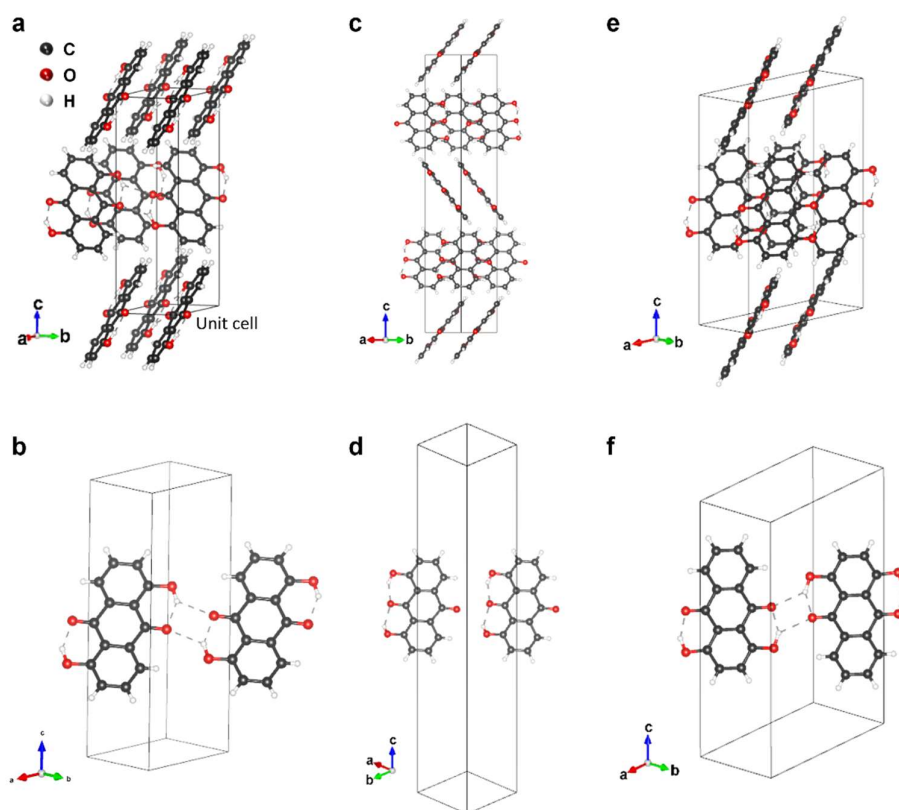


Figure 4.9. Crystal structure of 1,5- (a, b), 1,8- (c, d), and 1,4-DHAQ (e, f). Upper row: DHAQ molecules packed in a unit cell. Last row: Two DHAQ molecules forming intermolecular hydrogen bond (except for 1,8-DHAQ) in a unit cell. Dashed lines indicate hydrogen bonds.

Table 4.2. Hydrogen bond (HB) lengths between the oxygen of C=O and the hydrogen of O-H. The distance is measured with Gaussian output files in the software Avogadro for solution phases and with CIF files in the software Vesta for crystal structures. Units are in Å.

Molecule		Intramolecular HB	Intermolecular HB
1,5-DHAQ	Solution	2.234	
	Crystal	1.796	2.30
1,8-DHAQ	Solution	2.225	
	Crystal	1.825, 1.922	
1,4-DHAQ	Solution	2.216	
	Crystal	1.703	2.29

4.2.2 Transmission Electron Microscopy

The diffraction quality of the crystals was determined using a TEM to obtain essential background electron diffraction patterns for the planned UED experiments. The as-grown crystals on mica are measurable with the optical measurement setups, but the crystals have to be transferred to TEM grids to load into electron diffraction instruments. Therefore, crystal transfer methods such as polymer assisted dry transfer, agitation or sonification in water and fishing, etc. should be developed to use the thin crystals that strongly stick to substrates for UED experiments. In this work, growing crystals directly on TEM grid was tried instead of developing the transfer methods, which is left for the next step. Carbon film coated TEM grids were put on a mica sheet in the batch of crystallization runs to prepare samples for TEM. Small crystals having the same shape as those on mica sheet grew on the carbon film of the TEM grid. This strategy was successful with only 1,5-DHAQ to find electron-diffracting crystal. The 1,4- and 1,8-DHAQ samples for TEM had to be prepared by sectioning larger crystals using ultramicrotomy. Sampling without microtomy is desirable in fs experiments because the surface of the crystal can be contaminated or roughened while being sliced which can cause unnecessary scattering. Again, tailored crystal transfer methods for the thin organic crystals must be developed for this reason.

From the selective area electron diffraction (SAED) pattern (Figure 4.10a-c), the zone axes of the surfaces are determined by comparing the d-spacings of Bragg spots and reference data confirmed by SCXRD measurements. The faces of side facets of crystals are annotated on the corresponding Bragg spots in the SAED patterns. According to the crystal face information analysed, the crystal shapes are drawn in Figure 4.10d-f. The distances of each surface from the origin are adjusted to show the fragments of molecules for convenience. These results will be used as reference data for UED in the future.

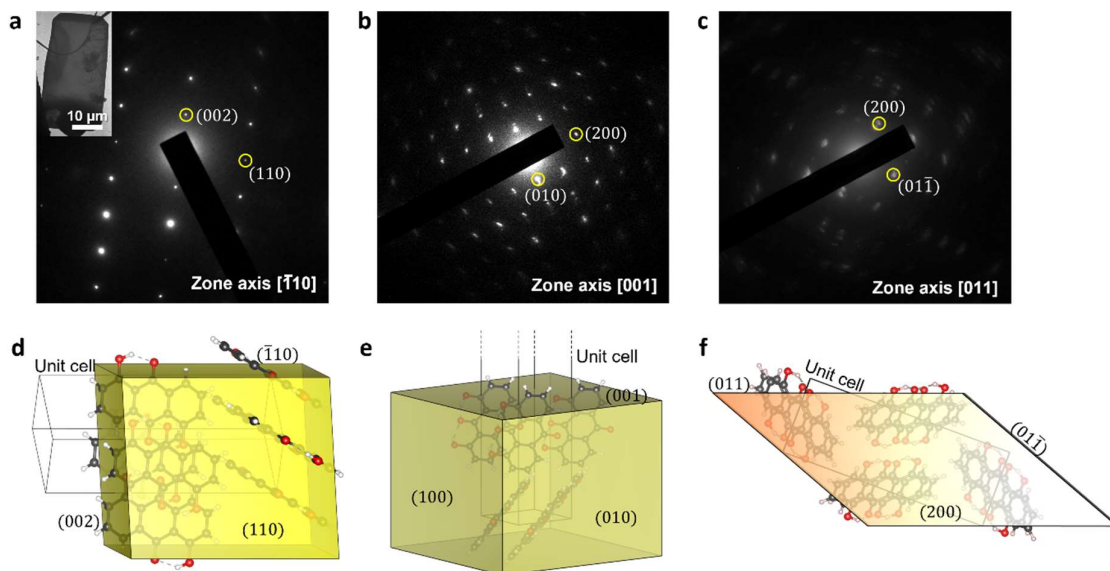


Figure 4.10. Surface orientation determination by electron diffraction patterns obtained with TEM. (a-c) Electron diffraction patterns of 1,5-, 1,8-, and 1,4- DHAQ, respectively. Inset in (a): Bright field image of 1,5-DHAQ crystal grown on the TEM grid. (d-e) Illustration of crystal shapes corresponding to (a-c). The flat surfaces of crystals (zone axis in TEM) are oriented to the top in the illustrations.

Chapter 5. Steady-State Absorption Measurements and Quantum Chemical Calculations

In the previous chapter, the morphology and crystallographic information were investigated on the thin crystals of 1,5-, 1,8-, and 1,4-DHAQ obtained by crystallisation from solution in 2D confined space. The crystallographic analysis reveals that the intermolecular hydrogen bonds are formed in 1,5- and 1,4-DHAQ crystals. The crystal structure provides insight into the geometric relationship between molecules in the lattice. The stiff arrangement in the lattice possibly influences on the electronic structure of the system, as mentioned in chapter 2. In this chapter, steady-state absorption measurements on crystals and solutions of the respective molecular systems are conducted to investigate the difference in the electronic structure. The absorption spectra present resonant excitation energies for each system for pump-probe measurements. The measured optical density is used to calculate penetration lengths and excitation fractions listed in chapter 3. Quantum chemical calculations on the three derivatives in solution and crystal support the occurrence of more absorption bands in crystals with narrowed energy gaps and delocalised molecular orbitals. Also, the coupling of transition dipole moments in lattice is computed to examine the excitonic coupling and spatial extent of the excitation and how this might affect the proton transfer process.

5.1 Steady-state absorption spectra

The lines in the left and middle columns of Figure 5.1 are the steady-state absorption spectra of 1,5-, 1,8-, and 1,4-DHAQ solutions in acetonitrile and crystals. The absorption peaks of solution samples analysed by first and second derivative methods are listed in Table 5.1 compared with previous reports in the literature, which were measured in different solvents. The absorption bands of crystals are broader than those of solutions because the higher energy levels in crystals are shifted to lower energy and have narrower linewidths. The narrowed gaps between electronic levels are described below with the theoretical results. Due to the broadness or more correctly more underlying structure of the absorption bands in the single crystals, only the absorption edges of crystal samples are analysed by Tauc plot fitting. The details were described in chapter 3. The fitting plots are given in the right column of Figure 5.1 and the analysed absorption edges of crystals compared with reported data at low temperature are listed in Table 5.2. The optical bandgaps of crystals are calculated to be 2.51 eV for 1,5-DHAQ, 2.47 eV for 1,8-DHAQ, and 2.14 eV for 1,4-DHAQ. Those energies are converted to wavelength scale in Table 5.2. The absorption edges observed here agree with the literature. Based on the absorption spectra, the pump wavelengths for each molecular systems are selected: 343 nm for 1,5-DHAQ, 400 nm for 1,8-DHAQ, and 515 nm for 1,4-DHAQ.

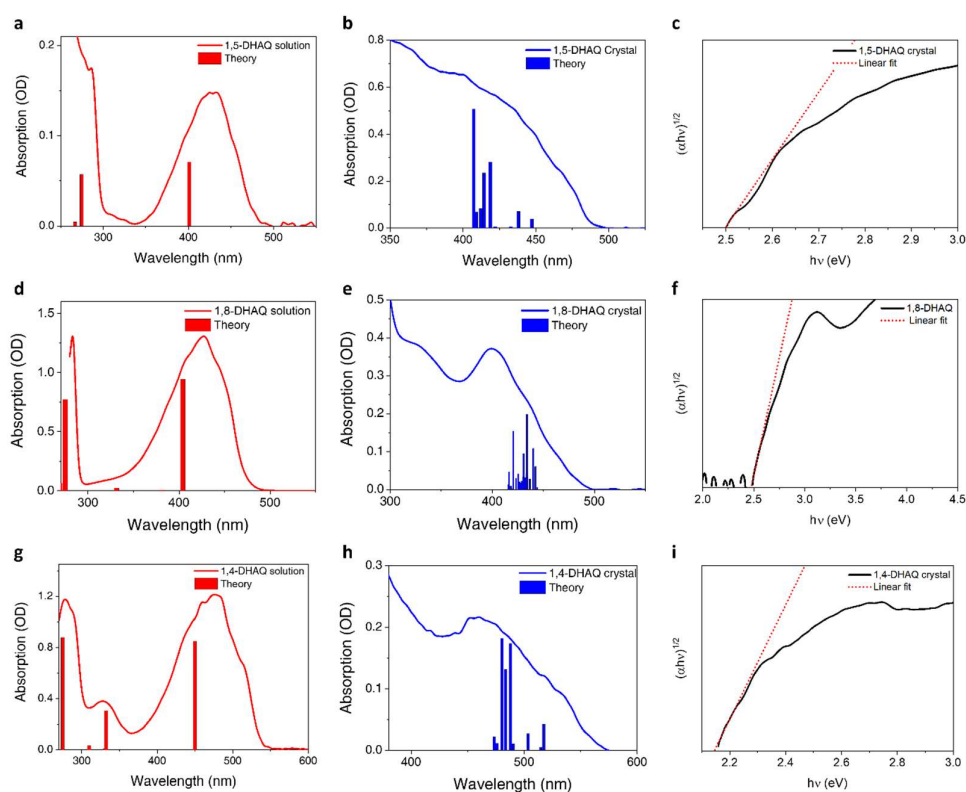


Figure 5.1. Steady state absorption spectra of 1,5-, 1,8-, and 1,4-dihydroxyanthraquinone solution and crystal. Left column: spectra of solutions. Middle column: spectra of crystals. Right column: Tauc plot of crystals and linear fit.

Table 5.1. Absorption peaks analysed from the absorption spectra of 1,5-, 1,8- and 1,4-DHAQ solutions in acetonitrile and the first absorption peaks of the solutions in different solvents from the literature. The values are expressed as wavelength (nm).

Molecule	Local Maxima	1 st peak	Literature
1,5-DHAQ	430	457	484 in n-heptane [58]
1,8-DHAQ	427	456	458 in CCl ₄ [93]
1,4-DHAQ	476	516	521 in CCl ₄ [93]

Table 5.2. Absorption edges analysed from the absorption spectra of 1,5-, 1,8- and 1,4-DHAQ crystals, the absorption edge of 1,5-DHAQ crystal at low temperature from the literature, and the first absorption peaks of 1,8- and 1,4- DHAQ solid powder at low temperature from the literature. The values are expressed as wavelength (nm).

Molecule	Absorption Edge	Literature
1,5-DHAQ	494	Edge at ~ 496 (single crystal, 25 K) [75]
1,8-DHAQ	501	1 st shoulder peak at ~ 460 (powder in KBr, 77 K) [60]
1,4-DHAQ	578	1 st shoulder peak at 573 (powder in KBr, 77 K) [94]

5.2 Quantum chemical calculations

The vertical excitation energies up to 20th level including forbidden transitions of 1,5-, 1,8-, and 1,4-DHAQ solutions in acetonitrile and crystals are computed with time-dependent density functional theory (TD-DFT) methods. The detail of the computation is described in section 3.3 in Chapter 3 and the coordinates of crystals used for input files are in Appendix (Table A 1 – 3). Table 5.3 – 5.5 show the calculated excitation energies and respective oscillator strengths at allowed levels of solutions and crystals of 1,5-, 1,8-, and 1,4-DHAQ, respectively. The numbers are visualised in Figure 5.1, representing the relative oscillation strengths of the transitions by the heights of the solid bars positioned at their respective energies under the absorption spectra. As shown in the plots, the energy levels of the crystals lie closer than the levels of the solutions. It supports that the broad absorption bands of crystal samples arise from the narrowed gaps between the energy levels.

Table 5.3. Calculated electronic excited state energies and oscillator strengths of 1,5-DHAQ crystal and solution. Forbidden (oscillator strength = 0) states are omitted.

		Excited state Excitation energy (nm)	Oscillator strength
Solution	1	401.00	0.2365
	6	274.59	0.1902
	8	266.85	0.0148
	13	224.78	0.8851
	14	224.64	0.0005
	18	210.92	0.0924
	20	205.32	0.0001
Crystal	1	449.01	0.0007
	3	447.30	0.0197
	6	438.10	0.0356
	8	433.02	0.0034
	10	422.25	0.0027
	12	418.76	0.1403
	14	414.48	0.1174
	16	412.20	0.0415
	18	409.11	0.0346
	20	407.40	0.2534

Table 5.4. Calculated electronic excited state energies and oscillator strengths of 1,8-DHAQ crystal and solution. Forbidden (oscillator strength = 0) states are omitted.

	Excited state	Excitation energy (nm)	Oscillator strength	
Solution	2	404.23	0.2245	
	3	380.78	0.0014	
	5	331.24	0.0059	
	6	274.87	0.1836	
	7	269.00	0.0157	
	8	266.56	0.0128	
	11	244.02	0.0282	
	12	243.39	0.0004	
	13	225.04	0.0005	
	14	224.55	0.8627	
	15	215.55	0.0125	
	16	213.38	0.0001	
	18	210.95	0.032	
	19	210.74	0.059	
	Crystal	1	444.10	0.0023
		2	442.31	0.0301
		3	440.19	0.0541
		4	436.87	0.0141
		5	434.37	0.0163
6		433.99	0.0993	
7		433.50	0.0208	
8		432.17	0.0157	
9		430.57	0.04727	
10		430.15	0.0165	
11		428.71	0.011	
12		428.06	0.0081	
13		426.86	0.0099	
14		425.59	0.0209	
15		423.50	0.0147	
16		420.48	0.0771	
17		419.42	0.0012	
18		418.15	0.0048	
19		416.30	0.0232	
20		415.80	0.0064	

Table 5.5. Calculated electronic excited state energies and oscillator strengths of 1,4-DHAQ crystal and solution. Forbidden (oscillator strength = 0) states are omitted.

	Excited state	Excitation energy (nm)	Oscillator strength
Solution	1	449.69	0.1704
	4	330.48	0.0012
	5	332.20	0.0613
	6	309.88	0.0068
	7	274.66	0.1758
	8	264.93	0.0182
	11	239.02	0.0140
	12	237.30	0.4521
	13	232.48	0.0054
	14	225.60	0.0005
	15	222.98	0.1514
16	220.95	0.0791	
19	204.35	0.4251	
20	203.50	0.0002	
Crystal	1	517.53	0.0085
	4	514.59	0.0010
	6	503.56	0.0055
	8	490.33	0.0021
	9	487.87	0.0347
	11	486.52	0.0002
	13	483.46	0.0263
	15	480.56	0.0364
	17	476.07	0.0023
18	473.51	0.0044	

Stacking of the molecules in crystals induces intermolecular interactions, which possibly perturb the energy relaxation pathways for excited states as discussed in chapter 2. To approximate the degree of intermolecular interactions, Coulomb coupling of the S_0 to S_1 transition dipole moments between two molecules are calculated. Again, the detail of the computation is described in section 3.3 in chapter 3 and the coordinates used for input files are in the Appendix. Table 5.6 shows that the transitions contribute to the first excited state of each molecular system. The respective molecular orbitals of the contributions are depicted in Figure 5.2 – 5.4. Due to the molecular geometry, ($\pi \pi^*$) transitions in 1,5-, 1,8-, and 1,4-DHAQs form dipoles in the molecular planes. In Figure 5.5, the directions of transition dipole moments are represented with green arrows. The Coulomb interactions between the neighboring molecules are calculated in Table 5.7. The couplings in 1,5- and 1,4-DHAQ are stronger than in 1,8-DHAQ. From these findings, combined with the existence of intermolecular hydrogen bonds as revealed with the crystal structure determination, it is presumed that the lattice structure of 1,5- and 1,4-DHAQ would more strongly influence the excited state dynamics related to the proton transfer reactions than the 1,8-DHAQ analogue and solution phase for all three systems as well.

Table 5.6. Transitions contribute to the first excitation of 1,5-, 1,8-, and 1,4-DHAQ solutions.

	Transition	Amplitude
1,5-DHAQ	HOMO \rightarrow LUMO	0.70262
	HOMO-4 \rightarrow LUMO	0.12850
1,8-DHAQ	HOMO-4 \rightarrow LUMO+1	0.10192
	HOMO-2 \rightarrow LUMO	0.68319
1,4-DHAQ	HOMO \rightarrow LUMO	0.70325

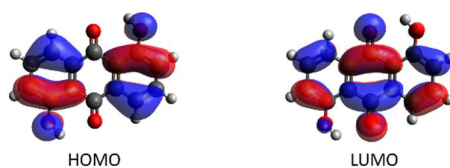


Figure 5.2. Molecular orbitals of 1,5-DHAQ solution.

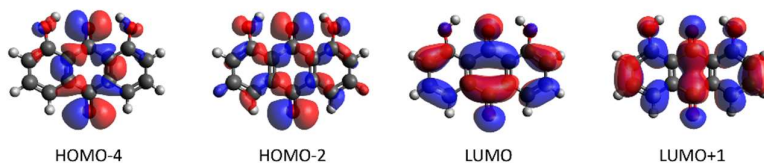


Figure 5.3. Molecular orbitals of 1,8-DHAQ solution.

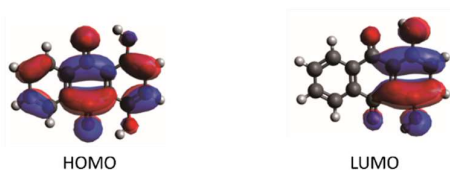


Figure 5.4. Molecular orbitals of 1,4-DHAQ solution.

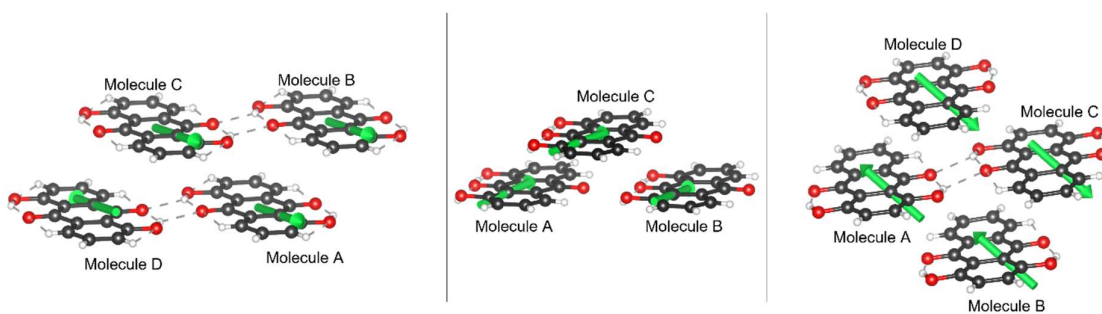


Figure 5.5 Depiction of the molecular coordinates used for transition dipole moments coupling calculations. Left: 1,5-DHAQ, middle: 1,8-DHAQ, right: 1,4-DHAQ. Green arrows indicate the directions of transition dipole moments. Note that the length of the depicted transition dipole moment is arbitrary, not showing the magnitude.

Table 5.7. Coulomb coupling of S_0 to S_1 transition dipole moments between two molecules labeled in Figure 5.5 in unit of cm^{-1} .

	1,5-DHAQ	1,8-DHAQ	1,4-DHAQ
Molecule A \leftrightarrow B	539.78	Molecule A \leftrightarrow B 24.09	Molecule A \leftrightarrow B 570.40
Molecule A \leftrightarrow C	382.86	Molecule B \leftrightarrow C 82.29	Molecule A \leftrightarrow C 385.35
Molecule A \leftrightarrow D	-302.73	Molecule C \leftrightarrow A 81.34	Molecule A \leftrightarrow D -34.40

The computation above is an approach to understand the charge shift through excitonic coupling in terms of the electrostatic interactions between two transition dipoles [95]. The molecular orbitals in the crystal lattice structure, not in a single molecule, can give supramolecular insights to the transitions. For linear excitations described above, an 8-molecule-in-lattice model is employed in the treatment of the DHAQ molecular crystals. It should be noted that real crystal is composed of unlimited number of molecules forming symmetries, therefore, periodic boundary conditions must be used for more precise predictions. Nevertheless, the calculation results with the 8-molecule model are already distinguishable against the results with the solution model, supporting the different absorption spectral shapes in solution and crystal as mentioned above. Here, the orbitals of the crystals which are involved in the excitation to first energy level are drawn in Figure 5.6 – 5.8, showing the delocalised excitations.

Table 5.8. Transitions contribute to the first excitation of 1,5-, 1,8-, and 1,4-DHAQ crystals.

	Transition	Amplitude
Solution	HOMO → LUMO	0.70262
1,5-DHAQ	HOMO-3 → LUMO	0.13166
	HOMO-1 → LUMO+1	0.31358
	HOMO → LUMO	0.52727
	HOMO → LUMO+2	-0.27189
1,8-DHAQ	HOMO-1 → LUMO+4	0.43170
	HOMO-1 → LUMO+5	0.17789
	HOMO → LUMO+4	0.45464
	HOMO → LUMO+5	0.18351
1,4-DHAQ	HOMO-1 → LUMO+1	0.35495
	HOMO → LUMO	0.59938

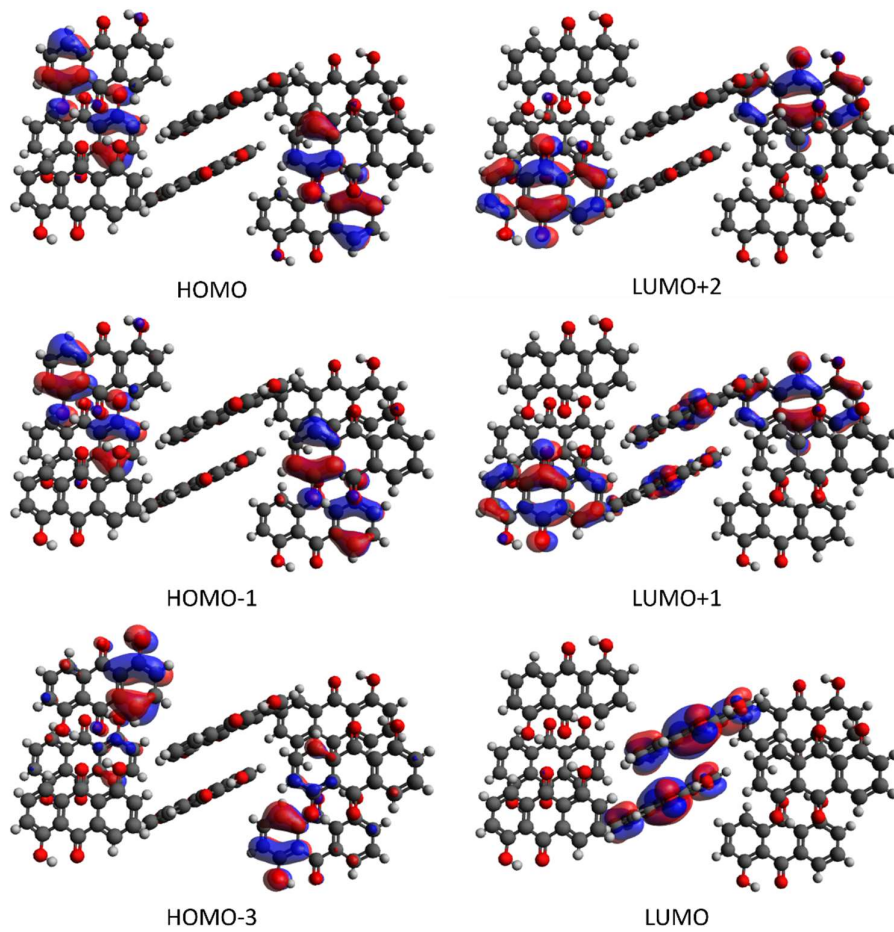


Figure 5.6. Molecular orbitals of 1,5-DHAQ crystal.

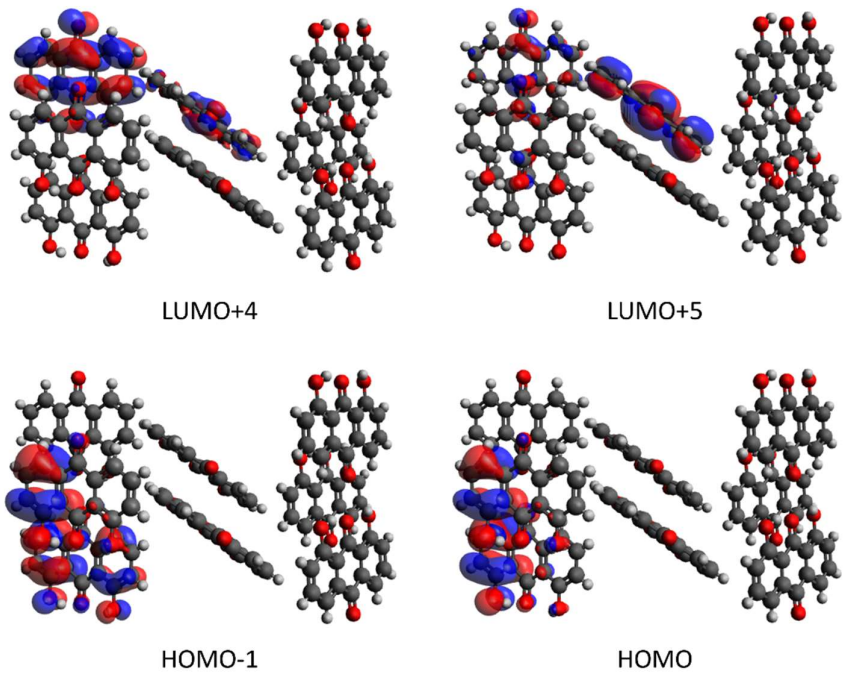


Figure 5.7. Molecular orbitals of 1,8-DHAQ crystal.

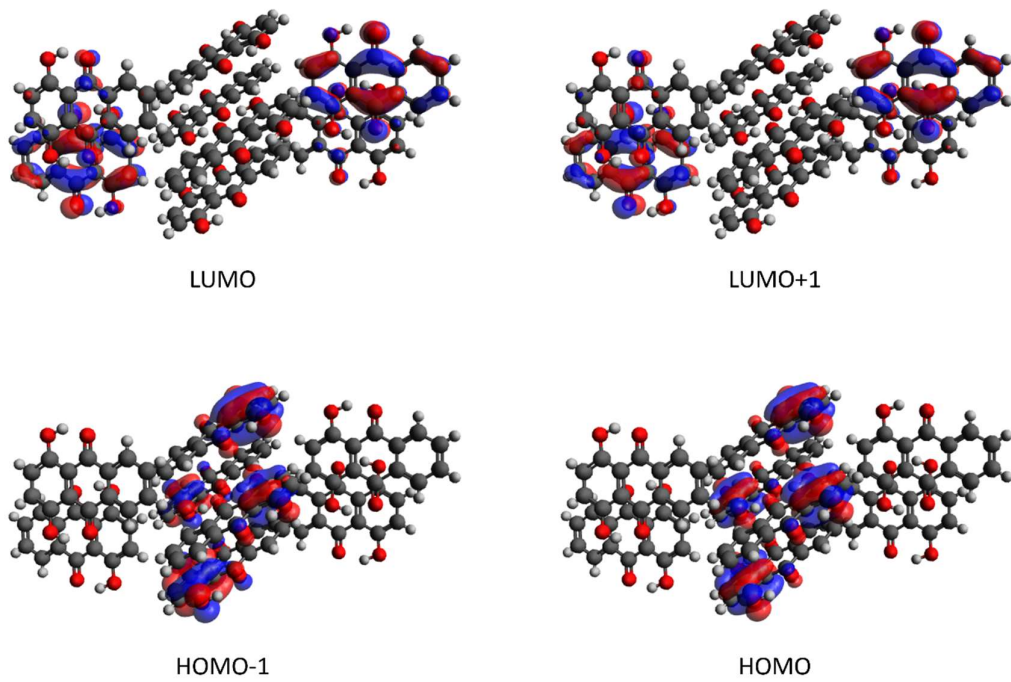


Figure 5.8. Molecular orbitals of 1,4-DHAQ crystal.

Chapter 6. Excited State Dynamics: Femtosecond Transient Absorption

The crystal structures of 1,5-, 1,4-, and 1,8-DHAQ characterized in chapter 4 showed that all the molecules in the crystalline form are packed by π - π interaction between molecular layers, and these molecular layers are formed by intermolecular hydrogen bonds except for 1,8-DHAQ. The electronic absorption spectra of these crystals and their respective solutions described in chapter 5 signified that the delocalized frontier molecular orbitals in crystals induce lowering of electronic resonant excitation energy and broader absorption bands, which are also supported by TD-DFT calculations. Furthermore, the interactions between transition dipole moments of the individual molecules in the lattice revealed the extent of excitonic couplings in different hydroxyanthraquinone systems. In this chapter, the effect of these excitonic couplings on modulating proton transfer reaction dynamics in crystalline bath as compared to respective dynamics in solution is investigated using the femtosecond transient absorption spectroscopy.

6.1 Excited state dynamics in solution phase

In this section, the transient dynamics of the three molecular systems: 1,5-, 1,4-, and 1,8-DHAQs in acetonitrile solutions have been described (details of the experimental set up have been provided in Chapter 3). 1,8-DHAQ has been studied previously using femtosecond transient absorption (TA) spectroscopy in benzyl alcohol, methanol, acetonitrile, and dimethyl sulfoxide solvent systems [65, 67]. Solutions dynamics of 1,5- and 1,4-DHAQs have not been studied using TA spectroscopy. To make a direct comparison of the excited state dynamics in acetonitrile solvent vs crystals, the excitation wavelengths used for the measurements are kept the same for solutions and in the respective crystals (described in section 6.2). The role of solvent bath in proton transfer dynamics in hydroxyanthraquinones have been described in various literature reports [67, 96, 97]. The measurements here have been limited to one solvent system i.e., acetonitrile. The excited state dynamics of molecules in acetonitrile solutions measured here are also compared and interpreted with the help of reported steady state and time-resolved results.

6.1.1 1,5-Dihydroxyanthraquinone

The TA data of 1,5-DHAQ solution in acetonitrile solution is measured with 343 nm as the excitation pump pulse with three different excitation photon fluences, 2.1, 2.7 and 3.1 mJ/cm², as shown in Figure 6.1. The transient spectra at selected delay time points with 2.7 mJ/cm² pump are plotted in Figure 6.2a. The power dependence in Figure 6.2b shows the excitation at photon fluence 2.7 mJ/cm² is in the linear regime. Excited state absorption (ESA) band in Figure 6.2a shows sharp peak at around 500 nm. Stimulated emission (SE) band is broad (550 – 800 nm) and has structured features. Van Benthem et al. discussed ESIPT in 1,5-DHAQ by showing dual fluorescence [58]. The two bands in emission spectra are observed: 485 – 540 nm band and in wavelength regime longer than 550 nm. From the comparison of emission spectra collected with various deuterium substituted 1,5-DHAQ, they interpreted the fluorescence intensity increase in short wavelength fluorescence (480 – 550) is activated by low-frequency skeletal mode and long wavelength fluorescence (560 – 575) is activated by O-H stretch mode. Thus, the longer wavelength emission band is considered to come after proton transfer in the excited state.

The kinetic traces at longer than 500 nm are best fitted with a bi-exponential function, and those between 490 and 500 nm are better fit with a tri-exponential function. In Figure 6.2c, three traces at 500, 510, and 630 nm and their exponential fit curves are plotted. All of them have several hundred picosecond decay time components, which is assigned to population decay of the excited states. Van Benthem et al. [58] mentioned observation of single exponential decay with a lifetime of 400 ps after a fast rise, which was not resolvable in their time-resolved fluorescence measurement. This observation is also in agreement with the results of Cho et al [98]. The centroid of ESA shifts from 511 nm to 507 nm within 100 ps with a fast time component of 13 ps (Figure 6.2d). This can be assigned as vibrational redistribution and solvation, which is in accordance with time-resolved fluorescence results by Arzhantsev et al. [65] and time-resolved IR absorption measurements by Mohammed et al. [67], for 1,8-DHAQ solutions. The kinetic analysis of ESA at 500 nm shows an additional short time component of 280 fs, which possibly corresponds to the proton transfer timescale. In the decay-associated spectra (DAS) a spectral component with 329 fs is revealed (blue curve in Figure 6.2e), which shows an emission feature at 505 nm and a broad absorption ranging from 570 to 800 nm. This short-lived component represents initially populated S₁ state with emission at 505 nm and broad absorption corresponds to its ESA. The other spectral components in DAS analysis correspond to the proton-transferred state with ~12 ps vibrational cooling timescales and the long-lived component refers to decay of the excited state. The clear blue shift can be observed in ESA feature of the proton-transferred state in DAS spectral components, which is earlier assigned to the vibrational cooling.

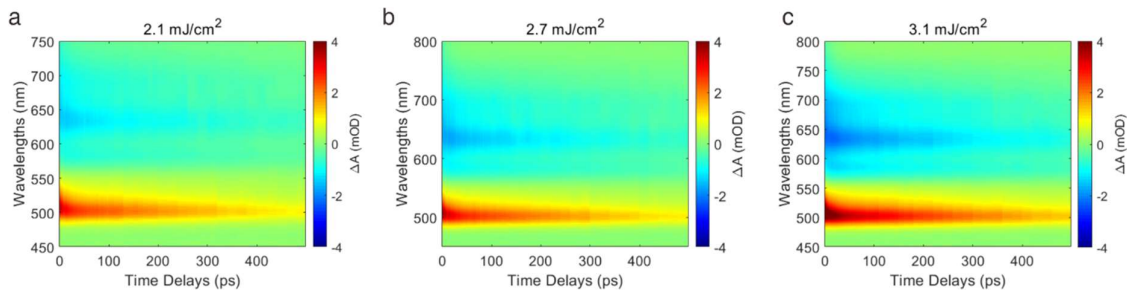


Figure 6.1. Excitation pump fluence dependence. 2D colour plots of TA of 1,5-DHAQ solution in acetonitrile with three different photon fluences.

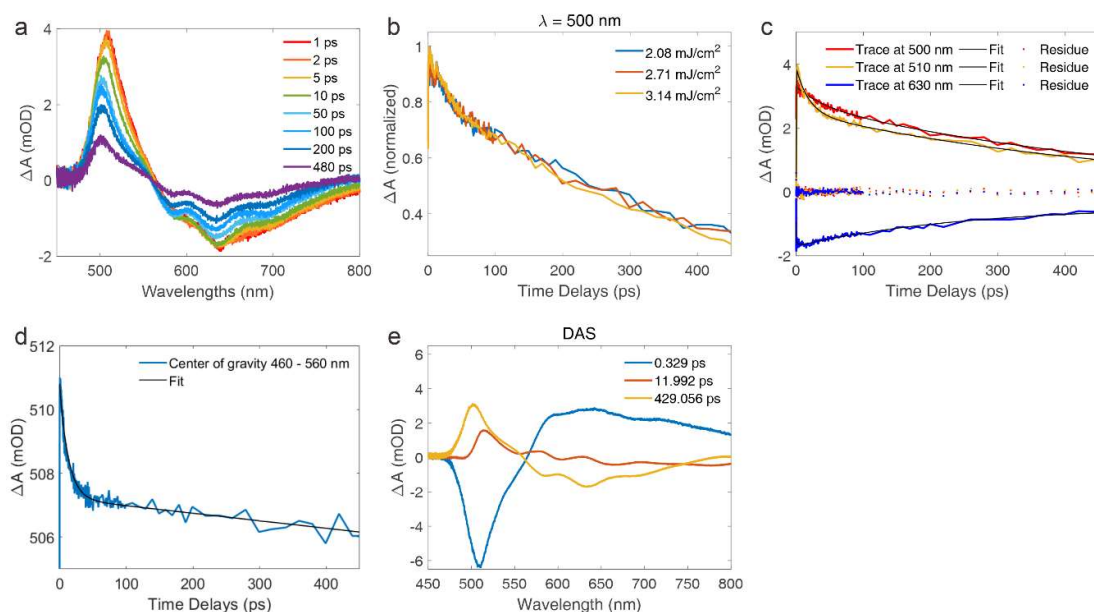


Figure 6.2. Fs-transient absorption measurements on 1,5-DHAQ solution in acetonitrile. Pump wavelength is 343 nm. (a) Spectral profile at photon fluence 2.7 mJ/cm^2 . (b) Normalized kinetic traces at 500 nm with different photon fluence. The power dependence shows that the excitation is in linear regime. (c) Exponential fit of kinetic traces of ESA (red) and SE (blue) at photon fluence 2.7 mJ/cm^2 . (d) Dynamics of centroid of ESA band between 460 and 560 nm (blue line). The black curve refers to the exponential fit to the experimental data. (e) Decay-associated spectra (DAS) obtained by global fitting the TA spectra at photon fluence 2.7 mJ/cm^2 with parallel model.

Table 6.1. Exponential fit parameters of the kinetic traces presented in Figure 6.2c.

	A_1 (mOD)	τ_1 (ps)	A_2 (mOD)	τ_2 (ps)	A_3 (mOD)	τ_3 (ps)
500 nm	-3.6 ± 1.2	0.279 ± 0.014	0.56 ± 0.16	40 ± 11	3.0 ± 1.0	600 ± 400
510 nm	1.36 ± 0.04	18.4 ± 1.4	2.50 ± 0.05	494 ± 33		
630 nm	0.145 ± 0.028	3.8 ± 1.7	-1.25 ± 0.11	250 ± 50		

6.1.2 1,8-Dihydroxyanthraquinone

1,8-DHAQ solution in acetonitrile is measured with excitation wavelength 400 nm and photon fluences 1, 2, and 3 mJ/cm² (Figure 6.3). In Figure 6.4a-c, the data at photon fluence 1 mJ/cm² are analysed since the excitation is in the linear regime, which was confirmed by the power dependence (Figure 6.4d). The spectral shape and decay dynamics are similar to those of TA result of 1,5-DHAQ solution (Figure 6.4a): a long-lived ESA band in between 450 – 500 nm and a broad SE band in 550 – 700 nm region. 1,8-DHAQ is also known to show dual emission bands and fluorescence spectra with deuterated substitutions proves occurrence of photoinduced proton transfer in this system [93]. Mohammed et al. observed solvent-dependent fluorescence spectra of 1,8-DHAQ showing dual emission, where the emission band between 600 – 650 nm was fluorescence of tautomeric form [67].

The kinetic traces of one point in ESA (480 nm) and one in SE (630 nm) bands are best fitted with bi-exponential function consisting of one rising component below 10 ps and a decaying component in hundreds of picoseconds (Figure 6.4b, Table 6.2). On the other hand, the kinetic traces between 485 – 500 nm are best fitted with tri-exponential function having additional sub-picosecond time component. As a representative, Figure 6.5b shows the kinetic trace at 485 nm and its exponential fit curve.

The several-hundred picosecond decaying component is the lifetime of the electronic excited state, in agreement with previous studies of time-resolved fluorescence and TA performed by Mohammed et al [67]. In addition, they observed decay lifetimes in 20 – 35 ps and 180 – 139 ps from the transient IR spectra of 1,8-DHAQ solution in acetonitrile-d₃ and dimethyl sulfoxide-d₆. The early time component was conjectured to be from vibrational relaxations and solvation dynamics by comparing the results of different spectroscopic methods. Particularly, the time scale of upshifting of the excited state band from 1419 cm⁻¹ to 1429 cm⁻¹ was 8.7 ps in tetrachloroethene and similar in acetonitrile-d₃, which is ascribed to vibrational relaxations. Furthermore, Arzhantsev et al. proposed photoexcitation causes vibrational delocalization of the proton in an elevated vibrational state at S₁ state, rather than producing the normal form and the tautomer as two different chemical species. Then the proton translocates to shift toward the tautomeric form during the intramolecular vibrational relaxation [65]. Their 400-nm-pumped time-resolved fluorescence of 1,8-DHAQ solution in hexane showed emission at short wavelengths with fast decays of <2 ps and at long wavelengths a rise <2 ps, which is followed by slow decay with a time constant of 127 ps corresponding to the lifetime of S₁ state. The few-ps dynamics were assigned to the additional proton translocation after delocalization of the wave packet. In accordance with the literature, the time component of 8 -13 ps in the present results is assumed to be the vestige of the vibrational relaxation involving proton translocation.

In the present work, the kinetic traces between 485 – 500 nm reveal sub-picosecond time components. The DAS obtained by global fitting of the TA spectra at photon fluence 1 mJ/cm² show the short time

component of 297 fs as well, representing the blended signal of GSB and SE from the primary species around 480 nm (Figure 6.4c). By recalling the absorption structure of 1,8-DHAQ solution in section 5.1, the emissive feature between 450 – 500 nm band of the spectrum corresponds to the S_1 - S_0 transition. It agrees with the findings by Jethwa et al., where the SE rises with a time component of about 300 fs as observed in the TA spectra of 1,8-DHAQ in benzyl alcohol solution excited by 400 nm pulse [66]. This dynamical feature is suggested to be proton transfer or redistribution along the proton transfer coordinate based on Lippincott-Schroeder potential.

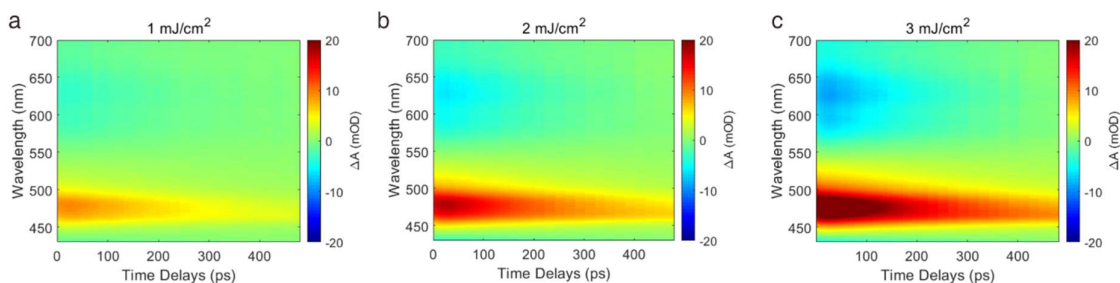


Figure 6.3. Excitation pump fluence dependence. 2D colour plots of TA of 1,8-DHAQ solution in acetonitrile with three different photon fluences.

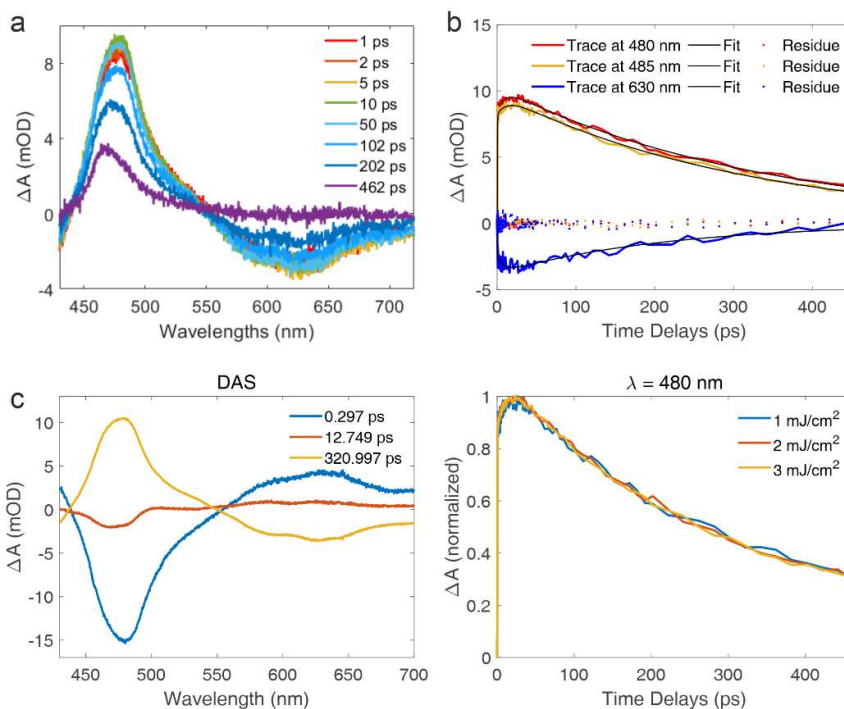


Figure 6.4. Fs-transient absorption measurements on 1,8-DHAQ solution in acetonitrile with the pump wavelength of 400 nm. (a) Spectral profile and (b) exponential fit of kinetic traces of ESA (red) and SE (blue) at photon fluence 1 mJ/cm². (c) DAS obtained by global fitting of the TA spectra at photon fluence 1 mJ/cm² with parallel model. (d) Normalized kinetic traces at 480 nm with three different photon fluences. The power dependence shows that the excitation at photon fluence 1 mJ/cm² is in linear regime.

Table 6.2. Exponential fit parameters of the kinetic traces presented in Figure 6.4b.

Wavelength	A_1 (mOD)	τ_1 (ps)	A_1 (mOD)	τ_1 (ps)	A_2 (mOD)	τ_2 (ps)
480 nm			-1.94 ± 0.5	8.4 ± 0.5	10.28 ± 0.05	338 ± 5
485 nm	-1.24 ± 0.10	0.41 ± 0.05	-1.54 ± 0.06	12.5 ± 1.3	9.79 ± 0.06	316 ± 5
630 nm			1.24 ± 0.09	8.5 ± 1.3	3.78 ± 0.09	213 ± 13

6.1.3 1,4-Dihydroxyanthraquinone

1,4-DHAQ solution in acetonitrile was measured with excitation wavelength 515 nm and photon fluences 0.04, 0.3, and 0.4 mJ/cm² (Figure 6.5). In Figure 6.6a-c, the data at photon fluence 0.04 mJ/cm² are analysed since the excitation is in linear regime, which was confirmed by the power dependence (In Figure 6.4a-c, the data at photon fluence 1 mJ/cm² are analysed since the excitation is in linear regime, which was confirmed by the power dependence (Figure 6.6d). The spectral profile of the transient data shows an ESA band in between 520 – 565 nm and a SE band between 570 – 750 nm with vibronic structural features (Figure 6.6a). From the previous reports of fluorescence measurements of 1,4-DHAQ solutions, the emission showed S₁-S₀ transition is at 522.7 nm (in n-heptane) [63] and peak at 570 nm with a shoulder at 545 nm in water [99], while in isopropanol, the peaks were at 536 nm and 565 nm [100]. In the transient spectra shown here in Figure 6.6a, the short wavelength emission band is screened by ESA, but it does show emission peaks at 630 nm and 585 nm.

The kinetic trace of SE at 630 nm and the trace of ESA at 540 nm is fitted with bi-exponential function (Figure 6.6b). The fit parameters are listed in Table 6.3. Both traces rise with a time constant of 11.8 ps, and they live longer than the measured time window, 500 ps (Figure 6.6c). The lifetime of the resonantly excited state of 1,4-DHAQ molecule in gas phase was also reported to be 1.7 ns by Berenbeim et al [8]. Thus, the longer decay time component is kept fixed at 1.7 ns for exponential fitting of the kinetic data. The hydroxyanthraquinones with 1,4-motif show comparatively longer lifetimes than those without the 1,4-motif. It is proposed to increase in decay time due to the absence of the non-radiative dissipation route through the proton transfer process, as introduced in Section 2.2.2 in Chapter 2. By taking into the excited state nature, the global rise time component of about 10 ps as shown by kinetics, and DAS, this dynamic feature is related to the vibrational relaxation time at the S₁ ($\pi\pi^*$) state.

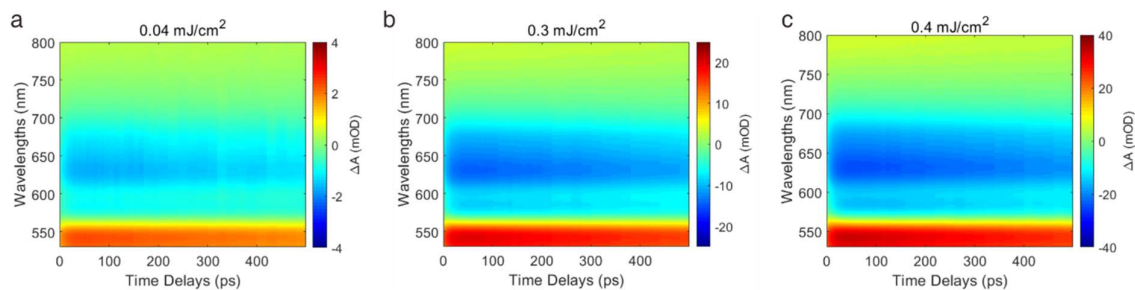


Figure 6.5. Excitation pump fluence dependence. 2D colour plots of TA of 1,4-DHAQ solution in acetonitrile with three different photon fluences.

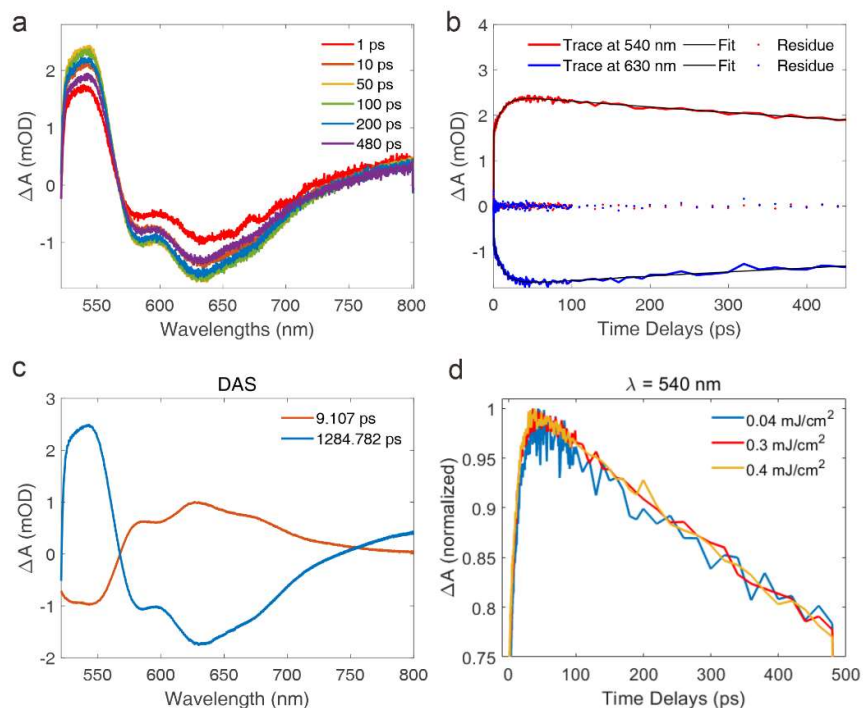


Figure 6.6. Fs-transient absorption measurements on 1,4-DHAQ solution in acetonitrile with pump wavelength of 515 nm. (a) Spectral profile and (b) exponential fit of kinetic traces of ESA (red) and SE (blue) at photon fluence 0.04 mJ/cm^2 . (c) DAS obtained by global fitting of TA spectra at photon fluence 0.04 mJ/cm^2 with parallel model. (d) Normalized kinetic traces at 540 nm with three different photon fluences showing linear 1-photon behaviour.

Table 6.3. Exponential fit parameters of the kinetic traces presented in Figure 6.6b.

Wavelength	A_1 (mOD)	τ_1 (ps)	A_2 (mOD)	τ_2 (ps)
540 nm	-0.804 ± 0.008	11.8 ± 0.4	2.446 ± 0.008	1760 ± 70
630 nm	0.907 ± 0.011	11.8 ± 0.4	-1.747 ± 0.010	1620 ± 110

6.2 Crystalline Phase

The excited state dynamics of 1,5-, 1,8-, and 1,4-DHAQ solutions agree well with previous research. The analysis of TA spectra from 1,5- and 1,8-DHAQ solution revealed sub-picosecond time components, which correspond to the ESIPT reaction. The fast time component is absent in the transient data of 1,4-DHAQ solution agreeing with the previous studies, which propose that the 1,4-DHAQ system does not favour the ESIPT pathway. In this section, the excited state dynamics of the crystals are analysed. The crystal samples are excited by the same pump wavelengths set to excite the corresponding levels from the solution phase studies for the respective molecular systems.

6.2.1 1,5-Dihydroxyanthraquinone

1,5-DHAQ crystal is measured with excitation photon fluences of 1.1, 2.7, and 3.1 mJ/cm², with pump excitation wavelength of 343 nm (Figure 6.7). The TA spectra of 1,5-DHAQ crystal show broad ESA in between 550 – 800 nm (Figure 6.8a). This observed broadness in ESA is analogous to the broad static absorption as discussed in Chapter 5, which is caused by the manifold of energy levels in the crystalline phase. It means the emission band will be broad as well, and the observed experimental spectra exhibit superpositions of GB, ESA, and SE. Unlike transient spectra from solution measurements, stimulated emission here is rendered invisible by the presence of overlapping broad absorption band. In Figure 6.8, the differential absorption spectral profiles show a peak at around 565 nm at early delay times (<1 ps) and longer-lived species at longer wavelength.

In Figure 6.8b, the kinetic traces at 565 nm and at two other wavelength points in longer wavelength regions show different decay dynamics: the trace at 565 nm is fit with a bi-exponential function, on the other hand, the traces at 670 nm and 700 nm are better fit with a tri-exponential function. The fit parameters are listed in Table 6.4. The τ_1 's of all the fits are below the time resolution (190 fs), and all the traces have (sub-)picosecond decay component at the early stage. The traces at 670 nm and 700 nm have additional longer time components of about 10 ps.

Wei et al. witnessed ESIPT occurring in dispersed 1,5-DHAQ micro crystals by steady state and time-resolved fluorescence measurements [59], where the crystals showed emission peaks at 575, 620, 675, 725 nm. The lifetimes of the four emission bands were sub-nanosecond long, while the emission at 575 nm had an additional decaying time component of 1.4 ps. This picosecond decay was inferred to be evidence of the proton transfer path in operation, while the sub-nanosecond decay is from fluorescence. Therefore, they conjectured the emission at 575 nm was from normal form and other three bands were from the proton transferred form. In this work, by taking into account the observation that the trace at 565 nm lacks the radiative decaying species, the sub-picosecond time component can be conjectured to be the proton transfer step. And the lifetime of decay, about 10 ps, which is shorter than the lifetimes assigned to radiative decay in solution in the present work and in microcrystals in [59] implies the

existence of other non-radiative channels dominating in crystalline phase. The time-resolved IR measurements of 1,5-DHAQ particles by Towrie et al [56] reviewed in section 2.2.2 support the possibility of the additional non-radiative pathway associated with proton transfer.

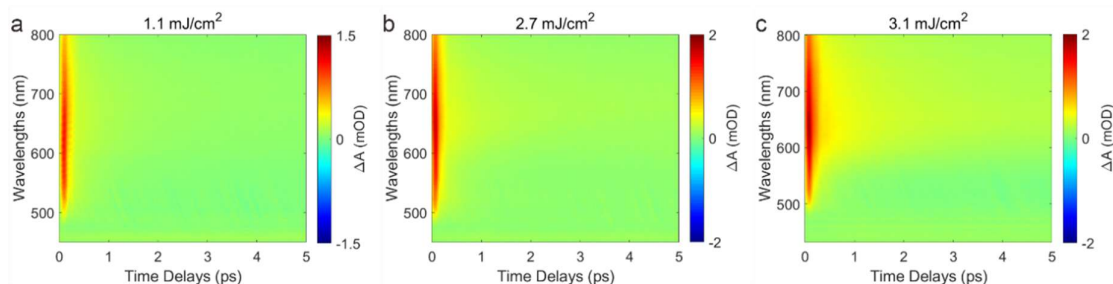


Figure 6.7. Excitation pump fluence dependence. 2D colour plots of TA of 1,5-DHAQ crystal with three different photon fluences.

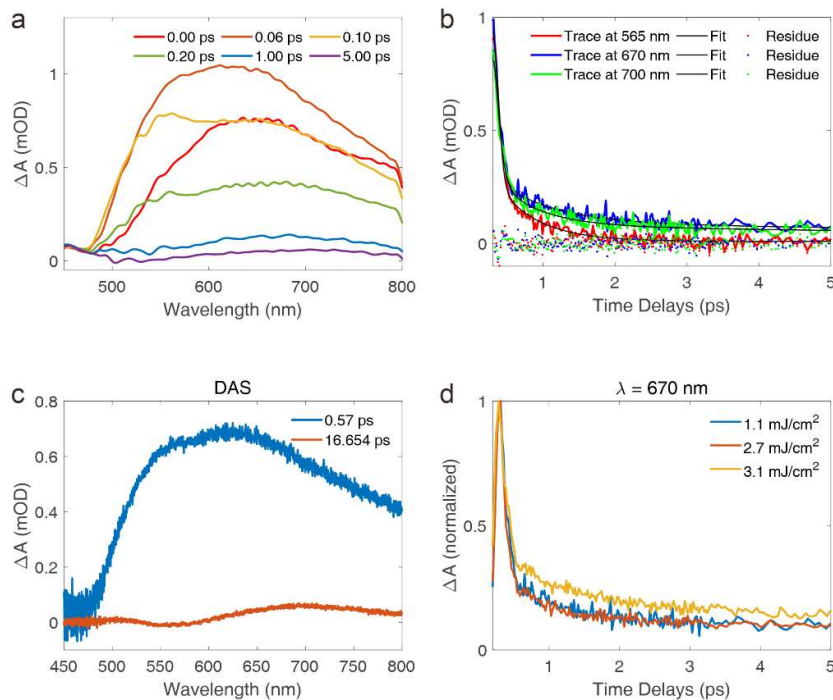


Figure 6.8. Fs-transient absorption measurements on 1,5-DHAQ crystal. (a) Spectral profile of 1,5-DHAQ crystal at photon fluence 1.1 mJ/cm². The power dependence shows that the excitation is in the linear regime. (b) Kinetic traces at 565 nm, 670 nm, and 700 nm. (c) DAS obtained by global fitting of the TA spectra at photon fluence 1.1 mJ/cm² with parallel model. (d) Normalized kinetic traces at 670 nm with three different photon fluences. Pump wavelength is 343 nm.

Table 6.4. Exponential fit parameters of the kinetic traces presented in Figure 6.8b.

	A ₁ (mOD)	τ ₁ (ps)	A ₂ (mOD)	τ ₂ (ps)	A ₃ (mOD)	τ ₃ (ps)
565 nm	3.1 ± 0.6	< 190 fs	0.289 ± 0.031	0.56 ± 0.06		
670 nm	2.44 ± 0.28	< 190 fs	0.211 ± 0.029	0.78 ± 0.20	0.058 ± 0.017	9 ± 5
700 nm	1.73 ± 0.17	< 190 fs	0.23 ± 0.04	0.60 ± 0.13	0.072 ± 0.009	12 ± 4

6.2.2 1,8-Dihydroxyanthraquinone

The transient absorption of 1,8-DHAQ crystal is measured with excitation photon fluences 0.75, 1, and 2 mJ/cm², with pump excitation wavelength of 400 nm (Figure 6.9). The transient spectra show broad ESA band like 1,5-DHAQ crystal. The fluorescence of 1,8-DHAQ crystal in this polymorph was reported to show peaks at 496.28, 568.50, and 594.88 nm [60], where the two lower energy bands are due to transitions from the proton transferred form. Here in the TA spectra, these emission bands are screened by the manifold of absorptive features. The observed dip with local minima at 462 nm (Figure 6.10a) is displaced 3350 cm⁻¹ from the excitation energy, which corresponds to a Raman vibrational band for the O-H stretch [101]. Fourier-transform infrared spectroscopy (FTIR) on 1,8-DHAQ solution showed weak absorbance from 2900 to 3400 cm⁻¹ which was suggested to be also due to O-H stretching modes involving the intramolecular hydrogen bond [67].

From the result with pump fluence 0.75 mJ·cm⁻², the kinetic trace at 515 nm is fitted with tri-exponential function (Figure 6.10b, Table 6.5). The fit results of 1,8-DHAQ crystal are similar to the results of 1,8-DHAQ solution, having sub-picosecond, a few 10 ps, and > 200 ps time components. Also, in the DAS in Figure 6.10c, the fastest time component is 216 fs. This is assigned to the timescale for proton transfer process at the S₁ state. The ESA band of the spectral component is in long wavelength region (> 500 nm). This ESA band is blue shifted in the spectral component with a 28 ps lifetime and further blue shifted in the spectrum with a 293 ps lifetime. Therefore, the time component of 28 ps is assigned to vibrational relaxation along the proton-transferred state and the time component 293 ps is assigned to decay of the electronic state, in analogy to the dynamics in solution phase.

It should be noted that 1,8-DHAQ crystal was sliced into 400 nm thick using ultramicrotomy, because micrometre-thick crystals did not show pump-probe signal. Its penetration depth is calculated in the previous chapter. The excitations with photon fluence 1 and 2 mJ·cm⁻² bring broad and long-lasting emissive features as plotted in Figure 6.9 b and c, because the excitations are not in linear regime as shown in power dependence (Figure 6.10d). This can be explained by the comparably higher excitation fraction than other two derivative crystals, due to the shorter path length and higher absorptivity of the sample at the excitation wavelength of 400 nm, matching the absorption maximum.

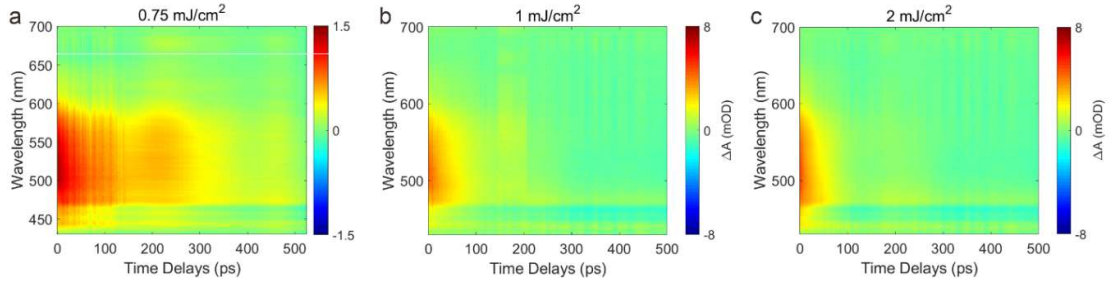


Figure 6.9. Excitation pump fluence dependence. 2D colour plots of TA of 1,8-DHAQ crystal with three different photon fluences.

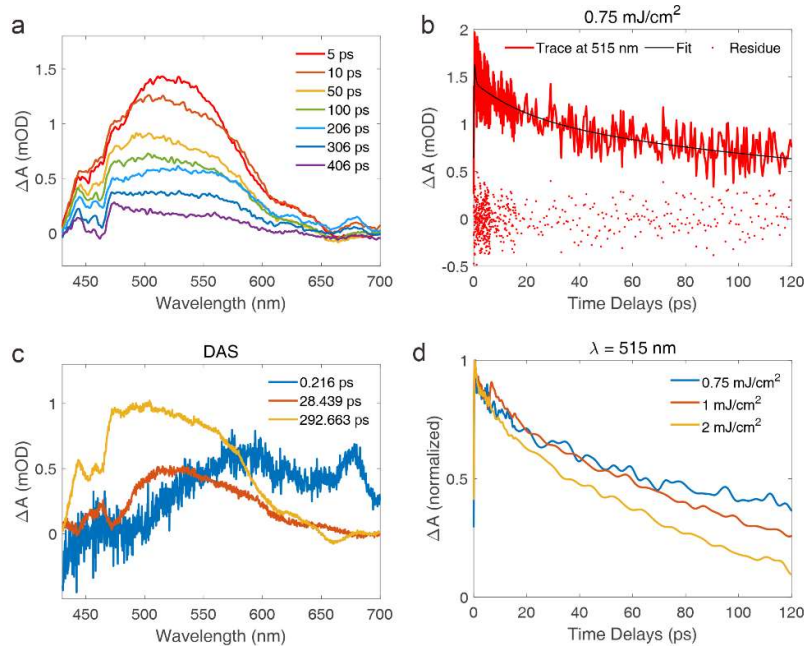


Figure 6.10. Fs-transient absorption measurements on 1,8-DHAQ crystal. (a) Spectral profile of TA of 1,8-DHAQ crystal at photon fluence 0.75 mJ/cm^2 . (b) Kinetic trace, exponential fit, and residue at 515 nm. (c) DAS obtained by global fitting with parallel model. (d) Normalized kinetic traces at 515 nm with three different photon fluences. Pump wavelength is 400 nm. The dependence is not linear above 1 mJ/cm^2 .

Table 6.5. Exponential fit parameters of the kinetic trace presented in Figure 6.10b.

	A_1 (mOD)	τ_1 (ps)	A_2 (mOD)	τ_2 (ps)	A_3 (mOD)	τ_3 (ps)
515 nm	0.59 ± 0.25	0.36 ± 0.16	0.40 ± 0.06	21 ± 6	1.05 ± 0.06	239 ± 28

6.2.3 1,4-Dihydroxyanthraquinone

1,4-DHAQ crystal is measured with excitation photon fluences of 0.2, 0.4, and 1.6 mJ/cm², at pump excitation wavelength of 515 nm (Figure 6.11). The TA spectra of 1,4-DHAQ crystal show positive signal over the probe wavelengths, but they are divided into three bands: the strongest signal in between 540 – 580 nm, and weaker band in 610 – 630 nm and in 660 – 750 nm (Figure 6.12a). The kinetic trace at 550nm is fit with a tri-exponential function and the trace at 560 nm is better fit with a bi-exponential function (Figure 6.12b, Table 6.6). Kinetic traces at longer wavelengths have low signal to noise ratio due to weak signals, which hinders extracting time components with low error values. Thus, the transient dynamics is further analysed by global fitting which provides spectral information associated with decay time components (Figure 6.12c). As shown in the DAS and single point fit results, the lifetime of electronic state is around 500 ps, which is shorter compared to the results from solution (longer than 1 ns, in section 6.1.3.). Also, the excited state has an additional short time component below 300 fs as revealed in the kinetic trace fit parameters at 550 nm as well as in the global fit result. The DAS spectrum of 249 fs component shows a GSB at around 550 nm and an ESA band at around 600 nm, which means that the component represents the lifetime of the primary species, S₁ state (normal form). The fast dynamics of the primary state implies a nonradiative pathway, which is postulated to be the proton transfer reaction in analogy of 1,5- and 1,8-DHAQ solution data. Consistently, the time component of a few picoseconds is assigned to relaxation within the vibrational manifolds.

The differed excited state dynamics in 1,4-DHAQ crystal compared to the dynamics in its solution suggest that the specific packing of the molecules modified the photophysical pathway or induced photochemical reaction in the molecule. Dutta et al. suggested that the intermolecular hydrogen bonding interactions in crystals alter the vibrational modes involving hydroxyl and carbonyl groups by comparing the electronic and vibrational spectra of two polymorphic 1,4-DHAQ crystals (Form I and II, The crystal structure of the 1,4-DHAQ system obtained in the current doctoral work is identical to the Form I.) [94]. They found that Form II showed spectral structure similar to that of solution, but Form I showed different vibronic structure. They interpreted the electronic spectrum of Form I to have a doublet excited state due to exciton energy splitting by the in-phase and out-of-phase arrangement of the transition dipoles. In the Raman spectra, the asymmetric δ_{OH} (1225 cm⁻¹) and ring stretch (1239 cm⁻¹) bands present in Form II as well as in solution, which are diminished in the spectrum of Form I. The ring stretching mode at 1407 cm⁻¹ in Form II was shifted to lower frequency in Form I due to the decrease in hydrogen bonding. In addition, a symmetric OH bending mode at 1205 cm⁻¹ appeared in Form I. Their findings indicated the intermolecular hydrogen bonds and excitonic couplings induced modification in the vibronic structure involving intramolecular hydrogen bonds. Berenbeim et al. discussed that the simultaneous motion of contraction at one intramolecular hydrogen bond and expansion at the other bond raise a barrier on the excited state potential energy surface [8]. Based on

the previous studies, the restricted and modified vibronic modes in the crystalline form are assumed to influence the transition state pathway in the excited state.

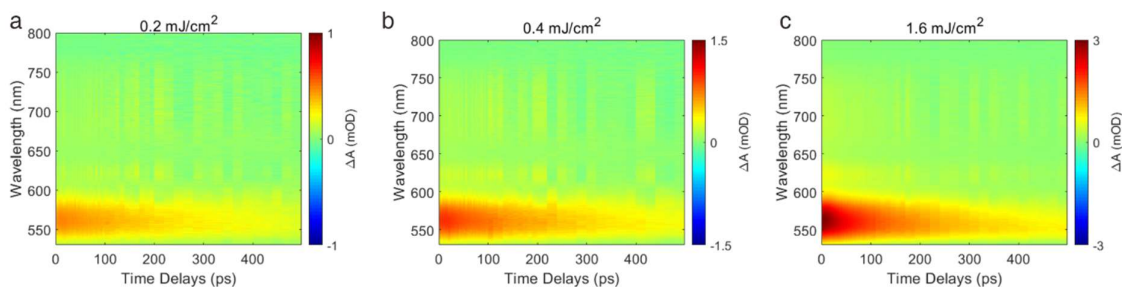


Figure 6.11. Excitation pump fluence dependence. 2D colour plots of TA of 1,4-DHAQ crystal with three different photon fluences.

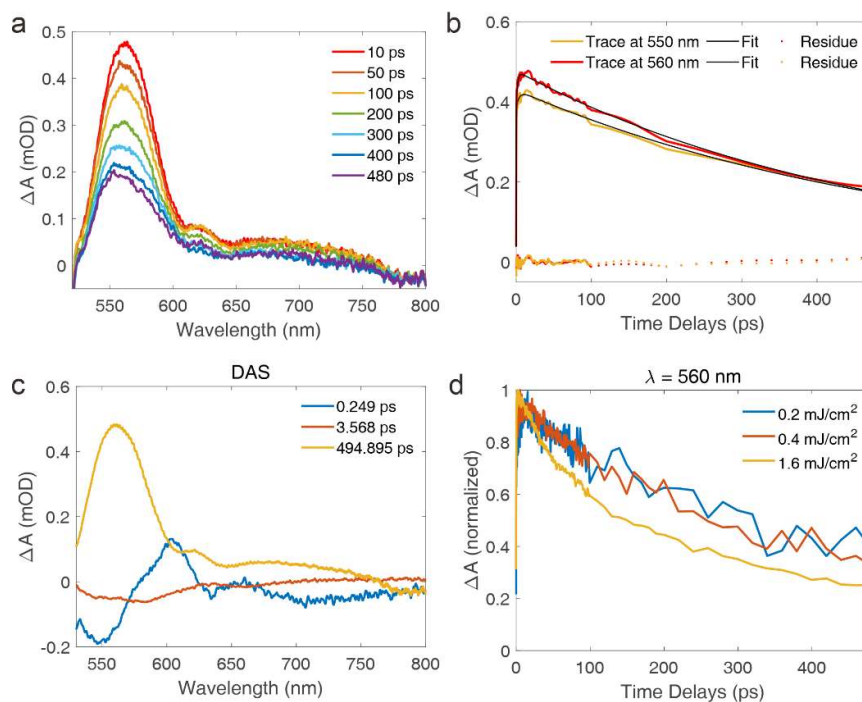


Figure 6.12. Fs- transient absorption measurements on 1,4-DHAQ. (a) Spectral profile of TA of 1,4-DHAQ crystal at photon fluence 0.2 mJ/cm^2 . The power dependence shows that the excitation is in linear regime. (b) Kinetic traces at 550 and 560 nm. (c) DAS obtained by global fitting with parallel model. (d) Normalized kinetic traces at 560 nm with three different photon fluences. Pump wavelength is 515 nm. The signal is nonlinear for excitation $> 0.4 \text{ mJ/cm}^2$.

Table 6.6. Exponential fit parameters of the kinetic traces presented in Figure 6.12b.

Wavelength	A_1 (mOD)	τ_1 (ps)	A_2 (mOD)	τ_2 (ps)	A_3 (mOD)	τ_3 (ps)
550 nm	-0.148 ± 0.011	0.246 ± 0.021	0.0446 ± 0.0024	3.9 ± 0.4	0.4296 ± 0.0009	523 ± 7
560 nm			-0.0859 ± 0.0016	1.82 ± 0.06	0.4781 ± 0.0007	477 ± 4

6.2.4 Discussion

The analysed time components by global fitting the TA spectra of the three molecular systems in solution and crystal phase are summarised and compared in Table 6.7. The dynamics of 1,8-DHAQ in crystal is not significantly changed compared to solution phase. However, the change in the dynamics of 1,5- and 1,4-DHAQ crystals are quite distinct from solution phase results. In the 1,5-DHAQ system, significantly longer dynamics are observed in crystal compared to solution. This indicates that other non-radiative pathways are preferred still against ESIPT in crystal. Meanwhile, interestingly, the excited dynamics in 1,4-DHAQ crystal look like the dynamics in 1,5- and 1,8-DHAQ solution. The crystal packing of 1,4-DHAQ in this polymorph is assumed to open non-radiative relaxation channel, possibly through ESIPT process.

As depicted in Figure 4.8, The 1,8-DHAQ molecules do not form intermolecular hydrogen bonds in the lattice, whereas 1,5- or 1,4-DHAQ molecules are linked by hydrogen bonds in a layer in the lattice. In addition, as discussed in section 5.2, the degree of excitonic coupling between 1,8-DHAQ molecules in the lattice is comparably less than other two systems. Based on the findings, I suggest those supramolecular interaction factors influence the photochemical reaction pathway by tuning the ESIPT reactivity.

Table 6.7. Time components of global fit of TA in 1,5-, 1,8-, and 1,4-DHAQ solutions and crystals.

		τ_1 (ps)	τ_2 (ps)	τ_3 (ps)
1,5-DHAQ	Solution	0.33	12.0	429
	Crystal	0.57	16.7	
1,8-DHAQ	Solution	0.30	12.7	321
	Crystal	0.22	28.4	293
1,4-DHAQ	Solution	-	9.1	1285
	Crystal	0.25	3.6	495

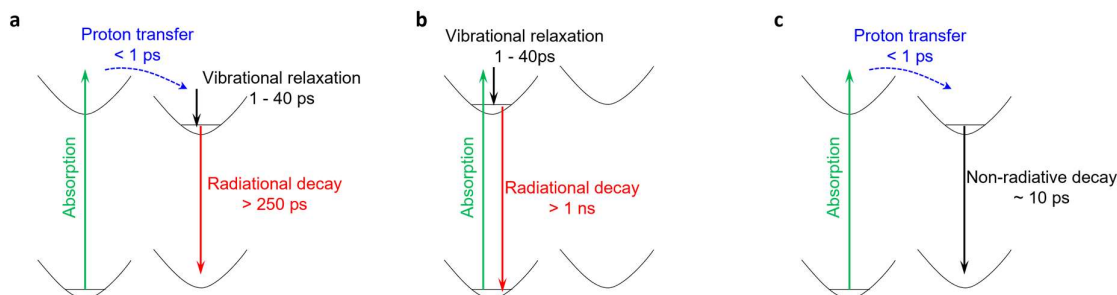


Figure 6.13. Schematic of the photo-induced dynamics representing (a) schematic potential energy diagram for solution phase 1,5- and 1,8-DHAQ and crystal forms of 1,4- and 1,8-DHAQ, (b) solution phase for 1,4-DHAQ, and (c) crystal for 1,5-DHAQ.

Chapter 7. Summary and Outlook

To summarize, I have developed a thin organic crystal growth method employing 2D spatial confinement. Three kinds of dihydroxyanthraquinone (DHAQ) derivatives have been grown in the 2D confined space generated by overlapping muscovite mica substrates while evaporation of their supersaturated solutions. The purpose of this development is to explore excited state reaction dynamics of ESIPT active molecules in ordered crystal lattices using ultrafast spectroscopy and diffraction methods. The density of the crystals on substrate was observed to be less in space-confined area. Additionally, crystals in the confined area are flatter and wider shaped compared to those in the open area. For example, thicknesses of the 1,5-DHAQ thin crystals were measured to be 1 – 1.75 μm by AFM. The spatial confinement provides a more restricted environment for nucleation and growth. The crystal structures of thin crystals were characterised by XRD, which matched with the reported crystal structures. Based on the crystal structures, 1,5- and 1,4-DHAQs, form intermolecular hydrogen bonds in crystals, whereas 1,8-DHAQ does not. The thin crystals of 1,5- and 1,4-DHAQ on mica were directly available for transmission-based optical measurements. Since 1,8-DHAQ has a smaller penetration depth at the excitation wavelength used, the crystal needed to be cut using ultramicrotomy. In this respect, this doctoral work includes a very important step in developing a general workflow to make thin enough crystals with large enough area for atomically resolved structural dynamics. The method is rather simple to implement and should be put forward as a new approach to open up imaging chemistry in action for a much broader class of systems than is now presently possible using conventional methods based on microtoming large crystals that can alter crystal quality. This new method provides an opportunity to observe photochemical reaction dynamics influenced by supramolecular interactions in crystal lattices. The crystal growth method has the possibility to be improved further to achieve thinner crystals with homogeneous thickness for a broader range of molecular systems. Also, it should be complemented with developments towards strategies on crystal-transfer from one to another substrate, which will enable various applications.

In the next part of this thesis, steady-state absorption measurements were conducted on solutions and crystals of the three molecular systems to examine resonant electronic excitation energies. The electronic energy levels were calculated using TD-DFT methods as well. The computed results are used here to decipher the nature of the experimentally observed electronic absorption bands. In addition, the molecular systems were also computed for excitonic couplings that play an important role in the excited state dynamics in crystals. The excitonic couplings between the transition dipole moments are strong in 1,5- and 1,4-DHAQ crystals (303 – 540 and 34 – 570 cm^{-1}) but rather weak in 1,8-DHAQ (24 – 82 cm^{-1}) crystals by comparison. To investigate the role of the crystal bath and the inherent excitonic couplings in crystals, I investigated the excited state dynamics in the DHAQ crystals and compared to the

dynamics in solution using fs-transient absorption spectroscopy. The results on solution samples agree with the previously reported research based on various steady-state and time-resolved spectroscopic methods: 1,5- and 1,8-DHAQ show sub-picosecond transient feature, which indicates ESIPT process, but 1,4-DHAQ does not show any evidence of ESIPT. The transient spectra of crystals showed a very different shape compared to solution, which may be a consequence of the narrowed gap between the energy levels due to the spatial delocalization of the electron distribution. The excited state dynamics in 1,8-DHAQ crystal was not significantly changed, however, other two systems displayed distinguishable dynamics in crystals. Excited species of 1,5-DHAQ crystal lived for much shorter time, with time component of 16.7 ps, whereas solution showed fluorescent decay living longer than 500 ps. For 1,4-DHAQ, the crystal form exhibited 250-fs time component, which was not present in the solution data. Also, the lifetime of electronic state was shortened from nanosecond to a few hundred picoseconds. The nature of the nonradiative decay pathways in 1,5-DHAQ crystal and fast decaying component in 1,4-DHAQ is yet to be assigned with complete confidence and needs further experimental efforts using different methods, though, the supramolecular interactions including intermolecular hydrogen bonds along with the excitonic couplings are presumed to play roles in opening new nonradiative channels in crystals. Since the photoinduced proton-transfer process results into dual emission bands, one can also capture the kinetics of the process by following the dynamics of emissive states, or radiative decay channels. Unfortunately, the broad absorption features in crystals hindered characterizing emissive feature using stimulated emission in TA spectra. Thus, femtosecond fluorescence up-conversion measurements may be useful to decipher the proton-transfer dynamics in these systems. Additionally, time-resolved vibrational spectroscopy will also be useful to get information of vibrational mode in specific changes accompanying the proton-transfer event. As has been discussed in the earlier chapters of this thesis, UED experiment is a powerful tool to directly capture the motions of hydrogen and surrounding atoms during the proton-transfer reaction. The great hope is to continue this work to directly observe the proton motion and prospects for observing a purely quantum event.

As preliminary work for UED experiments, 1,4-DHAQ crystal (100 nm cut) was tested in a home-built UED machine at low temperature (164 K). The details of the UED machine are described in [102]. For this test experiment, the electron pulse was accelerated to 90 keV and focused to ~130- μ m diameter. The diffraction image is obtained by accumulating 100 frames with 5 seconds exposure time (Figure 7.1). The temperature, pump fluence, electron energy, exposure time, and other parameters need to be optimized to gain differential diffraction signals containing physical meanings. Low-temperature fs TA experiments should also be conducted in parallel. The combination of these experiments will provide unprecedented information on the structural changes occurring during the excited state evolution involved in proton transfer – and with UED the prospect of observing nature's smallest nuclei in action – a truly quantum event.

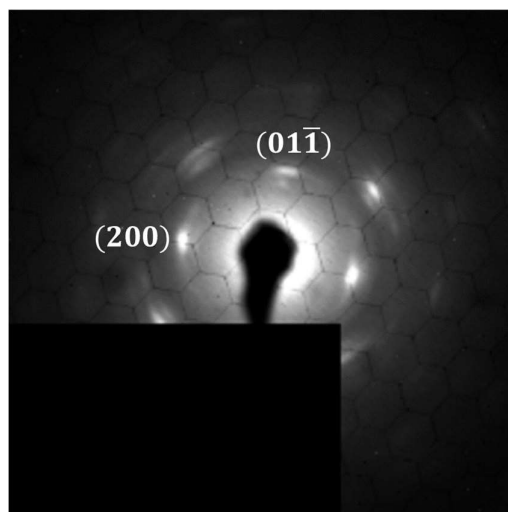


Figure 7.1. Static electron diffraction image of 1,4-DHAQ crystal obtained using femtosecond electron pulses.

Bibliography

- 1 Volkhard May, O.K., *Proton Transfer*, in *Charge and Energy Transfer Dynamics in Molecular Systems*. 2003. p. 377-403.
- 2 Watson, J.D. and F.H. Crick, *Genetical implications of the structure of deoxyribonucleic acid*. *Nature*, 1953. **171**(4361): p. 964-7.
- 3 Löwdin, P.-O., *Proton Tunneling in DNA and its Biological Implications*. *Reviews of Modern Physics*, 1963. **35**(3): p. 724-732.
- 4 Sassi, M., et al., *Hydrogen bond disruption in DNA base pairs from (14)C transmutation*. *J Phys Chem B*, 2014. **118**(35): p. 10430-5.
- 5 Slocombe, L., M. Sacchi, and J. Al-Khalili, *An open quantum systems approach to proton tunnelling in DNA*. *Communications Physics*, 2022. **5**(1): p. 109.
- 6 Singh, V., B.I. Fedeles, and J.M. Essigmann, *Role of tautomerism in RNA biochemistry*. *RNA*, 2015. **21**(1): p. 1-13.
- 7 Miliani, C., et al., *Photochemistry of Artists' Dyes and Pigments: Towards Better Understanding and Prevention of Colour Change in Works of Art*. *Angew Chem Int Ed Engl*, 2018. **57**(25): p. 7324-7334.
- 8 Berenbeim, J.A., et al., *Excited state intramolecular proton transfer in hydroxyanthraquinones: Toward predicting fading of organic red colorants in art*. *Science Advances*, 2019. **5**(9): p. eaaw5227.
- 9 Spence, D.E., P.N. Kean, and W. Sibbett, *60-fsec pulse generation from a self-mode-locked Ti:sapphire laser*. *Opt Lett*, 1991. **16**(1): p. 42-4.
- 10 Herek, J.L., et al., *Femtosecond real-time probing of reactions. IX. Hydrogen-atom transfer*. *The Journal of Chemical Physics*, 1992. **97**(12): p. 9046-9061.
- 11 Chudoba, C., et al., *Femtosecond studies of vibrationally hot molecules produced by intramolecular proton transfer in the excited state*. *Chemical Physics Letters*, 1995. **240**(1-3): p. 35-41.
- 12 Frey, W., F. Laermer, and T. Elsaesser, *Femtosecond studies of excited-state proton and deuterium transfer in benzothiazole compounds*. *The Journal of Physical Chemistry*, 2002. **95**(25): p. 10391-10395.
- 13 Barbara, P.F., L.E. Brus, and P.M. Rentzepis, *Intramolecular proton transfer and excited-state relaxation in 2-(2-hydroxyphenyl)benzothiazole*. *Journal of the American Chemical Society*, 2002. **102**(17): p. 5631-5635.
- 14 Lochbrunner, S., A.J. Wurzer, and E. Riedle, *Microscopic Mechanism of Ultrafast Excited-State Intramolecular Proton Transfer: A 30-fs Study of 2-(2'-Hydroxyphenyl)benzothiazole*. *The Journal of Physical Chemistry A*, 2003. **107**(49): p. 10580-10590.
- 15 Strandjord, A.J.G. and P.F. Barbara, *The proton-transfer kinetics of 3-hydroxyflavone: solvent effects*. *The Journal of Physical Chemistry*, 2002. **89**(11): p. 2355-2361.
- 16 Joshi, H.C. and L. Antonov, *Excited-State Intramolecular Proton Transfer: A Short Introductory Review*. *Molecules*, 2021. **26**(5).
- 17 Fang, C., et al., *Mapping GFP structure evolution during proton transfer with femtosecond Raman spectroscopy*. *Nature*, 2009. **462**(7270): p. 200-4.
- 18 Strandjord, A.J.G. and P.F. Barbara, *The proton-transfer kinetics of 3-hydroxyflavone: solvent effects*. *The Journal of Physical Chemistry*, 1985. **89**(11): p. 2355-2361.
- 19 Naka, K., H. Sato, and M. Higashi, *Theoretical study of the mechanism of the solvent dependency of ES IPT in HBT*. *Phys Chem Chem Phys*, 2021. **23**(36): p. 20080-20085.
- 20 Zhang, N., et al., *Solvent effect on excited-state intramolecular proton transfer process based on 'naked' diazaborepins*. *Computational and Theoretical Chemistry*, 2020. **1185**: p. 112898.
- 21 Park, S.Y., et al., *Triple proton transfer of excited 7-hydroxyquinoline along a hydrogen-bonded water chain in ethers: secondary solvent effect on the reaction rate*. *Photochem Photobiol Sci*, 2009. **8**(11): p. 1611-7.

- 22 Yordanov, D., et al., *Indirect solvent assisted tautomerism in 4-substituted phthalimide 2-hydroxy-Schiff bases*. Spectrochim Acta A Mol Biomol Spectrosc, 2020. **237**: p. 118416.
- 23 Joshi, N.K., et al., *Slow excited state phototautomerization in 3-hydroxyisoquinoline*. Photochem Photobiol Sci, 2014. **13**(6): p. 929-38.
- 24 Xian, R., et al., *Coherent ultrafast lattice-directed reaction dynamics of triiodide anion photodissociation*. Nat Chem, 2017. **9**(6): p. 516-522.
- 25 Li, J., et al., *Tuning the organic microcrystal laser wavelength of ESIPT-active compounds via controlling the excited enol* and keto* emissions*. Journal of Materials Chemistry C, 2017. **5**(46): p. 12235-12240.
- 26 Dommett, M., et al., *Molecular and crystalline requirements for solid state fluorescence exploiting excited state intramolecular proton transfer*. Journal of Materials Chemistry C, 2020. **8**(7): p. 2558-2568.
- 27 Mutlu Balcı, C., S.O. Tümay, and S. Bešli, *ESIPT on/off switching and crystallization-enhanced emission properties of new design phenol-pyrazole modified cyclotriphosphazenes*. New Journal of Chemistry, 2021. **45**(19): p. 8492-8505.
- 28 Stefanou, M., et al., *Comparison of ultrafast electron and X-ray diffraction – A computational study*. Chemical Physics Letters, 2017. **683**: p. 300-305.
- 29 Sciaini, G. and R.J.D. Miller, *Femtosecond electron diffraction: heralding the era of atomically resolved dynamics*. Reports on Progress in Physics, 2011. **74**(9): p. 096101.
- 30 Manz, S., et al., *Mapping atomic motions with ultrabright electrons: towards fundamental limits in space-time resolution*. Faraday Discuss, 2015. **177**: p. 467-91.
- 31 Ischenko, A.A., P.M. Weber, and R.J.D. Miller, *Capturing Chemistry in Action with Electrons: Realization of Atomically Resolved Reaction Dynamics*. Chemical Reviews, 2017. **117**(16): p. 11066-11124.
- 32 David Brandon, W.D.K., *Transmission Electron Microscopy*, in *Microstructural Characterization of Materials*. 2008.
- 33 Corazza, M., et al., *Comparison of ultramicrotomy and focused-ion-beam for the preparation of TEM and STEM cross section of organic solar cells*. Applied Surface Science, 2016. **389**: p. 462-468.
- 34 Kuech, T., *Handbook of Crystal Growth: Thin Films and Epitaxy*. 2nd ed. 2014.
- 35 Fox, A.M. and D.P.A.M. Fox, *Optical Properties of Solids*. 2001: Oxford University Press.
- 36 Frenkel, J., *On the Transformation of light into Heat in Solids. I*. Physical Review, 1931. **37**(1): p. 17-44.
- 37 Weller, A., *ber die Fluoreszenz der Salizylsure und verwandter Verbindungen*. Die Naturwissenschaften, 1955. **42**(7): p. 175-176.
- 38 Weller, A. *Inermolekularer Protonenübergang im angeregten Zustand*. 1956.
- 39 May, V., et al., *Charge and Energy Transfer Dynamics in Molecular Systems*. 2004: Wiley-VCH.
- 40 Laermer, F., T. Elsaesser, and W. Kaiser, *Femtosecond spectroscopy of excited-state proton transfer in 2-(2'-hydroxyphenyl)benzothiazole*. Chemical Physics Letters, 1988. **148**(2-3): p. 119-124.
- 41 Itoh, M., et al., *Time-resolved and steady-state fluorescence studies of the excited-state proton transfer in 3-hydroxyflavone and 3-hydroxychromone*. Journal of the American Chemical Society, 1982. **104**(15): p. 4146-4150.
- 42 Alarcos, N., et al., *An abnormally slow proton transfer reaction in a simple HBO derivative due to ultrafast intramolecular-charge transfer events*. Physical Chemistry Chemical Physics, 2015. **17**(25): p. 16257-16269.
- 43 Kramers, H.A., *Brownian motion in a field of force and the diffusion model of chemical reactions*. Physica, 1940. **7**(4): p. 284-304.
- 44 Smith, K.K. and K.J. Kaufmann, *Solvent dependence of the nonradiative decay rate of methyl salicylate*. The Journal of Physical Chemistry, 1981. **85**(20): p. 2895-2897.

- 45 McMorrow, D. and M. Kasha, *Intramolecular excited-state proton transfer in 3-hydroxyflavone. Hydrogen-bonding solvent perturbations*. The Journal of Physical Chemistry, 1984. **88**(11): p. 2235-2243.
- 46 Strandjord, A.J.G., et al., *Excited-state dynamics of 3-hydroxyflavone*. The Journal of Physical Chemistry, 1983. **87**(7): p. 1125-1133.
- 47 Schmidt, G.M.J. and D. Ginsburg, *Solid State Photochemistry: A Coll. of Papers Describing a Symbiot. Relationship Between X-ray Crystallography and Synthet. Organ. Photochemistry*. 1976: John Wiley & Sons, Incorporated.
- 48 Khatib, S., M. Botoshansky, and Y. Eichen, *Effects of Crystal Packing on Photoinduced Proton-Transfer Processes of 2,4-Dinitrobenzylpyridine Derivatives*. Acta Crystallographica Section B: Structural Science, 1997. **53**(2): p. 306-316.
- 49 Qian, Y., et al., *Aggregation-Induced Emission Enhancement of 2-(2'-Hydroxyphenyl)benzothiazole-Based Excited-State Intramolecular Proton-Transfer Compounds*. The Journal of Physical Chemistry B, 2007. **111**(21): p. 5861-5868.
- 50 Cheng, X., et al., *Organic Crystals with Near-Infrared Amplified Spontaneous Emissions Based on 2'-Hydroxychalcone Derivatives: Subtle Structure Modification but Great Property Change*. Angew Chem Int Ed Engl, 2015. **54**(29): p. 8369-73.
- 51 Dommett, M., M. Rivera, and R. Crespo-Otero, *How Inter- and Intramolecular Processes Dictate Aggregation-Induced Emission in Crystals Undergoing Excited-State Proton Transfer*. The Journal of Physical Chemistry Letters, 2017. **8**(24): p. 6148-6153.
- 52 Khan, A.U. and M. Kasha, *Mechanism of four-level laser action in solution excimer and excited-state proton-transfer cases*. Proc Natl Acad Sci U S A, 1983. **80**(6): p. 1767-70.
- 53 Padalkar, V.S. and S. Seki, *Excited-state intramolecular proton-transfer (ESIPT)-inspired solid state emitters*. Chemical Society Reviews, 2016. **45**(1): p. 169-202.
- 54 Wang, W., et al., *Intramolecular electron-induced proton transfer and its correlation with excited-state intramolecular proton transfer*. Nature Communications, 2019. **10**(1): p. 1170.
- 55 Wu, J.-J., et al., *Near-Infrared Organic Single-Crystal Nanolaser Arrays Activated by Excited-State Intramolecular Proton Transfer*. Matter, 2020. **2**(5): p. 1233-1243.
- 56 Towrie, M., et al., *A time-resolved infrared vibrational spectroscopic study of the photo-dynamics of crystalline materials*. Applied Spectroscopy, 2009. **63**(1): p. 57-65.
- 57 Srinivasan, R., et al., *Direct determination of hydrogen-bonded structures in resonant and tautomeric reactions using ultrafast electron diffraction*. J Am Chem Soc, 2004. **126**(8): p. 2266-7.
- 58 Van Benthem, M.H. and G.D. Gillispie, *Intramolecular hydrogen bonding. 4. Dual fluorescence and excited-state proton transfer in 1,5-dihydroxyanthraquinone*. The Journal of Physical Chemistry, 1984. **88**(14): p. 2954-2960.
- 59 Wei, G.-Q., et al., *Organic single-crystalline whispering-gallery mode microlasers with efficient optical gain activated via excited state intramolecular proton transfer luminogens*. Journal of Materials Chemistry C, 2020. **8**(34): p. 11916-11921.
- 60 Smulevich, G. and M.P. Marzocchi, *Raman excitation profiles of 1,8-dihydroxyanthraquinone at 8 K*. Chemical Physics, 1986. **105**(1-2): p. 159-171.
- 61 Smulevich, G., *Resonance Raman and fluorescence spectra of 1,8 dihydroxyanthraquinone inn-alkanes at low temperature. Evidence for excited state proton transfer*. The Journal of Chemical Physics, 1985. **82**(1): p. 14-21.
- 62 Smulevich, G., et al., *Fluorescence excitation and emission spectra of 1,8-dihydroxyanthraquinone-d0 and -d2 in n-octane at 10 K*. The Journal of Chemical Physics, 1987. **87**(10): p. 5664-5669.
- 63 Carter, T.P., G.D. Gillispie, and M.A. Connoll, *Intramolecular hydrogen bonding in substituted anthraquinones by laser-induced fluorescence. 1. 1,4-Dihydroxyanthraquinone (quinizarin)*. The Journal of Physical Chemistry, 1982. **86**(2): p. 192-196.
- 64 Zheng, D., M. Zhang, and G. Zhao, *Combined TDDFT and AIM Insights into Photoinduced Excited State Intramolecular Proton Transfer (ESIPT) Mechanism in Hydroxyl- and Amino-Anthraquinone Solution*. Sci Rep, 2017. **7**(1): p. 13766.

- 65 Arzhantsev, S.Y., S. Takeuchi, and T. Tahara, *Ultrafast excited-state proton transfer dynamics of 1,8-dihydroxyanthraquinone (chrysin) studied by femtosecond time-resolved fluorescence spectroscopy*. Chemical Physics Letters, 2000. **330**(1-2): p. 83-90.
- 66 Jethwa, J., et al., *Ultrafast Proton-Transfer and Coherent Wavepacket Motion of Electronically Excited 1,8-Dihydroxyanthraquinone in Liquid Benzyl Alcohol Solution*. Zeitschrift für Physikalische Chemie, 2000. **214**(10): p. 1367-1381.
- 67 Mohammed, O.F., et al., *Excited-state intramolecular hydrogen transfer (ESIHT) of 1,8-dihydroxy-9,10-anthraquinone (DHAQ) characterized by ultrafast electronic and vibrational spectroscopy and computational modeling*. Journal of Physical Chemistry A, 2014. **118**(17): p. 3090-9.
- 68 Mullin, J.W., *Crystallization*. 2001: Elsevier Science.
- 69 DeHoff, R., *Thermodynamics in Materials Science*. 2006: CRC Press.
- 70 Tran, R., et al., *Surface energies of elemental crystals*. Scientific Data, 2016. **3**(1): p. 160080.
- 71 Zhou, S., et al., *Space-confined vapor deposition synthesis of two dimensional materials*. Nano Research, 2018. **11**(6): p. 2909-2931.
- 72 Chen, Z., et al., *Thin single crystal perovskite solar cells to harvest below-bandgap light absorption*. Nature communications, 2017. **8**(1): p. 1890.
- 73 Gu, Z., et al., *A general printing approach for scalable growth of perovskite single-crystal films*. Science Advances, 2018. **4**(6): p. eaat2390.
- 74 Shi, Y., et al., *Bottom-up growth of n-type monolayer molecular crystals on polymeric substrate for optoelectronic device applications*. Nature communications, 2018. **9**(1): p. 2933.
- 75 Namsrai, N., et al., *Polarization Dependence of Absorption and Luminescence Spectra of a 1,5-Dihydroxyanthraquinone Single Crystal*. Journal of the Physical Society of Japan, 2006. **75**(4): p. 044703.
- 76 David R. Collins, C.R.A.C., *Computer simulation of structures and cohesive properties of micas*. American Mineralogist, 1992. **77**(11-12): p. 1172-1181.
- 77 Li, J. and M.F. Doherty, *Steady State Morphologies of Paracetamol Crystal from Different Solvents*. Crystal Growth & Design, 2017. **17**(2): p. 659-670.
- 78 Han, H., et al., *The XBI BioLab for life science experiments at the European XFEL*. J Appl Crystallogr, 2021. **54**(Pt 1): p. 7-21.
- 79 Kirchner, F.O., et al., *All-reflective UV-VIS-NIR transmission and fluorescence spectrometer for μm-sized samples*. AIP Advances, 2014. **4**(7): p. 077134.
- 80 Tauc, J., *Optical properties and electronic structure of amorphous Ge and Si*. Materials Research Bulletin, 1968. **3**(1): p. 37-46.
- 81 M. J. Frisch, G.W.T., H. B. Schlegel, G. E. Scuseria, , et al., *Gaussian 09, Revision D.01*. 2013, Gaussian, Inc.: Wallingford CT.
- 82 *Avogadro: an open-source molecular builder and visualization tool. Version 1.2.0.* <http://avogadro.cc/>.
- 83 Hanwell, M.D., et al., *Avogadro: an advanced semantic chemical editor, visualization, and analysis platform*. Journal of Cheminformatics, 2012. **4**(1): p. 17.
- 84 Marasinghe, P.A.B. and G.D. Gillispie, *Structure of 1,5-dihydroxyanthraquinone: a redetermination*. Acta Crystallographica Section C Crystal Structure Communications, 1993. **49**(1): p. 113-114.
- 85 Rohl, A.L., et al., *Hirshfeld Surfaces Identify Inadequacies in Computations of Intermolecular Interactions in Crystals: Pentamorphic 1,8-Dihydroxyanthraquinone*. Crystal Growth & Design, 2008. **8**(12): p. 4517-4525.
- 86 Cheuk, D., et al., *Investigation into solid and solution properties of quinizarin*. CrystEngComm, 2015. **17**(21): p. 3985-3997.
- 87 Bittmann, S.; Available from: <https://github.com/simonbittmann/>.
- 88 Eugene Hecht, A.Z., *The Propagation of Light*, in *Optics*. March 18, 2003, Addison Wesley Longman. p. 128.
- 89 Atkins, P. and J. De Paula, *Molecular Spectroscopy I: Rotational and Vibrational spectra*, in *Atkins' Physical Chemistry*. 2006, Macmillan Higher Education. p. 432.

- 90 Berli, C.L.A. and M.G. Bellino, *Extending Lifetime of Water Droplets Using Mirror-Nanoporous Surfaces*. *Advanced Materials Interfaces*, 2020. **8**(5): p. 2002098.
- 91 Chen, C.-C., et al., *Growth of Large-Area Graphene Single Crystals in Confined Reaction Space with Diffusion-Driven Chemical Vapor Deposition*. *Chemistry of Materials*, 2015. **27**(18): p. 6249-6258.
- 92 Bhaviripudi, S., et al., *Role of kinetic factors in chemical vapor deposition synthesis of uniform large area graphene using copper catalyst*. *Nano Lett*, 2010. **10**(10): p. 4128-33.
- 93 Marzocchi, M.P., et al., *Intramolecular hydrogen bonding and excited state proton transfer in hydroxyanthraquinones as studied by electronic spectra, resonance Raman scattering, and transform analysis*. *The Journal of Chemical Physics*, 1998. **108**(2): p. 534-549.
- 94 Dutta, P.K. and B.S. Lee, *Optical spectroscopic studies of the polymorphic forms of 1, 4-dihydroxyanthraquinone*. *Journal of Raman Spectroscopy*, 1988. **19**(3): p. 175-178.
- 95 Atkins, P. and J. De Paula, *Optical Properties*, in *Atkins' Physical Chemistry*. 2006, Macmillan Higher Education. p. 729.
- 96 Palit, D.K., et al., *Photodynamics of the S1 state of some hydroxy- and amino-substituted naphthoquinones and anthraquinones*. *Journal of the Chemical Society, Faraday Transactions*, 1990. **86**(23): p. 3861.
- 97 Lee, S., J. Lee, and Y. Pang, *Excited state intramolecular proton transfer of 1,2-dihydroxyanthraquinone by femtosecond transient absorption spectroscopy*. *Current Applied Physics*, 2015. **15**(11): p. 1492-1499.
- 98 Cho, D.-W., et al., *Excited-state Intramolecular Proton Transfer of 1,5- and 1,8-Dihydroxyanthraquinones Chemically Adsorbed onto SiO₂, SiO₂-Al₂O₃, and Al₂O₃ Matrices*. *Bulletin of the Korean Chemical Society*, 2007. **28**(4): p. 647-651.
- 99 Kandoth, N., et al., *Host-guest interaction of 1,4-dihydroxy-9,10-anthraquinone (quinizarin) with cyclodextrins*. *Photochemical & Photobiological Sciences*, 2009. **8**(1): p. 82-90.
- 100 Allen, N.S. and J.F. McKellar, *Fluorescence, phosphorescence and light fastness of hydroxyanthraquinones*. *Journal of Photochemistry*, 1976. **5**(4): p. 317-320.
- 101 Socrates, G., *Infrared and Raman Characteristic Group Frequencies: Tables and Charts*. 3rd ed. 2004: Wiley.
- 102 Ishikawa, T., et al., *Direct observation of collective modes coupled to molecular orbital-driven charge transfer*. *Science*, 2015. **350**(6267): p. 1501-5.

Appendix A

Table A 1. Coordinates of 1,5-DHAQ crystal in input file for electronic excitation calculation.

	X	Y	Z
O	2.866014	4.284133	1.812999
O	2.134240	1.023267	13.908460
O	2.638713	1.630433	6.047731
O	2.361542	3.676967	9.673728
O	1.885403	1.879350	0.304053
O	3.114851	3.428050	15.417405
O	3.619324	4.533050	7.556676
O	1.380931	0.774350	8.164782
C	3.866127	5.174715	1.894436
C	1.134127	0.132685	13.827023
C	1.638600	2.521015	5.966294
C	3.361655	2.786385	9.755165
C	3.832780	0.774350	2.947773
C	1.167474	4.533051	12.773685
C	1.671947	3.428050	4.912956
C	3.328308	1.879350	10.808503
C	4.815314	1.712167	3.097127
C	0.184940	3.595233	12.624331
C	0.689413	4.365867	4.763602
C	4.310842	0.941533	10.957856
C	-0.138340	1.792840	2.183711
C	5.138594	3.514560	13.537748
C	5.643067	4.446540	5.677019
C	-0.642812	0.860860	10.044440
C	5.916524	0.907035	1.135089
C	-0.916269	4.400366	14.586369
C	-0.411797	3.560735	6.725640
C	5.412051	1.746665	8.995819
C	4.923783	5.231504	0.966870
C	0.076471	0.075896	14.754589

C	0.580944	2.577804	6.893860
C	4.419310	2.729596	8.827599
C	1.030704	1.009468	0.157215
C	3.969551	4.297933	15.564244
C	4.474023	3.663168	7.703515
C	0.526231	1.644233	8.017944
H	3.095066	0.705884	3.553050
H	1.905189	4.601516	12.168409
H	2.409661	3.359584	4.307680
H	2.590593	1.947816	11.413779
H	0.505723	2.425482	2.232447
H	4.494531	2.881918	13.489011
H	4.999004	5.079182	5.628282
H	0.001251	0.228218	10.093176
H	4.811590	2.292797	3.773150
H	0.188664	3.014603	11.948309
H	0.693137	4.946497	4.087579
H	4.307118	0.360903	11.633879
H	3.008102	3.736410	1.069059
H	1.992153	1.570990	14.652399
H	2.496625	1.082710	6.791670
H	2.503629	4.224691	8.929788
C	3.832780	6.081750	2.947773
C	1.167474	-0.774350	12.773685
C	3.866127	-0.132685	1.894436
C	1.134127	5.440085	13.827023
C	5.870860	1.792840	2.183711
C	-0.870606	3.514560	13.537748
C	-0.366133	4.446540	5.677019
C	5.366388	0.860860	10.044440
C	-0.092676	0.907035	1.135089
C	-1.193886	1.712167	3.097127
C	6.194140	3.595233	12.624331
C	5.092931	4.400366	14.586369
C	6.698613	4.365867	4.763602

C	5.597404	3.560735	6.725640
C	-0.597149	1.746665	8.995819
C	-1.698359	0.941533	10.957856
C	4.923783	-0.075896	0.966870
C	7.039904	1.009468	0.157215
C	-2.039649	4.297933	15.564244
C	0.076471	5.383296	14.754589
C	-1.535177	3.663168	7.703515
C	6.535431	1.644233	8.017944
C	4.978496	4.297933	-0.157215
C	5.916524	6.214435	1.135089
C	-0.916269	-0.907035	14.586369
C	0.021759	1.009468	15.878673
C	1.085417	0.075896	-0.966870
C	3.914838	5.231504	16.688328
H	3.095066	6.013284	3.553050
C	4.815314	7.019568	3.097127
C	0.184940	-1.712167	12.624331
H	1.905189	-0.705884	12.168409
O	2.866014	-1.023267	1.812999
O	2.134240	6.330667	13.908460
H	6.514923	2.425482	2.232447
H	-1.514669	2.881918	13.489011
H	-1.010196	5.079182	5.628282
H	6.010451	0.228218	10.093176
C	-1.085417	-0.075896	0.966870
C	-2.176420	0.774350	2.947773
H	-1.197610	2.292797	3.773150
H	6.197864	3.014603	11.948309
C	7.176674	4.533051	12.773685
C	6.085672	5.383296	14.754589
C	7.681147	3.428050	4.912956
H	6.702337	4.946497	4.087579
C	6.590144	2.577804	6.893860
C	-1.589890	2.729596	8.827599

H	-1.702082	0.360903	11.633879
C	-2.680893	1.879350	10.808503
C	4.978496	-1.009468	-0.157215
C	7.094617	0.075896	-0.966870
O	7.894604	1.879350	0.304053
O	-2.894349	3.428050	15.417405
C	-2.094362	5.231504	16.688328
C	0.021759	6.316868	15.878673
O	-2.389876	4.533050	7.556676
O	7.390131	0.774350	8.164782
O	4.123797	3.428050	-0.304053
C	6.101876	4.400366	-1.135089
C	7.039904	6.316868	0.157215
C	5.870860	7.100240	2.183711
C	-0.870606	-1.792840	13.537748
C	-2.039649	-1.009468	15.564244
C	-1.101622	0.907035	16.856548
O	0.876458	1.879350	16.025511
C	0.092676	-0.907035	-1.135089
C	2.143073	0.132685	-1.894436
C	2.857182	5.174715	17.615894
C	4.907578	6.214435	16.856548
H	4.811590	7.600197	3.773150
H	0.188664	-2.292797	11.948309
H	3.008102	-1.570990	1.069059
H	1.992153	6.878391	14.652399
C	-2.143073	-0.132685	1.894436
C	-1.030704	-1.009468	-0.157215
H	-2.914134	0.705884	3.553050
H	7.914389	4.601516	12.168409
C	7.143327	5.440085	13.827023
C	6.030959	6.316868	15.878673
H	8.418861	3.359584	4.307680
C	7.647800	2.521015	5.966294
C	-2.647546	2.786385	9.755165

H	-3.418607	1.947816	11.413779
O	4.123797	-1.879350	-0.304053
C	6.101876	-0.907035	-1.135089
C	8.152273	0.132685	-1.894436
C	-3.152018	5.174715	17.615894
C	-1.101622	6.214435	16.856548
O	0.876458	7.186751	16.025511
C	6.147540	3.514560	-2.183711
C	7.094617	5.383296	-0.966870
O	7.894604	7.186751	0.304053
H	6.514923	7.732882	2.232447
H	-1.514669	-2.425482	13.489011
O	-2.894349	-1.879350	15.417405
C	-2.094362	-0.075896	16.688328
C	-1.147285	1.792840	17.905169
C	0.138340	-1.792840	-2.183711
C	2.176420	-0.774350	-2.947773
O	3.143186	1.023267	-1.812999
O	1.857069	4.284133	17.534457
C	2.823835	6.081750	18.669232
C	4.861915	7.100240	17.905169
O	-3.143186	-1.023267	1.812999
O	-1.885403	-1.879350	-0.304053
O	8.143440	6.330667	13.908460
O	6.885658	7.186751	16.025511
O	8.647913	1.630433	6.047731
O	-3.647659	3.676967	9.673728
C	6.147540	-1.792840	-2.183711
C	8.185620	-0.774350	-2.947773
O	9.152386	1.023267	-1.812999
O	-4.152131	4.284133	17.534457
C	-3.185365	6.081750	18.669232
C	-1.147285	7.100240	17.905169
H	5.503477	2.881918	-2.232447
C	7.203086	3.595233	-3.097127

C	8.152273	5.440085	-1.894436
C	-3.152018	-0.132685	17.615894
C	-2.202831	1.712167	18.818586
H	-0.503222	2.425482	17.953906
H	-0.505723	-2.425482	-2.232447
C	1.193886	-1.712167	-3.097127
H	2.914134	-0.705884	-3.553050
H	3.001098	1.570990	-1.069059
H	1.999157	3.736410	16.790518
H	2.086121	6.013284	19.274508
C	3.806369	7.019568	18.818586
H	5.505978	7.732882	17.953906
H	-3.001098	-1.570990	1.069059
H	8.001353	6.878391	14.652399
H	8.505825	1.082710	6.791670
H	-3.505571	4.224691	8.929788
H	5.503477	-2.425482	-2.232447
C	7.203086	-1.712167	-3.097127
H	8.923334	-0.705884	-3.553050
H	9.010298	1.570990	-1.069059
H	-4.010043	3.736410	16.790518
H	-3.923080	6.013284	19.274508
C	-2.202831	7.019568	18.818586
H	-0.503222	7.732882	17.953906
H	7.206810	3.014603	-3.773150
C	8.185620	4.533051	-2.947773
O	9.152386	6.330667	-1.812999
O	-4.152131	-1.023267	17.534457
C	-3.185365	0.774350	18.669232
H	-2.206555	2.292797	19.494608
H	1.197610	-2.292797	-3.773150
H	3.802645	7.600197	19.494608
H	7.206810	-2.292797	-3.773150
H	-2.206555	7.600197	19.494608
H	8.923334	4.601516	-3.553050

H	9.010298	6.878391	-1.069059
H	-4.010043	-1.570990	16.790518
H	-3.923080	0.705884	19.274508

Table A 2. Coordinates of 1,8-DHAQ crystal in input file for electronic excitation calculation.

	X	Y	Z
C	5.07403	3.74267	8.01661
C	0.63997	1.97133	23.43912
C	1.97133	5.07403	15.72786
C	5.19974	4.71976	7.02958
C	0.51426	0.99424	22.45208
C	0.99424	5.19974	14.74083
C	5.17117	0.99995	21.55757
C	5.08546	0.01714	20.57361
H	4.36321	0.03828	19.95363
C	0.30856	4.74262	20.49033
C	4.74262	5.40544	12.77908
H	0.22285	4.0718	19.821
H	4.0718	5.49115	12.10975
C	1.37707	4.69691	21.35091
C	4.69691	4.33693	13.63966
H	2.04961	4.03294	21.2522
H	4.03294	3.66439	13.54096
C	4.26836	0.05143	6.97405
C	1.44564	5.66257	22.39655
C	5.66257	4.26836	14.6853
C	3.11984	0.22285	7.88707
C	2.59416	5.49115	23.30957
C	5.49115	3.11984	15.59832
C	2.91985	4.87404	8.96047
C	2.79415	0.83996	24.38297
C	0.83996	2.91985	16.67172
C	1.93133	4.92547	9.86115

C	0.78853	1.93133	17.5724
H	1.29251	5.63058	9.82105
H	0.08342	1.29251	17.5323
C	1.83419	3.95409	10.86053
C	1.75991	1.83419	18.57177
H	1.14851	4.0158	11.51444
H	1.6982	1.14851	19.22569
C	2.70272	2.93128	10.89137
C	2.78272	2.70272	18.60262
H	2.61244	2.26274	11.55762
H	3.45126	2.61244	19.26887
C	3.74267	2.83414	9.96602
C	2.87986	3.74267	17.67727
C	3.89695	3.85695	8.98206
C	1.81705	1.85705	24.40456
C	1.85705	3.89695	16.69331
O	0.16571	2.78272	8.11532
O	5.54829	2.93128	23.53782
O	2.30846	1.11423	7.78528
O	3.40554	4.59977	23.20778
O	4.59977	2.30846	15.49653
O	1.5085	3.76553	6.19984
O	4.2055	1.94847	21.62234
H	1.18394	3.05642	6.5083
H	4.53006	2.65758	21.93079
O	4.6112	1.80562	10.0894
O	3.90838	4.6112	17.80065
H	5.08832	1.75477	9.39847
H	3.95923	5.08832	17.10972
O	5.87971	2.78272	8.11532
O	-0.16571	2.93128	23.53782
O	2.93128	5.87971	15.82657

C	4.26836	5.76543	6.97405
C	6.25683	4.71405	6.13507
C	-0.54283	0.99995	21.55757
C	1.44564	-0.05143	22.39655
C	-0.05143	4.26836	14.6853
C	0.99995	6.25683	13.84632
C	6.22826	0.99424	22.45208
C	6.02256	-0.97138	20.49033
C	-0.62854	5.73114	20.57361
C	5.73114	6.34254	12.86237
C	5.19974	-0.99424	7.02958
C	4.33693	1.01709	5.92841
C	0.51426	6.70824	22.45208
C	6.70824	5.19974	14.74083
C	2.91985	-0.83996	8.96047
C	2.79415	6.55396	24.38297
C	6.55396	2.91985	16.67172
C	3.11984	5.93685	7.88707
C	2.59416	-0.22285	23.30957
C	3.78267	0.78853	25.28365
C	-0.22285	3.11984	15.59832
C	1.97133	2.87986	25.38852
C	-0.63997	3.74267	8.01661
C	6.35397	1.97133	23.43912
C	0.54283	4.71405	6.13507
C	4.33693	6.73109	5.92841
O	7.2225	3.76553	6.19984
C	6.34254	5.69686	5.15111
C	-0.62854	0.01714	20.57361
O	-1.5085	1.94847	21.62234
C	1.37707	-1.01709	21.35091
C	-1.01709	4.33693	13.63966

C	0.01714	6.34254	12.86237
O	1.94847	7.2225	13.91109
C	7.15964	-0.05143	22.39655
H	5.93685	-1.6422	19.821
C	7.09107	-1.01709	21.35091
H	-1.35079	5.75228	19.95363
C	-0.54283	6.71395	21.55757
H	5.75228	7.06479	12.24238
C	6.71395	6.25683	13.84632
C	5.07403	-1.97133	8.01661
C	6.25683	-0.99995	6.13507
H	3.66439	1.68106	5.82971
C	5.40544	0.97138	5.06783
C	0.63997	7.68533	23.43912
C	7.68533	5.07403	15.72786
C	1.93133	-0.78853	9.86115
C	3.89695	-1.85705	8.98206
C	1.81705	7.57105	24.40456
C	3.78267	6.50253	25.28365
C	6.50253	1.93133	17.5724
C	7.57105	3.89695	16.69331
O	2.30846	6.82823	7.78528
O	3.40554	-1.11423	23.20778
H	4.42149	0.08342	25.24355
C	3.87981	1.75991	26.28302
O	-1.11423	2.30846	15.49653
O	1.1028	3.90838	25.5119
C	3.01128	2.78272	26.31387
C	-0.51426	4.71976	7.02958
C	-1.81705	3.85695	8.98206
C	7.53105	1.85705	24.40456
C	0.62854	5.69686	5.15111

H	3.66439	7.39506	5.82971
C	5.40544	6.68538	5.06783
H	6.89794	3.05642	6.5083
H	7.06479	5.67572	4.53113
H	-1.35079	0.03828	19.95363
C	0.30856	-0.97138	20.49033
H	-1.18394	2.65758	21.93079
H	2.04961	-1.68106	21.2522
H	-1.68106	3.66439	13.54096
C	-0.97138	5.40544	12.77908
H	0.03828	7.06479	12.24238
H	2.65758	6.89794	14.21955
C	8.30816	-0.22285	23.30957
H	7.76361	-1.68106	21.2522
O	-1.5085	7.66247	21.62234
O	7.66247	7.2225	13.91109
O	5.87971	-2.93128	8.11532
O	7.2225	-1.94847	6.19984
C	6.34254	-0.01714	5.15111
H	5.49115	1.6422	4.3985
O	-0.16571	8.64528	23.53782
O	8.64528	5.87971	15.82657
H	1.29251	-0.08342	9.82105
C	1.83419	-1.75991	10.86053
C	3.74267	-2.87986	9.96602
C	1.97133	8.59386	25.38852
H	4.42149	5.79743	25.24355
C	3.87981	7.47391	26.28302
H	5.79743	1.29251	17.5323
C	7.47391	1.83419	18.57177
C	8.59386	3.74267	17.67727
H	4.56549	1.6982	26.93694

H	0.62568	3.95923	24.82097
H	3.10156	3.45126	26.98012
C	-1.44564	5.76543	6.97405
C	-1.97133	2.83414	9.96602
C	-2.79415	4.87404	8.96047
C	8.50815	0.83996	24.38297
C	7.68533	2.87986	25.38852
C	-0.30856	6.68538	5.06783
H	1.35079	5.67572	4.53113
H	5.49115	7.3562	4.3985
H	0.22285	-1.6422	19.821
H	-1.6422	5.49115	12.10975
O	9.11954	-1.11423	23.20778
H	-1.18394	8.37158	21.93079
H	8.37158	6.89794	14.21955
H	6.89794	-2.65758	6.5083
H	7.06479	-0.03828	4.53113
H	1.14851	-1.6982	11.51444
C	2.70272	-2.78272	10.89137
O	4.6112	-3.90838	10.0894
O	1.1028	9.62238	25.5119
C	3.01128	8.49672	26.31387
H	4.56549	7.4122	26.93694
H	7.4122	1.14851	19.22569
C	8.49672	2.70272	18.60262
O	9.62238	4.6112	17.80065
C	-2.59416	5.93685	7.88707
C	-1.37707	6.73109	5.92841
C	-3.01128	2.93128	10.89137
O	-1.1028	1.80562	10.0894
C	-3.78267	4.92547	9.86115
C	9.49667	0.78853	25.28365

O	6.8168	3.90838	25.5119
C	8.72528	2.78272	26.31387
H	-0.22285	7.3562	4.3985
H	2.61244	-3.45126	11.55762
H	5.08832	-3.95923	9.39847
H	0.62568	9.67323	24.82097
H	3.10156	9.16526	26.98012
H	9.16526	2.61244	19.26887
H	9.67323	5.08832	17.10972
O	-3.40554	6.82823	7.78528
H	-2.04961	7.39506	5.82971
C	-3.87981	3.95409	10.86053
H	-3.10156	2.26274	11.55762
H	-0.62568	1.75477	9.39847
H	-4.42149	5.63058	9.82105
H	10.13549	0.08342	25.24355
C	9.59381	1.75991	26.28302
H	6.33968	3.95923	24.82097
H	8.81556	3.45126	26.98012
H	-4.56549	4.0158	11.51444
H	10.27949	1.6982	26.93694
O	2.866014	4.284133	1.812999

Table A 3. Coordinates of 1,4-DHAQ crystal in input file for electronic excitation calculation.

	X	Y	Z
C	10.37678	6.42154	4.36331
C	9.50579	7.2143	3.64203
C	6.05069	3.18823	1.12362
C	9.4486	5.5728	1.89558
C	10.31042	4.76098	2.63402
C	10.77529	5.19708	3.87275
C	6.15702	4.85822	2.94479

C	5.76241	6.16559	3.46593
C	10.20686	2.99195	0.82907
C	10.71528	3.43957	2.12211
C	6.24027	6.60557	4.69672
C	5.87828	7.87043	5.16059
C	5.05126	8.67273	4.42817
C	10.56195	1.74133	0.33429
H	10.69596	6.71628	5.18581
H	9.22534	8.02995	3.99057
H	6.62421	2.64372	1.61263
H	11.35335	4.66258	4.36752
H	6.20368	8.16998	5.97817
H	4.8251	9.51426	4.75371
H	11.62693	1.32447	1.78411
H	7.1768	4.99814	5.02853
O	11.47687	2.72931	2.7866
O	6.92461	4.13572	3.58217
O	7.06489	5.87246	5.47605
O	11.39368	0.8991	0.98196
C	6.28008	-5.78771	-4.49375
C	6.99473	-5.67339	-5.66998
C	7.30684	-4.43109	-6.17645
C	6.923	-3.28389	-5.48829
C	6.22092	-3.39888	-4.2879
C	5.8986	-4.66201	-3.79659
C	7.27556	-1.96268	-6.02552
C	1.69663	-0.6389	-2.81002
C	2.40038	-0.51892	-4.04377
C	5.8365	-2.19599	-3.52807
C	1.36014	-1.89914	-2.3249
C	1.69938	-3.03196	-3.06497
C	2.36845	-2.91784	-4.24963

C	2.73783	-1.66714	-4.75277
H	6.05533	-6.63033	-4.17013
H	7.26659	-6.43914	-6.12291
H	7.77411	-4.35911	-6.9771
H	5.42697	-4.74504	-2.99952
H	1.46751	-3.8742	-2.7473
H	2.58189	-3.68555	-4.72958
H	3.57112	-0.73976	-6.11495
H	0.58067	-1.20294	-0.7505
O	5.2172	-2.31135	-2.46544
O	7.90362	-1.87562	-7.08165
O	0.6953	-2.09301	-1.16508
O	3.42031	-1.64346	-5.91649
C	12.33738	8.20301	1.69521
C	9.92882	9.0206	-1.07368
C	2.31569	4.38798	-3.59991
C	4.72424	3.57039	-0.83103
C	13.05203	8.31733	0.51897
C	9.05783	9.81336	-1.79496
C	1.60103	4.27367	-2.42368
C	5.59523	2.77764	-0.10975
C	13.36414	9.55962	0.0125
C	9.05034	6.8037	2.40867
C	1.28893	3.03137	-1.91721
C	5.60273	5.78729	-4.31337
C	12.9803	10.70683	0.70066
C	9.00065	8.17186	-3.54141
C	1.67277	1.88416	-2.60537
C	5.65242	4.41913	1.63671
C	12.27822	10.59183	1.90106
C	9.86246	7.36004	-2.80298
C	2.37484	1.99916	-3.80576

C	4.7906	5.23095	0.89827
C	11.9559	9.32871	2.39237
C	10.32733	7.79614	-1.56424
C	2.69717	3.26229	-4.29708
C	4.32574	4.79485	-0.34047
C	13.33286	12.02804	0.16344
C	8.94401	5.13372	0.58749
C	1.32021	0.56295	-2.06814
C	5.70906	7.45728	-2.4922
C	6.89914	-0.76083	-5.28364
C	9.33861	3.82634	0.06635
C	7.75393	13.35182	3.37893
C	5.31445	8.76465	-1.97106
C	6.19538	-0.8808	-4.04989
C	9.7589	5.59101	-4.60792
C	8.45768	13.4718	2.14518
C	4.89416	6.99999	2.70322
C	11.8938	11.79472	2.66088
C	10.26732	6.03863	-3.31488
C	2.75927	0.79627	-4.56559
C	4.38575	6.55236	1.41017
C	7.23562	0.49942	-5.76876
C	8.86075	3.38636	-1.16444
C	7.41744	12.09158	3.86406
C	5.79231	9.20463	-0.74027
C	6.89639	1.63224	-5.02869
C	9.22274	2.12151	-1.62831
C	7.75668	10.95875	3.12398
C	5.43032	10.46949	-0.2764
C	6.22732	1.51812	-3.84403
C	10.04976	1.3192	-0.89589
C	8.42575	11.07287	1.93932

C	4.6033	11.27179	-1.00882
C	5.85794	0.26741	-3.34089
C	10.11399	4.34039	-5.1027
C	8.79513	12.32358	1.43618
C	4.53907	8.25061	3.198
H	12.11263	7.36039	2.01883
H	10.248	9.31534	-0.25118
H	2.54044	5.2306	-3.92353
H	4.40506	3.27565	-1.65353
H	13.32388	7.55158	0.06605
H	8.77738	10.62901	-1.44642
H	1.32918	5.03941	-1.97075
H	5.87569	1.96199	-0.45829
H	13.83141	9.63161	-0.78814
H	8.47682	7.34821	1.91966
H	0.82166	2.95939	-1.11656
H	6.17625	5.24278	-3.82437
H	11.48427	9.24567	3.18943
H	10.90539	7.26164	-1.06947
H	3.1688	3.34532	-5.09414
H	3.74767	5.32935	-0.83523
H	7.12826	2.47448	-5.34636
H	8.89734	1.82195	-2.44588
H	7.52481	10.11651	3.44166
H	5.75572	10.76904	0.54118
H	6.01388	2.28583	-3.36408
H	10.27593	0.47767	-1.22143
H	8.63919	10.30516	1.45937
H	4.37714	12.11332	-0.68328
H	5.02465	-0.65996	-1.97871
H	11.17897	3.92353	-3.65288
H	9.62842	13.25096	0.074

H	3.4741	8.66746	1.74817
H	8.0151	-0.19678	-7.34316
H	7.92423	4.9938	-1.49624
H	6.63797	12.78778	5.43846
H	6.72884	7.5972	-0.40846
O	11.2745	11.67936	3.72352
O	11.02891	5.32837	-2.6504
O	3.37856	0.91163	-5.62823
O	3.62416	7.26262	0.74569
O	13.96092	12.1151	-0.8927
O	8.17641	5.85621	-0.04989
O	0.69214	0.4759	-1.01201
O	6.47665	6.73478	-1.85482
O	7.90047	0.69329	-6.92858
O	8.03614	4.11947	-1.94377
O	6.7526	11.8977	5.02388
O	6.61693	8.47152	0.03906
O	5.17546	0.24374	-2.17717
O	10.94572	3.49816	-4.45503
O	9.47761	12.34726	0.27247
O	3.70735	9.09283	2.55033
C	8.37299	18.3787	2.58904
C	7.65833	18.26438	3.76527
C	7.34623	17.02209	4.27174
C	7.73007	15.87488	3.58358
C	8.43214	15.98988	2.38319
C	8.75447	17.253	1.89188
C	7.37751	14.55367	4.12081
C	12.95644	13.22989	0.90531
C	12.25268	13.10991	2.13906
C	8.81657	14.78699	1.62336
C	13.29292	14.49013	0.42019

C	12.95369	15.62296	1.16026
C	12.28462	15.50883	2.34492
C	11.91524	14.25813	2.84806
H	8.59773	19.22132	2.26542
H	7.38648	19.03013	4.2182
H	6.87896	16.9501	5.07239
H	9.2261	17.33604	1.09481
H	13.18556	16.4652	0.84259
H	12.07118	16.27655	2.82487
H	11.08195	13.33075	4.21025
H	14.0724	13.79393	-1.15421
O	9.43586	14.90235	0.56073
O	6.74944	14.46661	5.17694
O	13.95777	14.68401	-0.73963
O	11.23276	14.23445	4.01178
C	4.27628	6.16945	-6.26802
C	5.14727	5.37669	-5.54674
C	8.60238	9.40276	-3.02832
C	5.20446	7.01819	-3.80028
C	4.34265	7.83002	-4.53872
C	3.87778	7.39391	-5.77746
C	8.49605	7.73277	-4.8495
C	8.89065	6.4254	-5.37064
C	4.4462	9.59905	-2.73378
C	3.93779	9.15142	-4.02682
C	8.4128	5.98542	-6.60143
C	8.77478	4.72057	-7.0653
C	9.6018	3.91826	-6.33288
C	4.09112	10.84967	-2.23899
H	3.95711	5.87471	-7.09051
H	5.42773	4.56105	-5.89528
H	8.02886	9.94727	-3.51733

H	3.29971	7.92841	-6.27222
H	8.44938	4.42101	-7.88287
H	9.82797	3.07673	-6.65842
H	3.02614	11.26652	-3.68882
H	7.47627	7.59286	-6.93323
O	3.1762	9.86168	-4.6913
O	7.72845	8.45527	-5.48688
O	7.58818	6.71853	-7.38076
O	3.25939	11.69189	-2.88666
C	5.07403	3.74267	8.01661

Table A 4. Coordinates of 1,5-DHAQ molecules for excitonic coupling calculations.

	X	Y	Z
Molecule A			
C	-4.17748	2.975107	13.9916
C	-3.84363	2.644034	16.43992
C	-3.64351	3.159021	12.72101
C	-3.40727	2.334795	18.84845
C	-3.31026	2.827184	15.09082
C	-2.89617	2.512986	17.58616
C	-2.52684	2.198426	19.92606
C	-2.29137	3.190095	12.52623
C	-1.92204	2.875535	14.86614
C	-1.50795	2.561336	17.36148
C	-1.41094	3.053725	13.60385
C	-1.1747	2.2295	19.73129
C	-0.97458	2.744487	16.01237
C	-0.64073	2.413414	18.4607
H	-5.74081	2.824521	15.0013
H	-4.30526	2.280212	18.93829
H	-4.26614	3.260571	12.00178
H	-2.88236	2.091428	20.73619
H	-1.93585	3.297092	11.71611
H	-0.55207	2.127949	20.45052

H	-0.51295	3.108308	13.51401
H	0.922601	2.564	17.451
O	-5.51426	2.956786	14.10418
O	-5.05363	2.58685	16.64343
O	0.235417	2.80167	15.80887
O	0.696051	2.431734	18.34812
O	2.866014	4.284133	1.812999
Molecule B			
C	1.918063	6.747625	11.74876
C	2.354424	6.438387	14.15729
C	2.688271	6.107314	16.60562
C	1.821054	6.255237	15.50639
C	2.154303	5.9234	17.8762
C	0.802164	5.892326	18.07098
C	0.43283	6.206886	15.73107
C	-0.31451	6.852921	10.86592
C	1.037629	6.883995	10.67115
C	1.406963	6.569435	13.01105
C	-0.84848	6.669007	12.13651
C	0.018739	6.521085	13.23573
C	-0.07827	6.028696	16.99336
C	-0.51463	6.337934	14.58484
H	2.816049	6.802209	11.65892
H	4.251602	6.2579	15.59591
H	2.77693	5.82185	18.59544
H	0.44664	5.785329	18.8811
H	-0.93714	6.954472	10.14669
H	1.393153	6.990992	9.861021
H	-2.41181	6.518421	13.14621
H	-0.97626	5.974112	17.0832
O	3.564418	6.495571	13.95378
O	4.025052	6.125634	16.49303
O	-2.18526	6.650687	12.24909
O	-1.72463	6.28075	14.78834

Molecule C

C	-6.09079	6.451368	11.97122
C	-5.65443	6.14213	14.37974
C	-5.32058	5.811057	16.82807
C	-6.1878	5.95898	15.72885
C	-5.85455	5.627143	18.09866
C	-7.20669	5.596069	18.29343
C	-7.57602	5.910629	15.95353
C	-8.32336	6.556664	11.08837
C	-6.97122	6.587738	10.8936
C	-6.60189	6.273178	13.2335
C	-8.85733	6.37275	12.35896
C	-7.99011	6.224828	13.45819
C	-8.08712	5.732439	17.21581
C	-8.52348	6.041677	14.80729
H	-5.1928	6.505952	11.88137
H	-3.75725	5.961643	15.81837
H	-5.23192	5.525593	18.81789
H	-7.56221	5.489072	19.10356
H	-8.94599	6.658215	10.36914
H	-6.6157	6.694735	10.08347
H	-10.4207	6.222164	13.36866
H	-8.98511	5.677855	17.30566
O	-4.44444	6.199314	14.17624
O	-3.9838	5.829377	16.71548
O	-10.1941	6.35443	12.47155
O	-9.73348	5.984493	15.01079

Molecule D

C	-9.18355	1.933243	19.95375
C	-10.5357	1.902169	20.14852
C	-10.905	2.216729	17.80861
C	-12.1863	2.67885	14.21405
C	-11.3191	2.530927	15.31327
C	-11.4161	2.038538	19.0709
C	-11.8525	2.347777	16.66238

C	-9.41979	2.757468	13.8263
C	-8.98343	2.44823	16.23483
C	-8.64958	2.117157	18.68316
C	-9.5168	2.265079	17.58393
C	-11.6524	2.862764	12.94346
C	-10.3002	2.893838	12.74869
C	-9.93089	2.579278	15.08859
H	-8.56092	1.831692	20.67298
H	-10.8912	1.795171	20.95864
H	-13.7497	2.528264	15.22375
H	-12.3141	1.983955	19.16074
H	-8.52181	2.812051	13.73646
H	-7.08625	2.267743	17.67345
H	-12.275	2.964314	12.22423
H	-9.9447	3.000835	11.93856
O	-13.5231	2.660529	14.32663
O	-13.0625	2.290593	16.86588
O	-7.77344	2.505413	16.03132
O	-7.3128	2.135477	18.57057

Table A 5. Coordinates of 1,8-DHAQ molecules for excitonic coupling calculations.

	X	Y	Z
Molecule A			
C	-4.17748	2.975107	13.9916
C	-11.5831	8.211828	-1.24876
C	-11.4079	8.614085	0.073709
C	-10.769	8.136768	-3.53226
C	-10.6337	8.536504	-2.2031
C	-8.56283	9.361763	-4.19823
C	-7.67379	9.736121	-5.12586
C	-7.83743	9.350046	-6.45851
C	-8.86094	8.555208	-6.80791
C	-9.80551	8.134224	-5.87102
C	-9.69102	8.578239	-4.51904
C	-10.3175	9.347319	0.442084

C	-9.34694	9.689793	-0.46625
C	-9.54228	9.333457	-1.83207
C	-8.47774	9.8029	-2.74224
H	-12.5218	7.001283	-2.22421
H	-12.0586	8.372988	0.725629
H	-6.92699	10.2712	-4.87512
H	-7.21938	9.646325	-7.11562
H	-8.94844	8.276975	-7.71009
H	-11.2471	7.053362	-5.64394
H	-10.2249	9.625639	1.347244
H	-8.568	10.15778	-0.18851
O	-11.7272	7.422891	-3.92279
O	-12.6931	7.507642	-1.57802
O	-10.8392	7.378231	-6.30399
O	-7.52485	10.45475	-2.38117
Molecule B			
C	-3.31536	12.92491	5.531859
C	-2.62509	13.48426	4.485407
C	-3.16815	13.36128	3.17371
C	-2.38992	14.05182	2.125105
C	-4.77987	12.40412	1.652595
C	-4.30511	12.57225	2.953019
C	-2.84904	13.86859	0.683791
C	-2.24305	14.45731	-0.3541
C	-2.74628	14.30137	-1.64801
C	-3.81209	13.51505	-1.8652
C	-4.46839	12.87527	-0.81299
C	-4.00844	13.08151	0.522678
C	-4.96313	12.02368	4.041001
C	-4.45171	12.19806	5.32532
H	-2.99166	13.04543	6.418458
H	-1.80851	13.94611	4.636367
H	-1.46574	14.98771	-0.20797
H	-2.32884	14.74819	-2.37442
H	-4.13001	13.39443	-2.75028

H	-5.78023	11.67943	-0.42961
H	-6.10543	10.94449	3.130759
H	-4.90289	11.80423	6.065461
O	-1.3867	14.69102	2.344794
O	-5.5667	12.14111	-1.09959
O	-5.79498	11.70882	1.39477
O	-6.10857	11.31722	3.882008
Molecule C			
C	-10.1873	13.7626	3.143183
C	-9.19634	14.1852	2.29239
C	-9.31522	13.87322	0.907065
C	-8.23661	14.42703	0.063288
C	-11.3223	12.63522	1.356907
C	-11.2239	12.99377	2.699733
C	-10.4081	12.68693	-0.88905
C	-10.3496	13.04083	0.458579
C	-8.23747	14.03907	-1.41023
C	-7.32862	14.49041	-2.28277
C	-7.41585	14.14895	-3.63465
C	-8.38353	13.32103	-4.05841
C	-9.34591	12.82019	-3.18082
C	-9.31139	13.21642	-1.80972
H	-10.1473	14.00972	4.061166
H	-8.45374	14.67815	2.621694
H	-12.1582	11.42059	0.296717
H	-11.8895	12.69732	3.312587
H	-6.62021	15.04986	-1.9794
H	-6.78526	14.49914	-4.25212
H	-8.41852	13.07413	-4.97318
H	-10.7416	11.66482	-3.05826
O	-7.33296	15.10845	0.490309
O	-11.3128	11.94449	-1.34799
O	-12.3815	11.89294	0.952687
O	-10.322	12.0338	-3.68705

Table A 6. Coordinates of 1,4-DHAQ molecules for excitonic coupling calculations.

	X	Y	Z
Molecule A			
C	-4.36022	8.652773	1.324677
C	-2.98042	8.683029	1.375397
C	-3.0508	8.221097	3.726897
C	-4.4454	8.213219	3.680919
C	-5.09593	8.427772	2.467853
C	-4.53526	7.791381	6.173308
C	-5.23301	7.999718	4.908171
C	-5.25837	7.60512	7.346927
C	-2.32284	8.456774	2.564353
C	-2.34249	7.998804	4.994727
C	-3.11062	7.783852	6.21959
C	-2.45862	7.584946	7.432893
C	-3.21037	7.415037	8.595679
C	-4.57497	7.427773	8.553316
H	-4.7954	8.785609	0.51337
H	-2.49236	8.856778	0.602724
H	-6.02498	8.419234	2.429966
H	-6.89993	7.727181	6.510081
H	-1.3934	8.462128	2.590251
H	-2.77686	7.291198	9.408559
H	-5.05757	7.316463	9.340724
H	-0.74279	7.646797	6.643517
O	-6.46717	7.997399	4.854555
O	-6.60676	7.578004	7.387918
O	-1.1111	8.017485	5.022952
O	-1.11356	7.564139	7.556173
C	-4.17748	2.975107	13.9916
Molecule B			
C	2.309955	4.962754	4.251274
C	2.290302	4.504784	6.681648
C	1.522172	4.289832	7.906512

C	2.174176	4.090926	9.119814
C	1.422423	3.921017	10.2826
C	0.05782	3.933753	10.24024
C	0.272575	5.158753	3.011599
C	1.652371	5.189009	3.062318
C	1.581992	4.727077	5.413818
C	0.187394	4.719199	5.36784
C	-0.46314	4.933752	4.154775
C	0.097529	4.297361	7.860229
C	-0.60022	4.505698	6.595093
C	-0.62557	4.1111	9.033848
H	3.239393	4.968108	4.277172
H	1.855936	3.797178	11.09548
H	-0.42477	3.822443	11.02765
H	3.890007	4.152777	8.330439
H	-0.16261	5.291589	2.200291
H	2.140431	5.362758	2.289646
H	-1.39219	4.925214	4.116888
H	-2.26714	4.233161	8.197002
O	3.521688	4.523465	6.709874
O	3.519229	4.070119	9.243094
O	-1.83437	4.503379	6.541476
O	-1.97397	4.083984	9.074839
Molecule C			
C	4.62738	7.412766	9.570297
C	3.247583	7.38251	9.519577
C	3.317963	7.844442	7.168077
C	4.71256	7.85232	7.214055
C	5.363096	7.637767	8.427121
C	4.802426	8.274158	4.721666
C	5.500171	8.065821	5.986803
C	5.525527	8.460419	3.548047
C	2.59	7.608765	8.330621
C	2.609653	8.066735	5.900247
C	3.377783	8.281687	4.675384

C	2.725778	8.480593	3.462081
C	3.477532	8.650502	2.299295
C	4.842135	8.637766	2.341658
H	5.062562	7.27993	10.3816
H	2.759524	7.208761	10.29225
H	6.292147	7.646305	8.465008
H	7.167092	8.338358	4.384893
H	1.660562	7.603411	8.304723
H	3.044019	8.774341	1.486415
H	5.324727	8.749076	1.55425
H	1.009947	8.418742	4.251457
O	6.734328	8.06814	6.040419
O	6.873923	8.487536	3.507056
O	1.378267	8.048054	5.872022
O	1.380726	8.5014	3.338801

Molecule D

C	-2.04279	11.10279	6.6437
C	-2.02314	11.56076	4.213326
C	-1.25501	11.77571	2.988462
C	-1.90701	11.97461	1.77516
C	-1.15526	12.14452	0.612374
C	0.209343	12.13179	0.654736
C	-0.00541	10.90679	7.883375
C	-1.38521	10.87653	7.832656
C	-1.31483	11.33846	5.481156
C	0.079768	11.34634	5.527134
C	0.730304	11.13179	6.740199
C	0.169634	11.76818	3.034745
C	0.867379	11.55984	4.299881
C	0.892736	11.95444	1.861126
H	-2.97223	11.09743	6.617802
H	-1.58877	12.26836	-0.20051
H	0.691935	12.2431	-0.13267
H	-3.62285	11.91276	2.564535
H	0.42977	10.77395	8.694683

H	-1.87327	10.70278	8.605328
H	1.659355	11.14033	6.778086
H	2.5343	11.83238	2.697972
O	-3.25453	11.54207	4.1851
O	-3.25207	11.99542	1.65188
O	2.101536	11.56216	4.353498
O	2.241131	11.98156	1.820135

Appendix B

List of hazardous substances according to GHS (hazard symbols H- and P)

Substance	Pictogram	H-statement	P-statement
1,5-dihydroxyanthraquinone		H315 - H319 - H335	P261 - P264 - P271 - P280 - P302 + P352 - P305 + P351 + P338
1,8-dihydroxyanthraquinone		H315 - H319 - H335 - H351	P201 - P302 + P352 - P305 + P351 + P338 - P308 + P313
1,4-dihydroxyanthraquinone		H410	P273
Chloroform		H302 - H315 - H319 - H331 - H336 - H351 - H361d - H372 - H412	P201 - P273 - P301 + P312 + P330 - P302 + P352 - P304 + P340 + P311 - P308 + P313
Ethyl acetate		H225 - H319 - H336	P210 - P233 - P240 - P241 - P242 - P305 + P351 + P338
Butyl acetate		H226 - H336	P210
Acetone		H225 - H319 - H336	P210 - P233 - P240 - P241 - P242 - P305 + P351 + P338
Acetonitrile		H225 - H302 + H312 + H332 - H319	P210 - P280 - P301 + P312 - P303 + P361 + P353 - P304 + P340 + P312 - P305 + P351 + P338
Toluene		H225 - H304 - H315 - H336 - H361d - H373 - H412	P201 - P210 - P273 - P301 + P310 - P303 + P361 + P353 - P331
Isopropyl alcohol		H225 - H319 - H336	P210 - P233 - P240 - P241 - P242 - P305 + P351 + P338

Ethanol		H225 - H319	P210 - P233 - P240 - P241 - P242 - P305 + P351 + P338
---------	---	-------------	---

Acknowledgements

First, I would like to thank my supervisor Prof. R. J. Dwayne Miller to give me the opportunity to learn new things in the field of ultrafast science and in the international and interdisciplinary group, as a member of Atomically Resolved Dynamics group in MPSD. I have been always encouraged by Dwayne's supports with positive energy. He let people extract their own potentials. My mentor Dr. Ajay Jha is the best mentor ever. He guided me with practical advice to conduct doctoral project and taught me the knowledge for the laser lab experiments and organic chemistry. He put a lot of effort to expand my perspective as a materials scientist towards the view of chemistry. My senior students, Dr. Vandana Tiwari, Mr. Fernando Rodríguez Díaz, and Prof. Hong-Guang Duan made a perfect team with Ajay at the lab 095 and I took advantage of their efforts on building the lab. Especially, Vandana trained and helped me with crystallisation, microtomy, TA measurement, data analysis, and other miscellaneous tasks regarding the institute and the university. Hong-Guang and his wife Dr. Pan-Pan Zhang trained me with DFT calculations. I thank Dr. Simon Bittmann for sharing not only his TA setup and analysis software but also his idea in experiments and data analysis. I thank Dr. Günther Kassier for operating TEM and Dr. Maria Katsiaflaka for helping me in the chemistry labs. And I thank Dr. Friedjof Tellkamp and Mr. Hendrik Schikora from SSU for Machine Physics for training and helping me in the laser and machine labs. I thank Ms. Elena König in SSU for Ultrafast Electronics for conducting AFM measurements and Dr. Robin Schubert in European XFEL for training me to use the AFM instrument and operating TEM. I thank Ms. Isabelle Nevoigt in AK Fröba for measuring XRD and Dr. Frank Hoffmann for discussing the XRD results. Besides of my doctoral project, I thank Dr. Pedram Merabi and Dr. Chiwon Lee for giving me a lot of general knowledges in the ultrafast field and advice in life as a researcher.

I would like to thank my family foremost: Mr. Hyundeok Im my husband, Mr. Dongcheol Hwang my father, Ms. Chekyoung Kim my mother, Mr. Hakbin Im my father-in-law, Ms. Kyounghee Jeong my mother-in-law, Ms. Young-Ae Lee my grandmother and Mr. Sung-In Hwang my brother. Thanks to their supports and prayers, I could have studied abroad in the pandemic. My husband and I have already celebrated our first and second wedding anniversary while we have been separated – in Hamburg and Seoul, respectively. I appreciate his patience and wish us a wonderful life together from this year. Also, thanks to the prayers of my friends from Korean Catholic Community in Hamburg, I could have carried on being blessed.

Declaration on Oath

„I hereby declare on oath that this doctoral dissertation is written independently and solely by my own based on the original work of my PhD and has not been used other than the acknowledged resources and aids. The submitted written version corresponds to the version on the electronic storage medium. I declare that the present dissertation was prepared maintaining the Rules of Good Scientific Practice of the German Research Foundation and it has never been submitted in the present form or similar to any other University or board of examiners.“

Date 5. January 2023

Signature Hwang, Hyein

